Development of four-terminal mechanically-stacked solar cells utilising hydrogenated amorphous silicon oxide (a-SiO_x:H) and crystalline silicon cells

Aditya Chaudhary

Technische Universiteit Delft

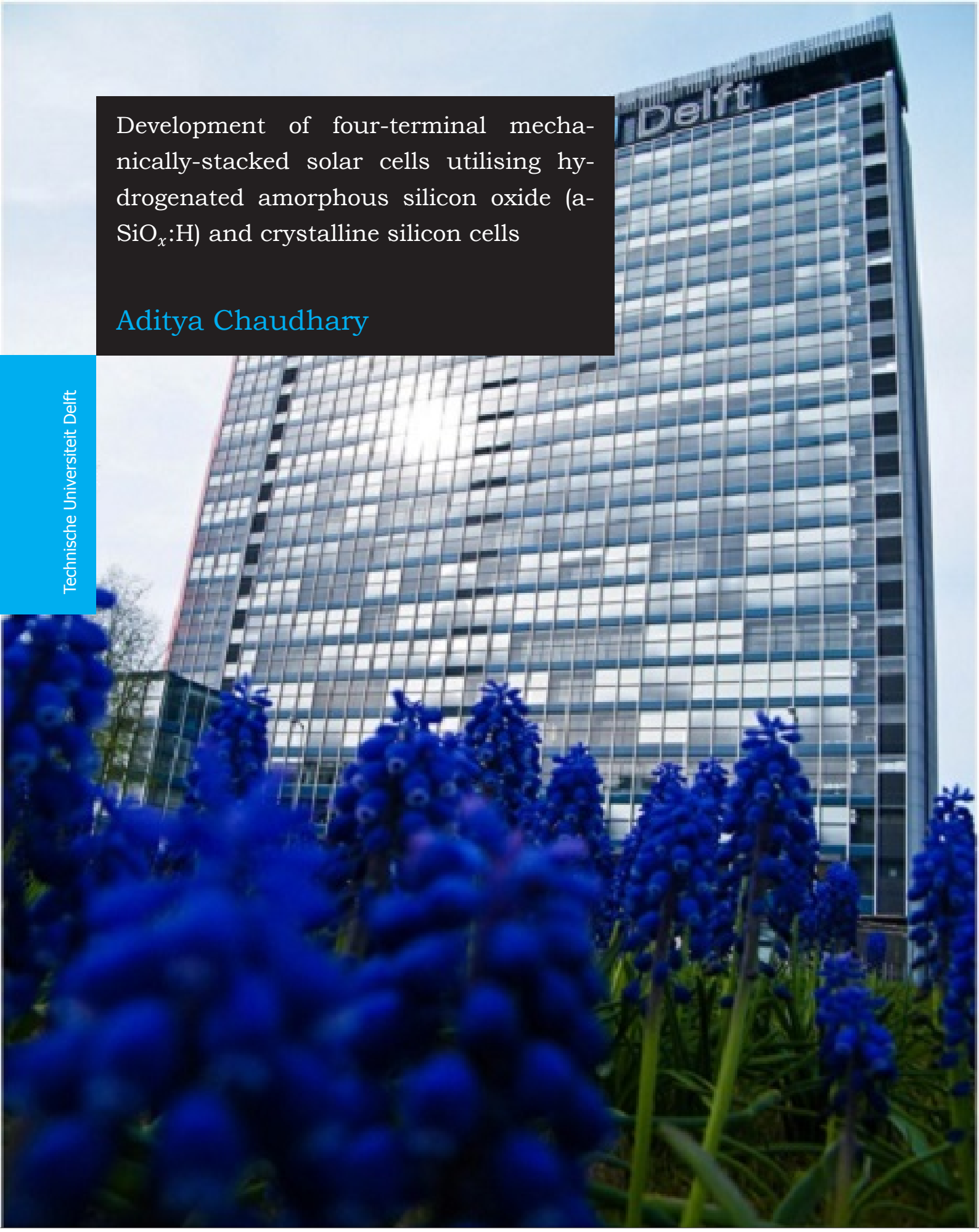

TU Delft Delft University of Technology

Challenge the future

Development of four-terminal mechanically-stacked solar cells utilising hydrogenated amorphous silicon oxide (a-SiO_x:H) and crystalline silicon cells

by

Aditya Chaudhary

in partial fulfillment of the requirements for the degree of

Master of Science
in Electrical Sustainable Energy

at the Delft University of Technology,
to be defended publicly on 15thAugust, 2017 at 14:00 PM

Supervisor:	Dr. R.A.C.M.M. van Swaaij ,	TU Delft
Thesis committee:	Prof. dr. Miro Zeman ,	TU Delft
	Dr. Erik van der Kolk ,	TU Delft
	Dr. R. Santbergen ,	TU Delft
Student Number:	4469828	

An electronic version of this thesis is available at http://repository.tudelft.nl/.

TU Delft Delft University of Technology

Preface

I still remember that fortunate day, when I walked into the office of Dr. René van Swaaij to discuss master thesis project. The discussion with Dr. René van Swaaij was so enthralling that I decided to pursue my thesis project under his guidance in PVMD group. The research was difficult and challenging, but extensive investigation and constant experimental work, made me develop the cell which is first of its kind. I would like to thank my thesis supervisor, daily supervisor and mentor Dr. René van Swaaij for his excellent guidance and support during this research. I am also very thankful to Dr. ir Rudi Santbergen for his constant support in the complex simulations and writing of the thesis.

I am also indebted to Martijn Tijssen and Stefaan Heirman for their technical help and providing me in-depth knowledge of machines and instruments. I am also grateful to Gianluca Limodio and Dr. Guangtao Yang for providing me with some of their solar cells. I would also like to thank all the members of the PVMD group for helping me in my research. I would like to thank Steve van Doorene and Nirmal Haldikar for their wonderful cooperation in relaxing me by the chilled talks during our coffee breaks, after long hours of experimental work.

I would like to thank my little sister, parents and grandparents for their constant faith in me.

Finally, I would like to thank the entire community engaged in exploration and utilisation of solar energy. I hope the great power of sun will help all of us to flourish and prosper.

Aditya Chaudhary
Delft, August 2017

Abstract

A tremendous amount of research in improving the efficiency of the single junction crystalline silicon (c-Si) based solar cells has brought its efficiency (26.6%) close to the theoretical maximum achievable conversion efficiency (29.43%) [1–3]. Thus to further improve the efficiency, new avenues of reducing losses need to be opened up. One of the major loss, spectral mismatch loss, can be reduced by utilising tandem structures. Still, there are shortcomings associated with the conventional tandem device structure.

This thesis describes how higher efficiencies can be achieved by utilising four terminal mechanically stacked structures. This structure utilises two solar cells, which are electrically isolated but optically connected. Isolating the cells electrically negates the problem of current matching which is present in conventional tandem cells. This structure also removes constraints such as lattice matching for the two cells. Hence many different types of four terminal cells can be developed.

In this work, high bandgap hydrogenated amorphous silicon oxide (a-SiO_x:H) thin film top cell was fabricated using plasma-enhanced chemical vapor deposition (PECVD). Three different types of c-Si cells namely, poly-Si, interdigitated back contact (IBC) and silicon heterojunction (SHJ (Hybrid)) were utilised as the bottom cells. This is the first instance where an a-SiO_x:H based cell has been used with c-Si cells in a four terminal application.

Before actual fabrication, theoretical calculations using two parameters called as Response 4T (R_{4T}) and Spectral Response 4T (SR_{4T}) were made to determine the optimal configuration as well as the efficiency enhancement for the four-terminal device. From this theoretical calculation, an efficiency gain of almost 4% can be obtained when an a-SiO_x:H top cell is used with a poly-Si cell in four terminal configuration. Gain between 1% and 2% can be realised by utilising four terminal topology for IBC and SHJ (Hybrid) bottom cells. These gains in efficiency are in comparison to the efficiency of the bottom cell alone.

A first of its kind- bifacial a-SiO_x:H cell with the efficiency of 6.60% (V_{oc}:0.97 V, J_{sc}:10.31 mA/cm^2 and fill factor:0.66) was developed. Using this cell as the top cell four terminal devices were fabricated. A gain in efficiency of 0.46% was obtained for the four terminal device based on the poly-Si bottom cell.

Further analysis of the four terminal devices using GenPro4 simulation tool was also performed. The analysis pointed to the reflection due to the top cell substrate glass as the limiting factor in improving the efficiency of the four terminal cell further. Parasitic absorption in the carrier selective layers of the thin film cell was another contributor to the losses. Through this work, the potential of four terminal device concept was analysed and actual development of the device was carried out. From the work done, future steps in improving the efficiency of the four terminal device were also deduced.

Present work positively brought hope for further improvement in efficiency of crystalline silicon solar cells.

List of Figures

Contents

1

Introduction

1.1. Introduction

As the world marches towards a greener future, solar energy has come to the forefront. Silicon photovoltaic (PV) have been commercialised in the last three decades to an extent that, they are the most prominent PV technology. With the total global installed PV capacity surpassing 300 GW in 2016, the price of electricity generated from PV plants has hit a record low. It is now competing with the price of electricity from coal power plants. With the point of socket parity being reached, it seems logical to improve the efficiencies of the PV panels to further reduce the cost, to enter into multi-terawatt regime as well as for penetration in the developing markets [17]. A higher efficiency of crystalline silicon cells directly translates into a smaller and thus less expensive PV system, which further lowers the cost involved. Also, a higher power generation from a small area is beneficial when looking at urban centers, where the area is often a limiting factor.

In this chapter, the state of the art geometry of PV cells (multijunction cells) is introduced. The interest in this geometry lies in the fact that the efficiencies of crystalline silicon cells have almost reached their upper limit. The record efficiency for a crystalline silicon cell was recently set at 26.6% by Kaneka corporation, which is near to the maximum achievable efficiency limit of 29.43% [1–3]. This is the reason why utilising multijunction cells is a viable option to achieve higher efficiencies. A multijunction cell is a stack of PV cells made of different bandgap materials. There are two ways in which these cells can be realised one is to utilise two output terminals for the whole stack and another is to have separate output terminals for each cell. In this work, development of a new architecture of PV cell utilising hydrogenated amorphous silicon oxide (a-SiO_x:H) cell and crystalline silicon (c-Si) cell in a four terminal configuration will be done.

1.2. Multijunction Solar Cells

Shockley-Queisser (S-Q) detailed balance model defines the limiting power conversion efficiency of a single junction solar cell at 33.1%. This is for an optimum semiconductor material with a band gap of 1.34 eV under AM 1.5 spectrum [18]. Even though this limit has been taken as the ultimate achievable efficiency in photovoltaic industry. However, the S-Q model is based on the assumption that only radiative recombination takes place, which is not a good assumption for indirect materials such as crystalline silicon. So for crystalline silicon, another limiting efficiency calculated by Richter et al. at 29.43% is used [3]. The major loss mechanism identified in both the models is the spectral mismatch. This accounts for almost 50% of the total losses. Spectral mismatch can be divided into two sub parts- Non-absorption and Thermalisation. The major losses are shown in the figure 1.1.

Non absorption losses, as shown in figure 1.2, occur because a large part of the spectrum is not absorbed by the photovoltaic cell. This is because the energy of the photons in this part is lower than the bandgap energy of the absorber material. Thermalisation losses occur due to the interaction between excited carriers which have excess energy and crystal lattice, as these carriers cool (lose energy) to the bandgap edge.

Thus to reduce spectral losses, various techniques have been developed such as utilising cells made of stacks of different bandgap absorber layers, so that most of the spectrum can be absorbed which

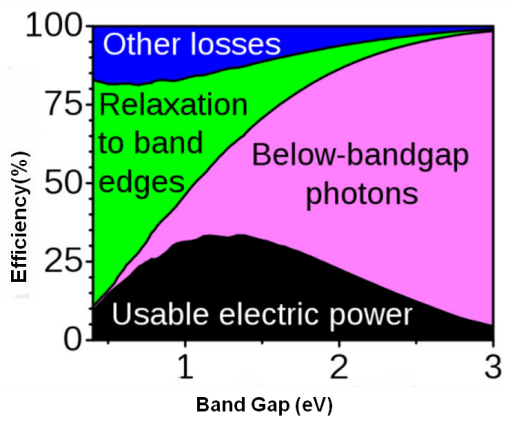

Figure 1.1: Major losses which are taken into account in Shockley-Queisser limit calculations [4].

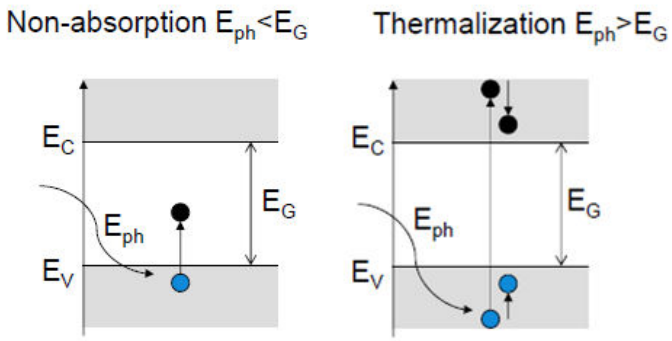

Figure 1.2: Spectral mismatch losses shown with a band diagram, the sphere shown represent the charge carriers [4].

is termed as a multijunction approach. Spectrum Splitting techniques have also been projected in reducing spectral mismatch losses [19]. Up-conversion and down-conversion are also possible solutions, but a significant research is required to successfully utilise these techniques. The most popular among these is the use of multijunction or multiband approach. By adding a cell made of high bandgap material on top of a cell with a relatively lower bandgap, spectral mismatch losses can be reduced. This is the basis of multijunction solar cells. Cells with efficiencies of 38.8% utilising five junctions have been developed [20]. The highest efficiency in case of a micromorph cell (a multijunction cell with a-Si and nanocrystalline silicon) has reached 13.6% [21]. The record cells mentioned above, utilise two output electrodes as shown in figure 1.3a.

The power generated in the component cells of a tandem structure can be utilised also in a four-terminal configuration. These type of cells are termed as mechanically stacked solar cells (MSSC) as shown in figure 1.3b. Problems such as current mismatch, which arises when different cells are connected in series (conventional multijunction cells), is not present in a four-terminal configuration. Another problem pertaining to multijunction cells is the constraint on the choice of materials that can be utilised. This is because of the limitation of lattice constants for growing subsequent layers. In a four terminal device, the two cells can be developed separately and then combined together. Thus the four terminal approach opens up a possibility to develop many new combinations of cells with different materials. One more advantage is that there is no need for developing any tunnel recombination junction (TRJ) between the two cells, which is the case when multijunction cells are developed. These type of cells are optically coupled such that lower wavelength light is absorbed in the top cell and the rest of the spectrum is absorbed in the bottom cell, hence the cells can be operated at their respective maximum power point. This reduces the spectral sensitivity and increases the time integrated energy yield as compared to two terminal single junction cells [5].

Various combinations of four terminal devices developed in the last decade, have achieved efficiencies greater than 25%. A small analysis of some of the four terminal cells are given in the below

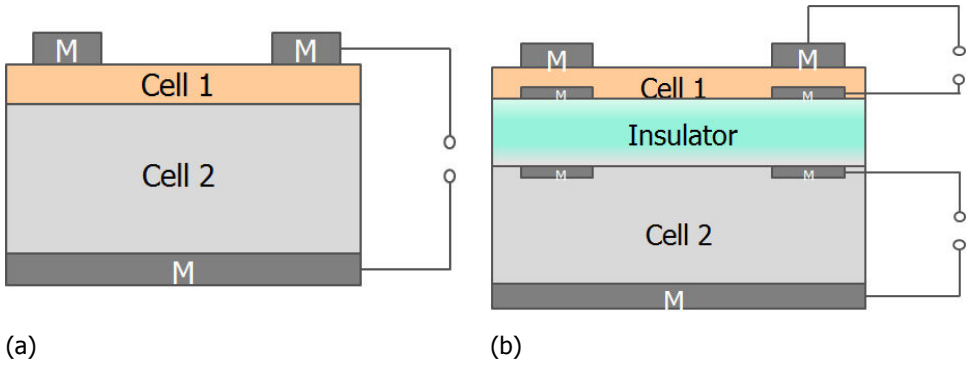

Figure 1.3: (a) A two terminal Device. (b) A four terminal device with an electrical insulator between the two cells.

section.

1.3. Four Terminal Mechanically Stacked Solar Cells

In this section some of the four terminal devices based on different materials are briefly touched upon.

1.3.1. III-V Materials and Perovskites Based Four Terminal Solar Cells

It is well known that III-V materials are suitable for application in thin film solar cells, as their band gap can be easily tuned by alloying, they have high absorption coefficients and multijunction cells with high efficiencies can be easily formed. Various four terminal solar cells have been developed utilising III-V materials based cells with CIS/CIGS (Chalcogens) and c-Si cells.

Stephanie Essig et al. provide a lot of details in fabrication and characterisation of the III-V material based four terminal solar cells [5, 22, 23]. The record cell with an efficiency of (29.8±0.6)% utilises a GaInP top cell with metal grids and antireflection coatings (ARC) on both front and back side and the bottom cell is made of a-Si:H/c-Si heterojunction (SHJ) as shown in figure 1.4 [5, 24].

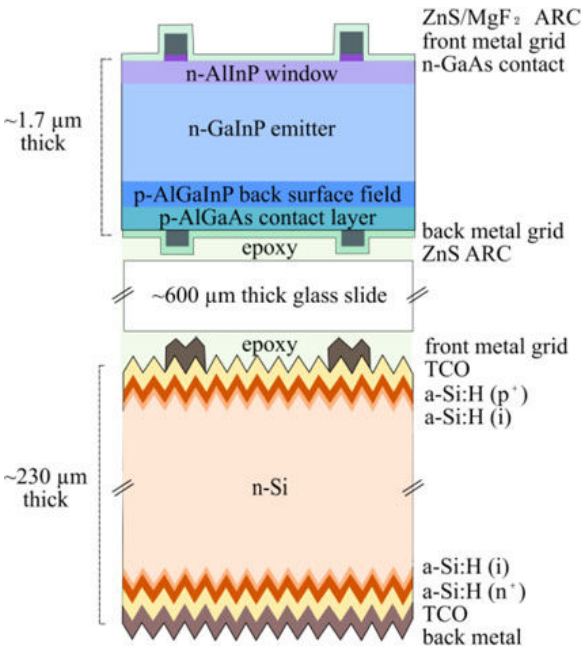

Figure 1.4: The GaInP cell with a Silicon heterojunction cell in four terminal configuration [5].

Perovskites are also interesting materials that could be utilised in a four terminal configuration. Among the available wide bandgap materials which can be used in tandem with c-Si, perovskites are promising because of their high absorption coefficients, a sharp absorption edge, a tunable bandgap

and simple preparation process.

In the paper by Zhang et al., results of optical and electrical simulations were shown for a four terminal cell with perovskite based top cell and c-Si bottom cell [25]. The total efficiency gain of 5% is observed when perovskite cell is used with the c-Si cell (efficiency of 19.5%) in four terminal configuration.

More insight into the performance of Perovskite based four terminal solar cell can be gained from the paper by Jeremie Werner et al. [26]. In his work, a heterojunction silicon bottom cell is used with perovskite based top cell. This combination gave a steady-state efficiency of 25.2%. An optical coupling liquid was used to connect the two subcells and reduce reflection losses.

Recently a new perovskite cell based on rubidium was developed, which when utilised in a four terminal topology with an IBC c-Si cell, gave an efficiency of 26.6% [27].

1.3.2. Amorphous Silicon Based Four Terminal Solar Cells

Hydrogenated amorphous silicon (a-Si:H) solar cells were invented by David.E.Carlson in the year 1974, almost twenty years after the first silicon solar cells were fabricated at Bell laboratories in the United States. Due to higher absorption coefficient of amorphous silicon as compared to crystalline silicon, non-epitaxial growth on any kind of surface, low processing temperature it becomes a good candidate for thin film cells. This opened up a large possibility of making new kinds of solar cells utilising a-Si and its alloys such as a-SiO_x:H, a-SiC etc.

Carlson et al. in the paper on a-Si:H solar cells, mentions a four terminal cell, utilising high band gap a-Si and CIS (chalcogen) cell. The paper even mentions, a company called Arco Solar which is now called Solar World that was manufacturing four terminal cells of 15.6% efficiency. This cell consisted of a top cell of a-Si:H and a bottom cell of cadmium-sulfide/copper-indium diselenide (CdS/CIS) junction [6]. The design of the cell is shown in figure 1.5. The actual analysis and fabrication procedure is not mentioned in the work of Carlson et al.

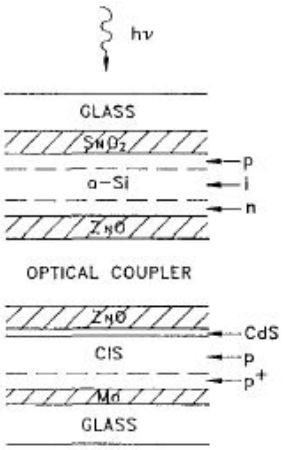

Figure 1.5: The a-Si/CIS cell in a four terminal configuration [6].

In the year 1990, new papers on four terminal solar cells were published by Y. Matsumoto et al., from Osaka University, Japan. In the papers by the group the top cell is made of conventional p-a-SiC/i-a-Si/n-μc-Si and the bottom cell is made of poly-silicon. The amorphous and microcrystalline layers were prepared by RF plasma deposition [7, 28]. The bottom poly-Si cell was made of n type poly c-Si with p type μc-SiC, as the window layer. The highest efficiency of 16.8% was obtained, at AM1 and cell areas of 0.033 cm^2 and 0.16 cm^2 for the top and bottom cells. Silicon oil with a refractive index of 1.5 was used in this cell. The configuration can be seen in figure 1.6. The defects between the heterojunction interface can be reduced by introducing an a-SiC buffer layer between μc-Si and poly silicon, also the a-SiC layer provides higher structural flexibility, thus preventing strain induced defects [8]. The efficiency was further boosted to 19.1% by utilising n type μc-Si in the bottom cell as shown in figure 1.7.

Analysing the timeline of four terminal solar cell development, it can be seen that in 1990's a lot of work was done on utilising a-Si:H thin film cells with crystalline silicon cells. In the next two decades

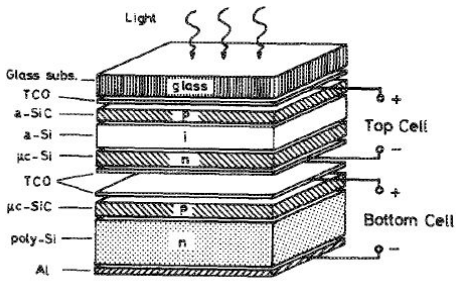

Figure 1.6: The a-Si/poly-Si cell in a four terminal configuration [7].

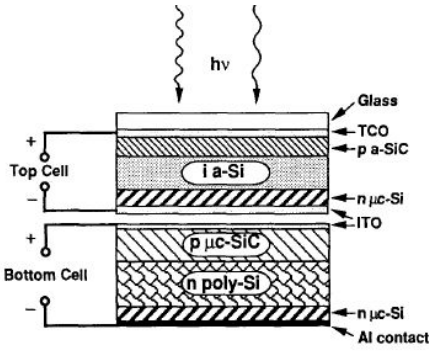

Figure 1.7: The a-Si/poly-Si cell in a four terminal configuration with buffer layers [8].

this shifted to the utilisation of III-IV materials, which has lead to the development of the highest efficiency four terminal device [5]. With the improvement in the fabrication process of perovskite cells, they have come to the forefront now.

In spite of about three decades of work on four terminal devices, no one has tried to combine hydrogenated amorphous silicon oxide cell (a-SiO_x:H) with crystalline silicon cells. This combination seems promising and interesting to develop. In recent 2 to 3 years, there has been a substantial improvement in the development of hydrogenated amorphous silicon oxide cells (a-SiO_x:H), with the efficiency reaching to 8.8% [29]. This efficiency coupled with a high open circuit voltage and fill factor becomes very promising when utilised with a c-Si cell.

In this work, hydrogenated amorphous silicon oxide cell (a-SiO_x:H), has been utilised in combination with c-Si cell.

1.4. Objective and Outline of Thesis

The aim of this thesis is to develop and assess the efficiency potential of an a-SiO_x:H based four terminal solar cell in conjugation with a c-Si cell. To accomplice this goal, following tasks are performed:

1. Determining the theoretical gain that can be achieved by using a-SiO_x:H based top cell and different c-Si bottom cell.
2. Development of a-SiO_x:H cell to achieve high open circuit voltage and fill factor.
3. Development of an optimum transparent conductive oxide layer for the back contact of the a-SiO_x:H cell.
4. Developing the suitable fabrication process for four terminal solar cell.
5. Utilising optical simulation tools to assess areas where further improvements are required to achieve higher efficiencies.

The layout of this thesis is shown in the figure 1.8.

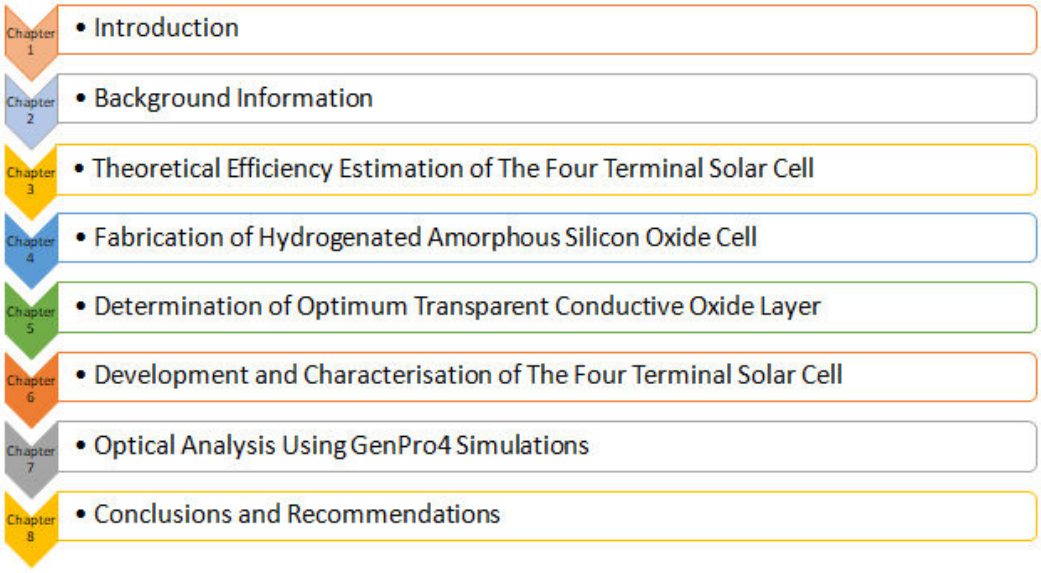

Figure 1.8: Outline of the Thesis.

The second chapter describes the important materials and the equipments used for development and characterisation of the solar cells. The third chapter contains the estimation of the four terminal device efficiency utilising theoretical parameters. The fourth chapter is about the fabrication of the a-SiO_x:H top cell. The fifth chapter deals with the determination of the optimum back transparent contact for the a-SiO_x:H top cell. The sixth chapter focuses on the final development and characterisation of the four terminal solar cell. The penultimate chapter covers optical simulations to deduce the loss mechanisms in the combination. It identifies potential target areas for further improving the efficiency of these devices. The last chapter summaries the conclusions deduced from this work. It also contains some recommendations, drawn from this work, that can be applied to achieve higher efficiency four terminal solar cells.

2

Background Information

2.1. Introduction

This chapter pertains to some background knowledge, which will be helpful in better understanding this work. Two major sections are involved in this chapter. The first section titled ”Materials” provides a brief overview of the materials used in this work. This section is divided into three major subsections namely, hydrogenated amorphous silicon (a-Si:H) which is the main material to develop a silicon oxide (a-SiO_x:H) based cell, c-Si cells and transparent conductive oxides (TCO). The second section titled ”Experimental Methodology” is dedicated to the material deposition techniques for the development of a-SiO_x top cell and all the characterization setups used in this work. The material deposition and photovoltaic cell fabrication were carried out in Else Kooi Laboratory clean room 10000-TU Delft. The required characterizations were carried out in EWI, Tu Delft.

2.2. Materials and Cell Structure

2.2.1. Hydrogenated Amorphous Silicon (a-Si:H)

Before going into details of the cells developed using a-SiO_x:H which are incorporated in Chapter 4, a brief discussion on amorphous silicon (a-Si) is done in this section so to get a slight insight into the material structure and properties. This is done because a-SiO_x:H is a derivative of a-Si:H.

In the year 1965, the first a-Si films were developed by using radio frequency glow discharge [30]. It took almost 10 years to finally have a working photovoltaic cell made of a-Si, which had an efficiency of 2.4% [31]. This delay in the development was due to the difficulty in doping the material as well as developing material with lower defect density. One way of reducing the defect density is by the incorporation of hydrogen in the material. The hydrogen atoms passivate some of the defects in the material, hence higher efficiency devices can be fabricated. This is the reason why almost all the authors refer to amorphous silicon as hydrogenated a-Si (a-Si:H).

The structure of a-Si:H is the reason why it has significantly different properties as compared to crystalline silicon. Due to small deviations in bond angles and bond lengths between the neighboring atoms, there is a complete loss of the locally ordered structure on a scale exceeding a few nanometers. This resulting atomic structure of a-Si:H is called a continuous random network. In this structure, a large number of defects (10^{15} to 10^{16} cm^{-3}) are found due to the silicon atoms which are bonded to only three neighbouring atoms even after passivation by hydrogen [32]. Due to this long range disorder, the definition of electronic band structure is modified by taking into account the band tailing. For a material with a large concentration of defects, the density of states inside the bands is reduced. Thus by the law of conservation of Eigenstates (also referred as the golden rule), energy levels extend from the band edge into the band gap. These tails are also referred to as the Lifshitz tail [33]. A diagram of density of states is shown in figure. 2.1.

Thus the bandgap, defined in case of a-Si:H, is called Tauc bandgap. Thisis calculated from the Tauc plot [34]. In our case, we will define the bandgap as optical bandgap, E_{04}, which is the photon energy in electron volt when the absorption coefficient of the material is 10^4.

The doping of a-Si:H is in itself a very important aspect. The doping efficiency is low in a-Si:H

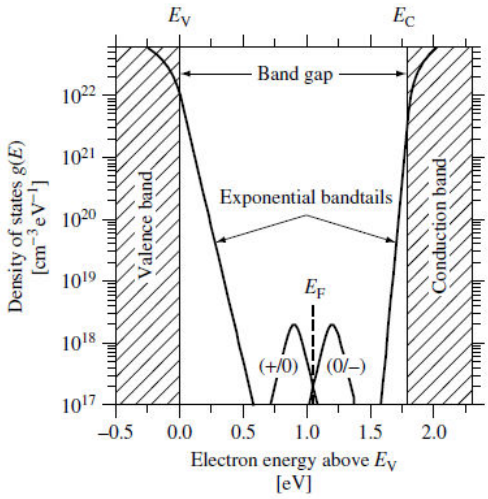

Figure 2.1: Density of states diagram with two bands in the middle represent the amphoteric dangling silicon bonds (D-Center).

in contrast to c-Si because of the structural differences. For example in phosphorus doping this phenomenon is observed. This is termed as phosphorus paradox. This is because phosphorus atoms bond to only three silicon atoms, which is in accordance with Mott rule [35]. This is chemically advantageous for phosphorus atoms as only three electrons in the P orbital are involved in bonding and the other two S orbital electrons remain tightly bound. Because of this reason we use a nanocrystalline silicon oxide n layer (fine silicon crystallites with size of the order of few nanometers bound with hydrogen in an amorphous silicon oxide matrix).

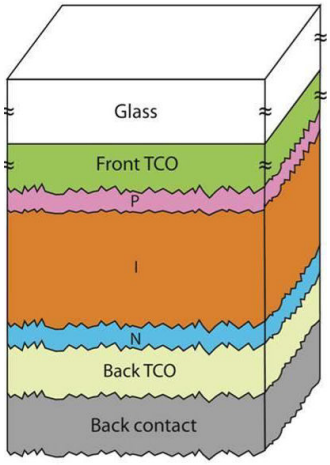

Figure 2.2: Schematic of p-i-n structure, light enters from the p side [9].

The photovoltaic cells developed with a-Si:H materials utilise either the p-i-n or the n-i-p structure. These structures are completely different from the structure utilised in conventional crystalline cells. For doped a-Si:H, the minority carrier's (holes in n-type a-Si:H and electrons in p-type a-Si:H) diffusion length is low, so a p-n structure would collect carriers from photons generated in an extremely thin layer of doped a-Si:H. This also means that diffusion alone can not lead to transport of charge carriers. Thus there is a need to utilise an intrinsic layer which acts as the absorber/active layer in between the two doped layers. Due to a built-in field in the intrinsic layer charge transport happens. Hence these kind of devices are called drift device. It is interesting to note that the photons absorbed in the doped layer do not contribute significantly to the generated current. Hence these layers are made very thin. In this work, only superstrate (p-i-n) configuration is utilised as shown in figure. 2.2. In superstrate configuration p layer is deposited first and then the other layers. Thus light passes through p layer

first. This is done because holes have lower mobility than electrons. As the cells are deposited on a glass (Asahi VU) substrate this topology is followed. The band diagram (Energy-position diagram) of a p-i-n structure is shown in figure. 2.3.

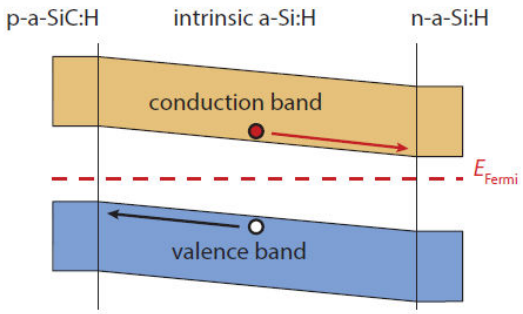

Figure 2.3: A simple schematic of p-i-n band diagram [4].

There are several advantages associated with utilising a-Si:H to develop solar cells. The material processing is relatively simple as easy process as compared to c-Si. The bandgap and optical properties of a-Si can be tuned, by adding Oxygen, Carbon (to increase the bandgap) or Germanium (to decrease the bandgap) when depositing a-Si:H layer [36–40]. The addition of Oxygen is done by adding Carbon Dioxide precursor gas in the PECVD process. For Carbon and Germanium; Methane and Germane are used respectively. This makes it easier to develop cells with different bandgap. With different bandgap of absorber layers cells dedicated for a specific part of solar spectrum can be developed. This approach was used by Yan et al., to develope 16.3% initial efficiency, triple junction cells of a-Si:H/a-SiGe:H/nc-Si:H [41]. Another advantage associated with a-Si:H material is that it can be deposited on flexible substrates, so it can be used in applications requiring low weight and flexible operations. Even though after almost four decades of research on these cells, they are still not competitive to the crystalline solar cells. So it becomes imperative that they should be utilised in an approach where the advantages associated with them can be coupled to other technologies, hence developing devices that have higher efficiencies. Even high efficiency c-Si devices, such as heterojunction with intrinsic thin layer cells, utilise a-Si:H layer to make window layers and carrier selective layers. In this work, cells made of high band gap material i.e a-SiO_x:H will be utilised. The reason for using it is explained in chapter-3. The optimised layer structure developed in the work of Guijt and Kim is utilised in this work. More details pertaining to the exact parameters of depositions can be found in their work [29, 42]. The back contact is made of silver (100 nm) / chromium (30 nm) / aluminium (500 nm) layers. The structure of the cell followed in this work is TCO substrate (Asahi VU glass) / p-nc-Si (seed) / p-a-SiO_x:H (7 nm) / a-SiO_x:H buffer / i-a-SiO_x:H (200 nm)/n-nc-Si:H (5 nm) / n-nc-SiO_x:H (100 nm) as shown in Fig. 2.4 [42].

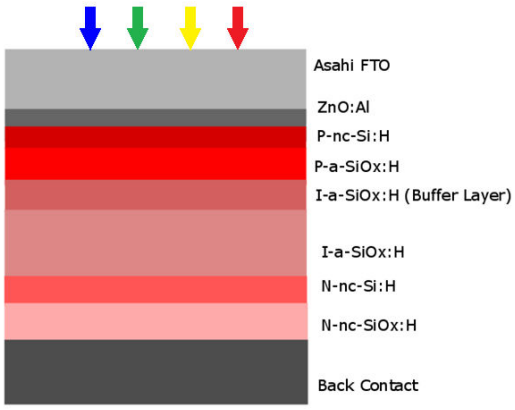

Figure 2.4: Schematic structure of the a-SiO_x:H, with all the layer used.

Throughout this work, the above mentioned structure will be used to compare the cells developed. To make more accurate comparisons the reference cell will be developed every time a parameter is changed so as to maintain consistency in the comparison. This is because of some minor fluctuations in the deposition processes. All the layers utilised are also made each time and the required activation energy, bandgap and deposition rate are also measured. Each cell is annealed at 120°C for 1.5 hours.

2.2.2. Crystalline Silicon

The structure of the three types of the c-Si cells namely- Polycrystalline-Silicon (poly-Si), Interdigitated Back Contact (IBC) and Silicon Heterojunction (SHJ (Hybrid)), used as the bottom cells in this work are shown below in figure. 2.5. There are major differences in the three types of cells mentioned above. A poly-Si cell utilises carrier selective (doped) layers of poly silicon. A major advantage of these cells is that they are easy to fabricate. Whereas due to free carrier absorption in the poly silicon layers the efficiency of these cells is not too high. The IBC cells are a high efficiency cell concept. In these cells, all the carrier selective contacts are present at the back side of the cell. Due to this, there is no front shading loss in this concept. The SHJ (Hybrid) cells use an intrinsic a-Si:H layer between the n doped layer and the n type FZ silicon wafer. The presence of this intrinsic a-Si:H layer, reduces the defect density at the a-Si:H/c-Si interface. With reduced defects (reduced recombination losses) a V_{oc} greater than 700 mV can be obtained [43]. For the p layer- poly-Si is used. Because poly-Si is used as the p layer this cell is called as a SHJ (Hybrid) cell. The metal back contact in the cells is composed of silver (200nm)/ chromium (30nm)/ aluminium (2μm) layers. A detailed analysis of each type of cell is too wide for this work. It should be mentioned that the c-Si wafer used has pyramidal texturing. All of these cells were developed in the PVMD group in TU Delft. The exact details can be found in the work of Limodio and Yang et al. [44–46].

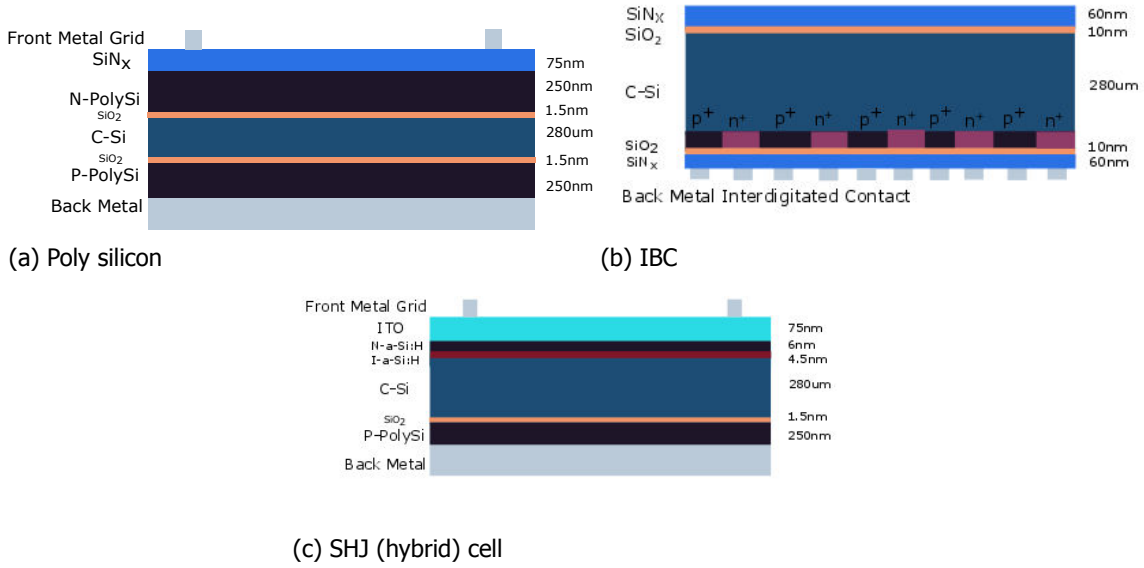

(a) Poly silicon

(b) IBC

(c) SHJ (hybrid) cell

Figure 2.5: Schematic of various c-Si cells used as bottom cell in this work. The thicknesses shown are not to scale.

2.2.3. Transparent Conductive Oxides (TCO)

A TCO usually consists of a wide bandgap degenerate semiconductor with a low resistivity and high transparency in the visible and near infrared range. Typical values for a TCO are shown in table 2.1. Though these values are a function of the thickness as well as the deposition parameters, still most of the TCO films used for solar cell applications have values between these numbers [47–50]. Even though it may look impossible to have a material which has high bandgap and simultaneously has high conductivity, but by careful manipulation of the energy levels in the material this can be achieved [51]. For this, an impurity in a form of a metal or a metal oxide is added to another metal oxide to achieve the required properties. By this addition of impurity atoms highly degenerate materials can be developed which have higher conductivity.

Table 2.1: Typical range of values for a TCO.

Band Gap(eV)	Transmittance (%)	Resistivity (Ωcm)	Sheet Resistance ($\Omega/\square$)
>3	75-85 (in 300 to 1200 nm wavelength)	10^{-4}-10^{-3}	10-50

The first TCO thin film was developed in the year 1907 [52]. This was a thin film of CdO prepared by thermally oxidising a vacuum sputtered film of cadmium metal. Due to the poisonous nature of cadmium, this TCO is not used now. In this section, the three most widely used TCO materials, namely Indium Tin Oxide (ITO), Hydrogenated Indium Oxide(IO:H) and Aluminium Doped Zinc Oxide (AZO) are discussed with respect to their material properties.

Indium Tin Oxide (ITO)

The most widely used TCO in solar cell application is Indium tin oxide (ITO) owing to its lower resistivity as compared to other available TCOs. ITO is a n-type degenerate (degenerate meaning that the fermi level lies in the conduction band) as shown in figure 2.6. It is a wide band gap semiconductor that has low electrical resistivity due to its high free carrier density. By adding tin to indium oxide structural changes happen which is the reason for the electrical properties of ITO. The electrical properties of ITO are defined by the free carrier concentration N, carrier mobility μ and conductivity σ, which are mathematically related as,

$$\sigma = e.N.\mu \tag{2.1}$$

The conductivity of ITO can be increased by increasing the free carrier concentration or by increasing their mobility. By addition of tin atoms the free carrier concentration can be increased but there is a theoretical maximum which limits the concentration [53]. This maximum carrier density N can be mathematically defined as,

$$N_{max} = N_{in}.C \tag{2.2}$$

N_{in} is the concentration of indium atoms which is equal to $3{\cdot}10^{22}cm^{-3}$ and C is the concentration of tin atoms. This maximum occurs because a majority of tin atoms at higher doping levels are deactivated. This is caused by the fact that the higher the tin content, the more is the probability of the tin ions occupying the nearest-neighboring anion site hence forming neutral defects. Also the transmittance starts to decrease if the carrier concentration is increased owing to the free carrier absorption, so it is of great importance to improve the mobility. Mobility is influenced by the scattering phenomenons in the ITO structure. Some of the sources of scattering which may influence the free carrier mobility can be defined as, ionized impurity scattering, neutral impurity scattering, grain boundary and external surface scattering, acoustical phonon scattering, defect lattice scattering, etc [54].

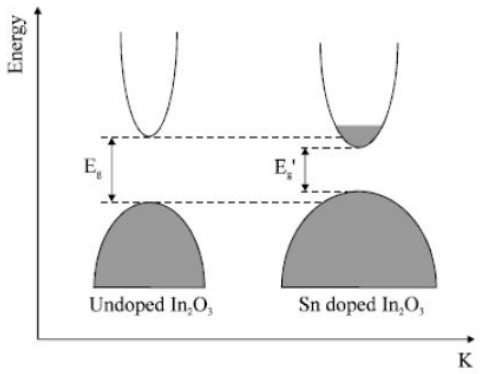

Figure 2.6: The Parabolic energy dispersion diagram of undoped indium oxide and the effect of tin doping [10].

The high optical transmittance of ITO originates from its wide bandgap, it has a direct bandgap of around 3.75 eV. The work from some researchers pointed to a bandgap with a value between 3.5 to

4.06 eV [55–57]. Optical properties of ITO are influenced by many types of electronic excitation: band gap transitions, interband transitions from the bulk of the valence band into the bulk of the conduction band and intraband transitions of free electrons in the conduction band (free carrier absorption). From these excitations three different regions can be explained in the ITO transmission curve. The ultraviolet region (high energy) shows a strong absorption edge, known as the band edge which is governed by the ITOs band gap transition. In the visible wavelength range quite high transmittance is present. Going to the infrared region a strong increase in absorption takes place at the so-called plasma edge which is associated with the excitation of free electrons in the conduction band.

Hydrogenated Indium Oxide (IO:H)

The demand for high mobility TCO's is increasing not only in photovoltaic industry but also in semiconductor industries. To feed these demands new TCO's based on indium oxide have been developed. The best out these is Hydrogenated Indium oxide (IO:H). A major work on the development of this TCO for applications in c-Si cells and CIGS based photovoltaic cells has been ongoing from the last decade [58, 59]. As compared to ITO, IO:H has high mobility(exceeding 100 cm^2/V.s) and high near IR transparency [58]. These two properties give an edge to IO:H over ITO, hence it can be used as an alternative to ITO. The high mobility in case of IO:H has been attributed to the presence of amphoteric hydrogen in the structure. The presence of substitutional hydrogen, which replaces oxygen, leads to a reduced impurity scattering. As impurity scattering is the limiting factor for mobility, the reduced impurity scattering translates to high mobility [60]. The higher mobility of IO:H films allows a lower doping concentration for equal conductance. Thus an enhanced optical transmission is possible specifically in the IR region which is in accordance with Drude theory.

The utilisation of double layers of IO:H and ITO have also gained a lot of interest, specifically in use as front contact for silicon heterojunction cells. In these case, the properties of the double layer are optimised in such a way the electrical and optical properties are dictated by IO:H whereas the good electrical connection between silver and ITO gives a low resistance contact between the doped layers and metal contacts. Due to scarce nature of indium in the earth's crust, there are some concerns regarding the widespread use of ITO and IO:H, as they are not only used in solar cell manufacturing but are also employed as transparent electrodes in flat-panel displays, light-emitting diodes, electrochromic windows [61, 62].

Aluminium Doped Zinc Oxide (AZO)

Owing to the relative low abundance of indium in the earth's crust as shown in figure 2.7 and no specific indium mines, it can be estimated that there will be a huge supply demand imbalance in the next 20-30 years.

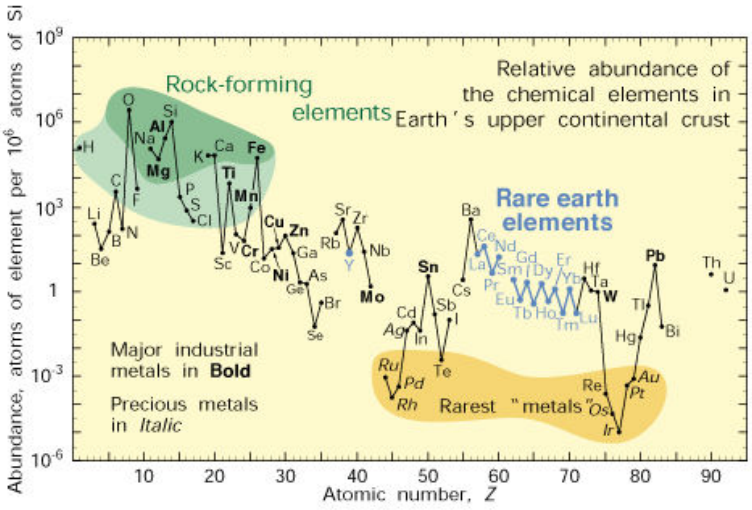

Figure 2.7: Abundance (atom fraction) of the chemical elements in earths upper crust as a function of atomic number [11].

This has lead to the development of new materials which have comparable properties as ITO. Aluminum doped zinc oxide (AZO) is the front runner in this aspect.

ZnO is composed of abundant elements, the abundances of Zn and Oxygen in the earth crust are 132 ppm and 49.4%, respectively [63]. Zinc oxide is a compound semiconductor with a band gap of nearly 3.2 eV which crystallizes in the hexagonal wurtzite structure, explained by William Bragg in 1914, shortly after the discovery of X-ray diffraction [64]. The hexagonal unit cell of ZnO, contains two ZnO molecules, in which the Zn atoms are surrounded tetrahedrally by oxygen atoms.

In comparison to ITO, there is a certain difference in, how the electrical properties vary for AZO. Other than the mobility and carrier concentration, the morphology of the film also determines the conductivity. The Modified Thornton-structure-zone model depicts how the material grows with respect to the pressure and temperature of deposition [65]. Specific zones/growth regime can be identified from this diagram. By targeting the specific growth regime, specific properties can be obtained.

There are various deposition techniques available to deposit TCO. Some of the techniques that are frequently used are Thermal evaporation, Chemical Vapor Deposition (CVD), Spray Pyrolysis (SP) and RF Sputtering. In this work, the TCO deposition was done by RF magnetron Sputtering in the machines-Amigo and Zorro respectively.

2.3. Experimental Methodology

This section is divided into three sub parts: sample preparation, thin film deposition and characterisation techniques.

2.3.1. Sample Preparation

To produce high efficiency photovoltaic cells and high quality film, clean substrates are essential. To do so we used chemical baths to remove any unwanted particle or residue before actual deposition could be done. Also it is worthwhile to mention that the substrate holders were also cleaned using acetone and isopropylalchohol (IPA), to maintain high quality.

The thin film samples used in this thesis were fabricated with both glass and Asahi VU (SnO_2:F) substrates. Corning Eagle XG glass was used mainly to test deposition conditions and as-deposited samples. For cell fabrication Asahi VU glass, which is coated with a textured Fluorine doped tin oxide (FTO) having a root mean square roughness of 34 nm was used [66]. Cleaning process involved the following sequential steps :

- Dipped in acetone for 10 minutes.
- Dried using nitrogen.
- Dipped in isopropylalchohol (IPA) for 10 minutes.
- Dried using nitrogen.

2.3.2. Thin-film Deposition Technique

In this section the development methodology for the deposition of hydrogenated amorphous silicon oxide (a-SiO_x:H) layers, the required cell and transparent conductive oxides will be explained.

Plasma-Enhanced Chemical Vapour Deposition (PECVD)

PECVD is a type of chemical vapour deposition in which gas phase chemical reactions lead to deposition of materials on the substrate. As the energy is supplied by plasma, so the temperature required for depositions is low as compared to atmospheric pressure or low pressure CVD. One of the advantage of this process is that by manipulating the gas flows in the deposition processing chambers (DPC), one can alter the properties or make different kinds of the layers. In this process, different gases can be mixed together. This mixture is then ignited into a argon atmosphere to create a plasma through the application of electric field at radio frequency (13.56 MHz) or very high frequency (40 Mhz). These frequencies are internationally agreed upon for use in scientific applications for material depositions. After the plasma is fired, the electrons are accelerated. This leads to ionisation of precursor gases through collisions leading to formation of charged radicals. The substrate is kept grounded with a lower potential than the plasma (plasma is at positive potential), thus only neutral or positively charged particles can diffuse towards it, which form the thin-film layer. A schematic of a PECVD chamber is shown below in figure 2.8.

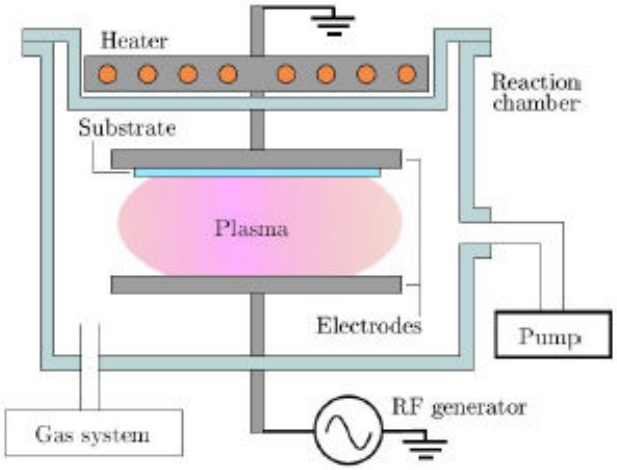

Figure 2.8: A schematic of a PECVD chamber [12].

Deposition of the amorphous silicon oxide (SiO_x) layers involves the use of three precursor gasses: silane (SiH_4), carbon dioxide (CO_2) and hydrogen (H_2). The p and n doped layers were developed by adding diborane (B_2H_6) and phosphine (PH_3) gases to the mixture respectively. The distance between substrate and electrode is kept constant at 1.4 cm for p-layers, i-layers and 2.1 cm for n-layers [66]. This distance is also an important parameter in defining the structural properties of the films deposited [67]. Throughout this work, all the layers of amorphous silicon oxide (a-SiO_x:H) were deposited using PECVD apparatus called Amigo by Elettorava S.p.A as shown in figure 2.9.

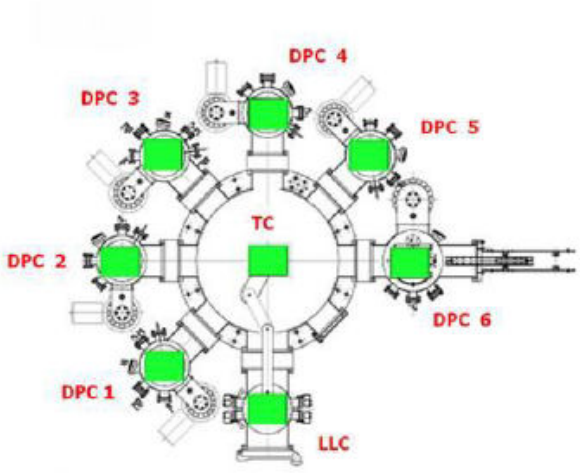

Figure 2.9: A schematic of PECVD apparatus used in this work (Amigo) [9].

This is a 6-chamber thin-film processing system consisting of a load-lock chamber (LLC), a transfer chamber (TC), p-type layer chamber (DPC1), n-type layer chamber (DPC2), amorphous i-layer chamber (DPC3), μ c-Si:H layer chamber (VHF, DPC4), multi-process chamber (DPC5), and a sputtering chamber (DPC6) for AZO deposition. This system is fully automated with the ability to handle 5 substrates. Only DPC 1,2,5 and 6 were utilised for material development. For the deposition of AZO, the DPC6 of the amigo machine is used as shown in figure 2.9. It contains a 6 inch (diameter) circular ceramic target of ZnO/Al_2O_3 (98/2 % by weight).

RF magnetron Sputtering

RF magnetron Sputtering is a type of physical vapour deposition technique where both a plasma and a magnetic field are used in combination to achieve high quality films. The magnetic field provided

by a magnet placed underneath the target is to increase the utilisation of secondary electrons. The plasma, which is composed of ionised argon gas, contains positive argon ions which are bombarded on the target by application of a voltage bias. The target is kept at a negative potential and the substrate is at a positive potential. Although there are various methods to deposit TCO's, such as DC sputtering, spray pyrolysis etc. In this thesis, the TCO's developed are by RF Magnetron Sputtering owing to the several advantages in comparison with the other physical chemical deposition methods such as, a low-temperature ion–assisted deposition, the before/post deposition modification of substrate/thin - film surface, change of deposition rate in wide range, to control further parameters which are important for thin film growth (substrate temperature, plasma density, composition of working gas, ion bombardment of film during deposition) and uniform depositions [68]. A schematic of RF magnetron sputtering is shown in figure 2.10.

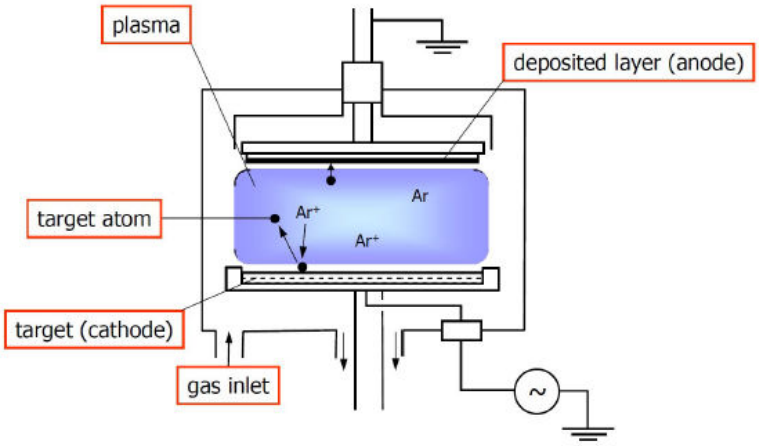

Figure 2.10: A schematic of RF magnetron Sputtering, image courtesy: Dr.Rene van Swaaij .

The ITO and IO:H films were deposited in RF magnetron sputtering unit (Zorro) in Else Kooi Laboratory-TU Delft. This unit consists of two deposition processing chambers- one for hydrogenated indium oxide and the other for indium tin oxide. A circular ceramic target of 4 inch (diameter) of indium oxide and tin oxide (90/10 % by weight) was used, in the depositions of ITO.

Physical Vapour Deposition

Metal deposition is required in various stages of cell development, such as to measure activation energy of a layer or for front and back contacts of the cells. In this work, aluminium is deposited by electron beam even though its melting point is not to high, because it can form alloys with the tungsten boat. In this work, all the metal depositions were done by using metal evaporation. A high vacuum PRO500S metal evaporator by Provac is used to deposit metal. The system, depicted in figure 2.11, is fully automated. This machine utilises two types of process, thermal evaporation for metals with low melting points (silver) and electron beam evaporation for high melting point materials. A tungsten boat is used for depositing Ag using thermal evaporation. Four ceramic crucibles, each containing a different material, used for evaporating Al or other metals by electron beam evaporation. The reaction chamber, equipped with a rotating stage, can accommodate up to four 10x10 cm^2 substrates. A rotating stage is used, so as to maintain uniform depositions and improved step coverage. The chamber is kept at very high vacuum (approx.10^{-5} mbar) to avoid oxidation.

2.3.3. Characterisation Techniques

To ascertain the optical and electrical quality of the films developed as well as to characterise the photovoltaic cells fabricated in this work various techniques are used. In this section all the techniques which were utilised are mentioned. These techniques can broadly be divided in two parts, the first six are the electrical techniques and the others are optical techniques. Finally, towards the end the way how the efficiencies are determined in this work is mentioned.

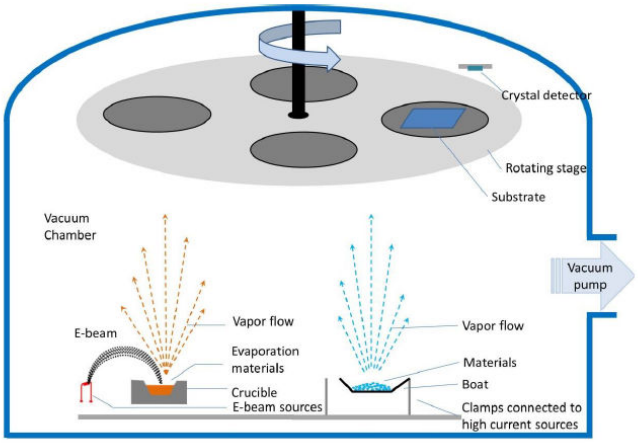

Figure 2.11: A schematic of Provac PRO500S, showing the two methods of metal evaporation. Electron beam (E-beam) is shown in the left and thermal evaporation is in the right [9].

Activation Energy

Activation energy is one of the most important parameter, which is used in determining the level of doping in a layer. The activation energy (E_{ac}) is defined as the energy difference between the conduction band energy level and fermi level for a n type material and as the difference between the fermi level and valence band for a p type material. In case of materials based on amorphous silicon and its alloys, this measurement becomes more important. One of the reason is that the a-Si and its alloys suffer from a phosphorus doping paradox [33]. In these materials, phosphorus atoms are bonded to three silicon atoms i.e. threefold configuration. This is associated to the chemical advantage in forming three bonds and the absence of a rigid lattice. Hence the doping in this case is not as efficient as in case of crystalline silicon. So to develop good n layers one needs to calibrate the level of phosphine in the deposition process. Thus determining activation energy becomes an important task. Also from activation energy one can get an idea of the built in voltage in the cell which can be used as a parameter in determining the maximum achievable open circuit voltage. For an activation energy measurement, a layer of doped material was deposited on Corning eagle XG glass. Two strips of 500 nm aluminium with fixed dimensions and distance, were evaporated on top of the deposited layer. Then the electrical conductance of the layer was measured by applying a voltage on the contact strips and measuring the resultant steady-state current using Keithley 6517A electrometer. This was done in dark, so as to avoid any photogeneration of carriers. The activation energy of the layer was extracted by taking a linear fit in the $ln(\sigma(T))$ and $1/kT$ plot, also referred as Arrhenius plot. The slope of this linear fit gives the activation energy. Mathematically the relation between activation energy and dark conductivity can be written as,

$$\sigma(T) = \sigma_o \cdot e^{\frac{-E_{ac}}{kT}} \tag{2.3}$$

where, E_{ac} is the activation energy, T is the temperature, K is boltzmann's constant and σ_o is the conductivity pre-factor [69].

Illuminated Current density-Voltage (J-V)

The estimation of Current density-Voltage curve under standard test conditions (STC) is vital in characterising the solar cells. Irradiance of 1000 W/m^2, AM 1.5 spectrum and temperature of 25°C (called as STC conditions) are used in determining the parameters of the photovoltaic cell. All the parameters that define the efficiency of the cell can be determined from this measurement. Wacom WXS-156S-L2 solar simulator was used in this work for determination of J-V curves, it has a cooling system that maintains temperature of 25°C. A halogen lamp and a Xenon lamp are used to simulate AM 1.5 spectrum in this apparatus. The J-V curves provide external parameters such as open circuit voltage (V_{oc}), short circuit current (J_{sc}), fill factor (FF), series and shunt resistances (R_s and R_{sh} respectively) and efficiency.

External Quantum Efficiency

External Quantum Efficiency (EQE) is defined as the ratio of charge carriers collected across a solar cell to the number of photons incident on the cell. To determine the number of charge carriers collected the current generated by the solar cell at short circuit condition is divided by the elementary charge. For the number of incident photons the total power incident (AM1.5g spectrum) on the solar cell is divided by the photon energy. Taking the ratio of these two the EQE is determined. By, multiplying the photon flux ($\phi(\lambda)$) as a function of wavelength, with the EQE of the cell which is measured at the short circuit conditions, the J_{sc}can be calculated. Mathematically the following relations are used in the calculations of the short circuit current (J_{sc}),

$$J_{sc} = -\int_{\lambda_{min}}^{\lambda_{max}} \phi(\lambda) \cdot EQE(\lambda)_{cell} \cdot e \cdot d\lambda \tag{2.4}$$

Another aspect of EQE that has been utilised in this thesis is the dependence of EQE on bias voltage. To specifically see how the response of cell varies in specific wavelength spectrum, a bias voltage is given to the cell and the EQE is measured. From these results, it is quite easy to identify the regions of the cells having defects, as by applying a bias voltage (negative voltage was used in this work) only the electrical parameters are changed where as the optical parameters (reflectance, transmittance etc) remain constant [70].

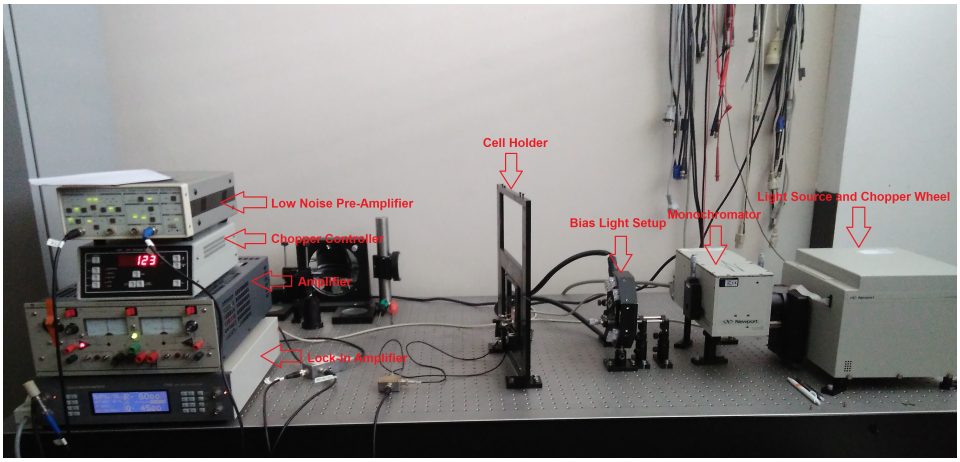

Figure 2.12: Actual image of EQE set-up used in this work.

The EQE measurements were done by a set up developed in TU Delft, as shown in figure 2.12. Before each measurement a calibration step is performed with a reference silicon diode. Two gold wires are used as contacts for the cell. The light from Xenon lamp is filtered by a chopper wheel and a monochromator, such that a specific wavelength of light is focused on the cell. Steps of 10 nm are used to get the measurement points. The frequency of the chopper is set at 123 Hz by a chopper controller which is coupled with a lock in amplifier (EG&G 7260DSP). The cell is maintained at short circuit conditions so as to measure the current developed, which is done by an electrometer. This process uses the lock in amplifier so as to improve the signal to noise ratio. Finally, the signals are analysed by the computer and presented as a plot of EQE.

Four Point Probe

Four point probe method was applied to get the resistivity Ωcm and sheet resistance ($\Omega/\square$) of the TCO films. In this method four probes with a specific spacing and dimensions are put on the film. Current (I) is supplied by two probes and the other two probes are used to measure the voltage (V). The ratio between the two is then used to calculate the resistivity of the film. Taking into account the dimensions and the spacing between the probes the following mathematical relation is used to calculate the resistivity,

$$\rho = \frac{\pi \cdot t \cdot V}{\ln(2) \cdot I} \tag{2.5}$$

In the above equation, the term π/ln(2) is equal to 4.53 and t is the film thickness. To make the calculation easy to comprehend the value of current is set at 4.53 mA. From the value of resistivity, the value sheet resistance (ρ_{sheet}) is deduced as,

$$\rho_{sheet} = \frac{\rho}{t} \tag{2.6}$$

In this work, the Advanced Instruments Technology CMT-SR2000NW was used to measure resistivity and sheet resistance of the TCO layers

Hall measurements

In identifying, the best TCO films it becomes imperative to compare the majority carrier concentration and the mobility in addition to sheet resistance and resistivity. A larger mobility and carrier concentration are the desired properties for a TCO. To do so Hall effect in conjugation with Van Der Pauw method is used. The Hall effect is a consequence of the forces that are exerted on moving charges by mutually perpendicular electric and magnetic fields. These forces called as Lorentz force in steady state lead to a development of a voltage, which is defined as hall voltage (V_H). By measuring this voltage the majority charge carrier mobility and concentrations are determined.

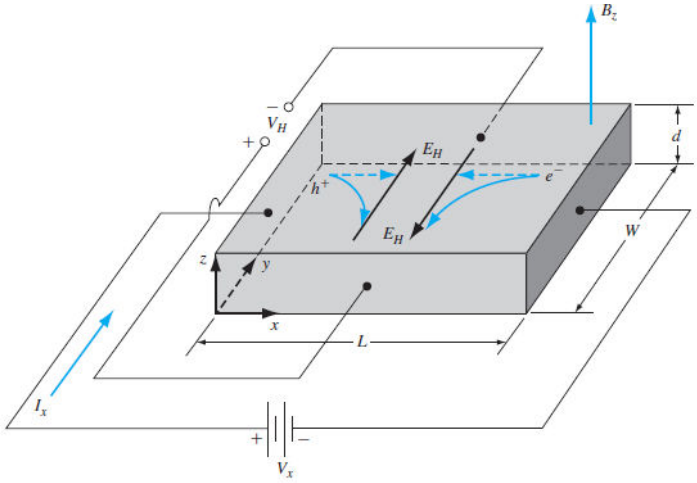

Figure 2.13: Schematic for Hall Effect measurement [13].

Mathematically, the relation between hall voltage and majority carrier concentration (n) can be written as,

$$n = -\frac{I_x \cdot B_z}{e \cdot d \cdot V_H} \tag{2.7}$$

The directions taken in above equation are based on the figure 2.13, e is the elementary charge [13]. The important thing to account is that the above formula is defined for a n type semiconductor and the hall voltage is negative, hence the carrier concentration becomes positive. Thus from the calculation of hall voltage, one can get the mobility as per the below formula,

$$\mu_n = \frac{I_x \cdot L}{e \cdot n \cdot W \cdot d \cdot V_H} \tag{2.8}$$

For the measurement of sheet resistance (R_S) and resistivity, the Van der pauw technique is used [71]. This technique utilises the following equations,

$$e^{-\pi \cdot R_A/R_S} + e^{-\pi \cdot R_B/R_S} = 1 \tag{2.9}$$

$$R_A = V_{43}/I_{12} \tag{2.10}$$

$$R_B = V_{14}/I_{23} \tag{2.11}$$

The above formula is based on figure 2.14 [14]. The resistivity can be calculated by multiplying the sheet resistance with the thickness of the film. For a sample shown in figure. 2.14, V_H is determined by performing measurements with constant current I and magnetic field B applied perpendicular to the plane of the sample. By forcing a current I through contacts 1 and 3, V_H can be measured across the other two contacts.

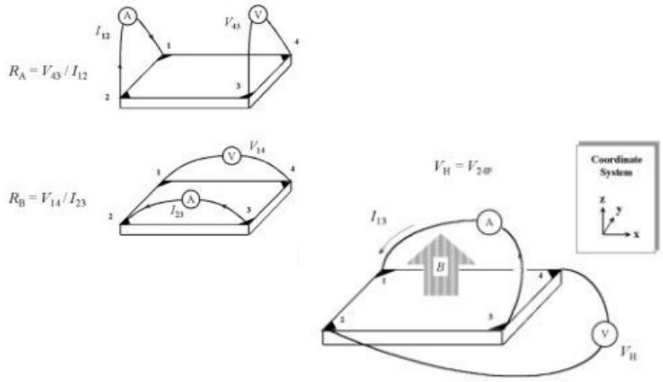

Figure 2.14: Schematic for Van der pauw technique [14].

In this work Ecopia HMS-5000 Hall Effect setup was used for the measurements of the TCO developed.

Electroluminescence

Identification of shunt paths is really important to characterise large area cells. In this work Electroluminescence (EL) is used as a technique to identify the spots where material defects are present. Eventhough in photovoltaic industry, this technique is applied to c-Si module as a method of contact less photographic surveying method. Simply put this method utilises the radiative recombination mechanism that happens when electrons and holes combine to give out radiation. By estimation of the emitted photons or radiation one can estimate the material properties at that point. A forward bias is given to the cell, so as to inject excess charge carriers in the cells to facilitate the radiative recombination. Then the cell is photographed by an infrared camera in dark to get a high resolution image. The reason to use infrared camera is because the dominant emission spectrum for a crystalline silicon cell is between 900 to 1100 nm [72]. A Nikon D7200 camera with a IR lens and a DC power supply is used in this work.

Spectrophotometer

Spectrophotometer is used for the correct estimation of the optical properties (reflection, transmittance and angular intensity distribution) associated with the films and the TCO developed. From the measurements of reflectance and transmittance, we can estimate the absorptance in the spectral range of 300 - 1200 nm which is selected on account of the absorption associated with the silicon cells used in this work. In this thesis, a Perkin Elmer Lambda 950 spectrophotometer is used. It utilises a deuterium arc lamp for ultraviolet light and a tungsten-halogen lamp for visible and infrared light. This apparatus is used with an Integrating Sphere (IS) to get the required optical parameters. The measurements of reflection and transmittance were done utilising integrating sphere as shown in figure 2.15.

The sphere has a diameter of 150 mm and is coated with a highly reflective material. This is done to make light inside the sphere homogeneous [73]. By comparison with a reference beam the values of reflectance (R) and transmittance (T) are deduced. For calculation of absorptance (A) by the film following relation is used.

$$A = 100 - (R + T) \tag{2.12}$$

The correction for the absorptance in the glass substrate has to be taken into account when using the above formula. All the above values are in percentages as they are taken relative to the reference beam.

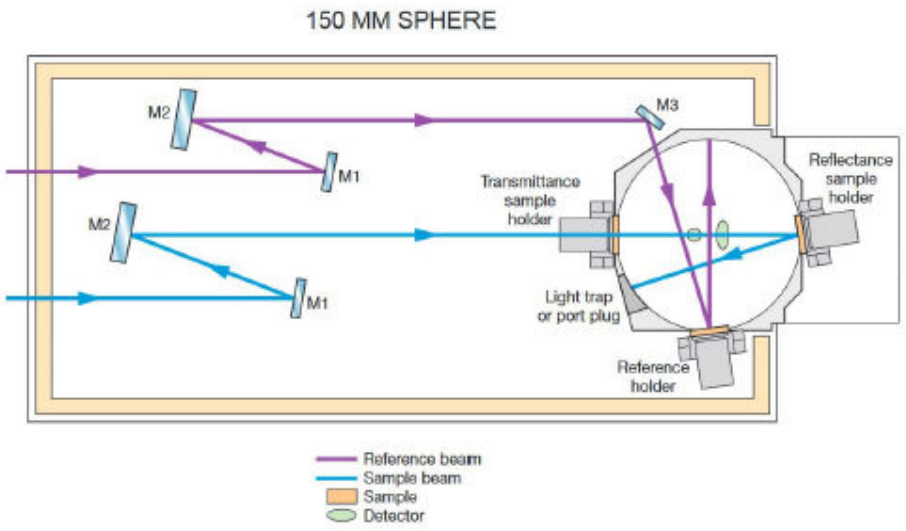

Figure 2.15: A schematic of Lambda with the integrating sphere set-up used in this work [15].

Spectroscopic Ellipsometry (SE)

Ellipsometry is an optical measurement technique that characterizes light reflection from samples [74]. The key feature of ellipsometry is that it measures the change in polarized light upon reflection from a sample. This makes ellipsometric measurement very precise and reproducible. The name 'ellipsometry' comes from the fact that polarized light often becomes 'elliptical' upon light reflection. Ellipsometry measures the two values Ψ and Δ. These represent the amplitude ratio Ψ and phase difference Δ between light waves known as p- (parallel) and s- (perpendicular) polarized waves. Mathematically, these two values are related by what are called as fundamental equations of ellipsometry [75]. These equations are derived by using Fresnel equations and reflection coefficients (r^p and r^s). In short, the most important equations are shown below,

$$\rho = \tan(\Psi) \cdot e^{j \cdot \Delta} \tag{2.13}$$

$$\rho = R^p / R^s \tag{2.14}$$

$$R^p = |r^p|^2, R^s = |r^s|^2 \tag{2.15}$$

Using SE, the optical constants i.e. real part of the refractive index (n), extinction coefficient (k) and thickness of a thin film layer are deduced. From the measurement of k, the absorption coefficient is also calculated and ultimately from it the optical bandgap is computed. But this requires some fitting methods which depend on the type of thin film layer. A M-2000 Ellipsometer by J.A. Woollam Co. was utilised in this work to acquire the thickness and optical constants of the films developed.

Calculation of Efficiency

Thirty thin film cells with dimensions of 4 mm and 4 mm are developed on Asahi VU substrate (10X2.5 cm^2). For cells with transparent back contacts, 24 cells of 5 mm by 5 mm are developed on the Asahi VU substrate. To calculate the efficiency of the cells developed in this work, the mean values of the best 10 cell's (otherwise stated) open circuit voltage, short circuit current density and fill factor. All the plots showing these parameters have error bars, the standard deviation was calculated from the values obtained. To get the precise estimate of efficiency the short circuit current density measured from EQE set up was used instead of the Wacom values. This was done due to the fact that the EQE setup takes into account the AM1.5g spectrum, hence the chance of spectral mismatch occurring due to the light source is reduced. Also the mismatch occurring due to illuminated area is also taken care of in the EQE setup as well as the overestimation of the short circuit current due to lateral current collection is excluded [76]. All the current density (J)-voltage (V) curve were scaled according to the value of short circuit current obtained from EQE setup.

3

Theoretical Efficiency Estimation of The Four Terminal Solar Cell

3.1. Introduction

Two important issue while developing four terminal cells, are the determination of the optimum combination of cells to be utilised, and the efficiency gain that can be realised. To accomplish these two goals, theoretical calculations utilising two parameters namely, Response 4T (R_{4T}) and Spectral Response 4T (SR_{4T}) are performed in this chapter. This chapter also explains the advantage of using an a-SiO_x:H based top cell instead of a-Si:H based top cell.

3.2. Response 4T (R_{4T}) and Spectral Response 4T (SR_{4T})

In this section, two parameters called Response 4T (R_{4T}) and Spectral response 4T (SR_{4T}) are provided as a suitable approach to determine the best suited configuration for the four terminal cells.

Here, first the parameter called Response 4T (R_{4T}) is defined. Mathematically, as shown below,

$$R_{4T} = \frac{EQE(\lambda) \cdot V_{oc} \cdot FF \cdot e \cdot \lambda}{hc} \tag{3.1}$$

In the above equation, h is the Planck's constant and c is the speed of light in vacuum. This unitless parameter relates the wavelength dependent external quantum efficiency (EQE(λ)), the open circuit voltage V_{oc}, fill factor (FF) of the cell and elementary charge (e) with the energy of the photon at the corresponding wavelength. Although this term signifies the efficiency but one important thing to keep in mind is that this efficiency is independent of the spectrum of incident light. Thus this is a universal term. The actual estimation of the efficiency gain at standard test conditions (STC) is not possible from this term alone as the spectrum of incident light is required to determine the value of efficiency. This parameter can only be used to identify the best possible combinations.

Table 3.1: Electrical Parameters of the thin film cells [29].

Cell	V_{oc}(V)	J_{sc}(mA/cm^2)	Fill Factor	Efficiency(%)
a-Si:H	0.875	15.19	0.66	8.78
a-SiO_x:H	1.02	12.3	0.70	8.80

There are many options that can be applied as the top cell, but at PVMD the focus is on thin film solar cells. We have two available options that can be used as the top cell in our application- a-Si:H based cell and high band gap material a-SiO_x:H based cell [29]. The parameters of these cells are mentioned in table 3.1. Both the cells were developed in the Else Kooi Laboratory-TU Delft. It can be argued that EQE plots could be used for choosing the best cell, but the main aim of our work is to obtain high efficiency for the four terminal cell. Thus only EQE can not become the differentiating factor. That is the main reason for using R_{4T} parameter. To deduce which one of the two is more

suitable for application- we must look at the R_{4T} plot of the two cells. The one that has higher values of R_{4T} in the wavelength range from 300 to 600 nm will give the best efficiency gain in our application. The reason for choosing this range lies in the fact that the bottom cell will be working at its maximum in the range from 600 to 1200 nm. This will also become more clear in the following paragraphs. The plots of R_{4T} made for a-Si:H cell and the a-SiO_x:H is shown in figure 3.1. The plot makes it clear that a-SiO_x:H has higher R_{4T} values in the required spectral range.

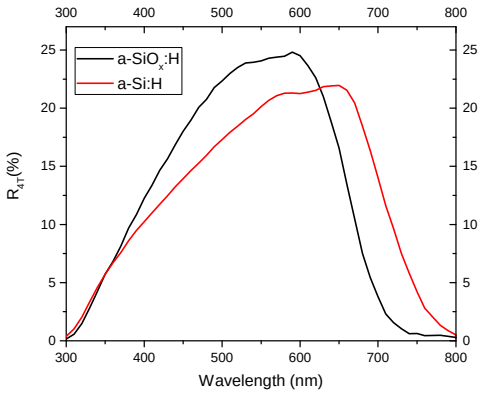

Figure 3.1: R_{4T} comparison between a-Si:H and a-SiO_x:H cell.

The motivation for using high bandgap (1.8-2 eV) materials also comes from literature. A high bandgap top cell translates into a high open circuit voltage, which in our case, leads to a high V_{oc} and fill factor product. This is the most important parameter in determining the efficiency of the four terminal stack [77]. Various simulation studies and models developed in the literature have shown that a top cell with a high bandgap (1.8-2.2 eV) even though with a low efficiency under STC (8-14%) when coupled with a high-efficiency c-Si cell can result in efficiencies exceeding Richter limit [22, 78].

Using the highest efficiency a-SiO_x:H cell with parameters mentioned in table 3.1, as the top cell in combination with the poly-Si, Interdigitated back contact (IBC) and Silicon heterojunction (SHJ (Hybrid)), the plots of R_{4T} are generated. Two cells of each type are compared, all of which were developed in the PVMD group. The parameters of the bottom cells are mentioned in the table 3.2 for the poly-Si (Poly), IBC and SHJ (Hybrid) cells.

Table 3.2: Electrical Parameters of the bottom cells used in the calculations.

Bottom cell	V_{oc}(V)	J_{sc}(mA/cm^2)	Fill Factor	Efficiency(%)
Poly-1	0.68	32.67	0.64	14.22
Poly-2	0.68	33.60	0.68	15.54
IBC-1	0.68	35.68	0.72	17.48
IBC-2	0.70	40.80	0.70	20.00
SHJ (Hybrid)-1	0.69	37.20	0.71	18.22
SHJ (Hybrid)-2	0.69	38.40	0.71	18.81

In the figure 3.2, the R_{4T} plots for different cell combinations are given to identify the gain in utilising the four terminal configuration. It is imperative that the difference between the area shown in indigo colour and the lime should be positive. Essentially this is the area which when translated into efficiency provides the enhanced efficiency of the four terminal device. But a true estimate of the efficiency gain from this single parameter alone is not correct, as it does not take into account the spectrum under which the measurements are taken.

By looking at the plots in figure 3.2 it may look that there is an advantage in using the four terminal topology, but it would be more clear with a new parameter defined in this work as the Spectral Response 4T (SR_{4T}), which is the product of the response 4T parameter with the photon flux ($\phi(\lambda)$) at the specific wavelength. To calculate the photon flux (ϕ), AM 1.5 (Global spectrum) was used. For the AM 1.5 (Global) spectrum, data from American Society for Testing and Materials (ASTM), Terrestrial Reference

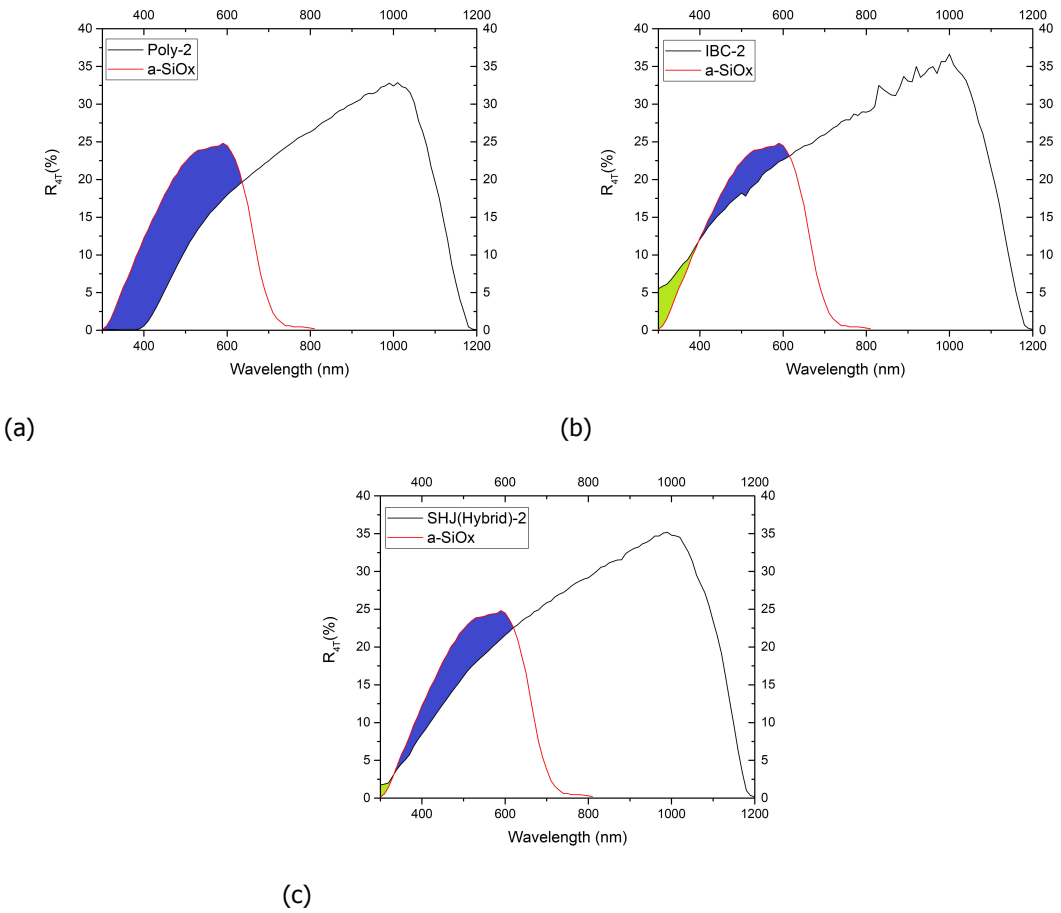

Figure 3.2: R_{4T} comparision with (a) the best poly-Si cell (Poly-2). (b) the best IBC cell (IBC-2). (c) the best SHJ (Hybrid) cell (SHJ (Hybrid)-2).

Spectra for Photovoltaic Performance Evaluation was used [16]. This is done because AM 1.5 spectrum is used as the standard test condition to determine the efficiency. The integration of this plot with respect to wavelength yields a value of 1000 Wm^{-2} as show in figure 3.3.

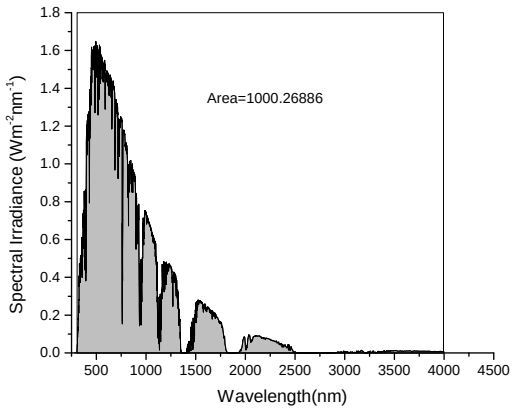

Figure 3.3: The AM 1.5 global Spectrum as shown with the area of 1000 W/m^2 [16].

Mathematically, the spectral irradiance ($I(\lambda)$) as a function of wavelength at AM 1.5 can be related to the photon flux at that wavelength as shown below,

$$\phi(\lambda) = \frac{I(\lambda) \cdot \lambda}{hc} \tag{3.2}$$

Finally, the spectral response 4T (SR_{4T}) can be defined mathematically,

$$SR_{4T} = \frac{EQE(\lambda) \cdot I(\lambda) \cdot \lambda \cdot q \cdot V_{oc} \cdot FF}{hc} \tag{3.3}$$

The quantity SR_{4T} has a unit of $Wm^{-2}nm^{-1}$, which is same as that of spectral irradiance. To take into account all the units involved in the calculations a factor of 10^{-9} is multiplied to the results obtained from the equation 3.3. A detailed derivation is given in appendix B.1.1. In literature, Spectral Response 4T (SR_{4T}) has been mentioned as spectral efficiency [79]. Although calling this term as efficiency is not correct as the units of this term are $Wm^{-2}nm^{-1}$. These SR_{4T} plots are helpful in determining the maximum possible four terminal device performance because the power output of the cells can be compared directly at any desired wavelength in the AM 1.5 spectrum.

The integral of the plot of SR_{4T} with λ (wavelength), when divided by the total spectral irradiance at AM 1.5, gives the efficiency of the cell at AM 1.5. Thus the area of these plots can be translated to the efficiency of the cell at AM 1.5. The indigo area in the figure 3.4 can be translated into the increased efficiency ($\eta_{Increase}$). But the area marked in lime colour needs to be subtracted so as to correctly estimate the efficiency gain. So η_{Total} of the four terminal configuration, becomes the sum of efficiency of the bottom cell without the top cell (η_{Bottom}) plus the efficiency gain from the top cell ($\eta_{Increase}$). Mathematically, this can be explained as

$$\eta_{Total} = \eta_{Bottom} + \eta_{Increase} \tag{3.4}$$

In the plots of SR_{4T}, the gain in the efficiency of the four terminal configuration is estimated from the difference between the area shaded by the indigo and the lime color, in figure 3.4a for the best poly-Si cell, figure 3.4b for the best IBC cell and figure 3.4c for the best SHJ (Hybrid) cell. From this area, the total achievable efficiency rise is estimated, which is provided in the table 3.3. This table contains all the bottom cells as shown in figure 3.4.

Comparing SR_{4T} for IBC bottom cells with the SHJ (hybrid) cell it can be seen that the effective area rise is more in case of SHJ (hybrid) bottom cells. This area is maximum when a poly-Si cell is used as the bottom cell. A reason behind this is that, the poly-Si cell has poor response in the blue green region (due to absorption in poly-Si layers).

Even though the shading by front electrodes is lower (non-existent) for the IBC cell as compared to SHJ (Hybrid), which is clear from the lower efficiency of the best SHJ cell (SHJ (Hybrid)-2) in the set of cells, at 18.81% in comparison to the best IBC cell (IBC-2) of approximately 20%, the absolute gain ($\eta_{Increase}$)) is higher for SHJ (Hybrid) cells in the four terminal configuration as seen in table 3.3. The efficiency gain can be improved if the response of the top thin film cell is improved in the 300 to 600 nm spectral range. This is because the photons in this range are absorbed in the top cell.

Also one interesting observation is that, when a lower efficiency cell (poly-Si) is utilised as the bottom cell, the gain of utilising the four terminal approach is more prominent, eventhough the total efficiency is lower than 20%.

Table 3.3: Total efficiency that can be obtained in four terminal configuration.

Bottom Cell	η_{Bottom}(%)	$\eta_{Increase}$(%)	η_{Total}(%)
Poly-1	14.22	3.94	18.16
Poly-2	15.54	3.69	19.23
IBC-1	17.48	1.32	18.80
IBC-2	20.00	0.82	20.82
SHJ (Hybrid)-1	18.22	1.87	20.10
SHJ (Hybrid)-2	18.81	1.64	20.45

From the results of the table 3.3, it can be seen that a gain of almost 4% can be obtained when an a-SiO_x:H top cell is used with a poly-Si cell in four terminal configuration. Gain between 1% and 4% can be realised by simply utilising four terminal topology.

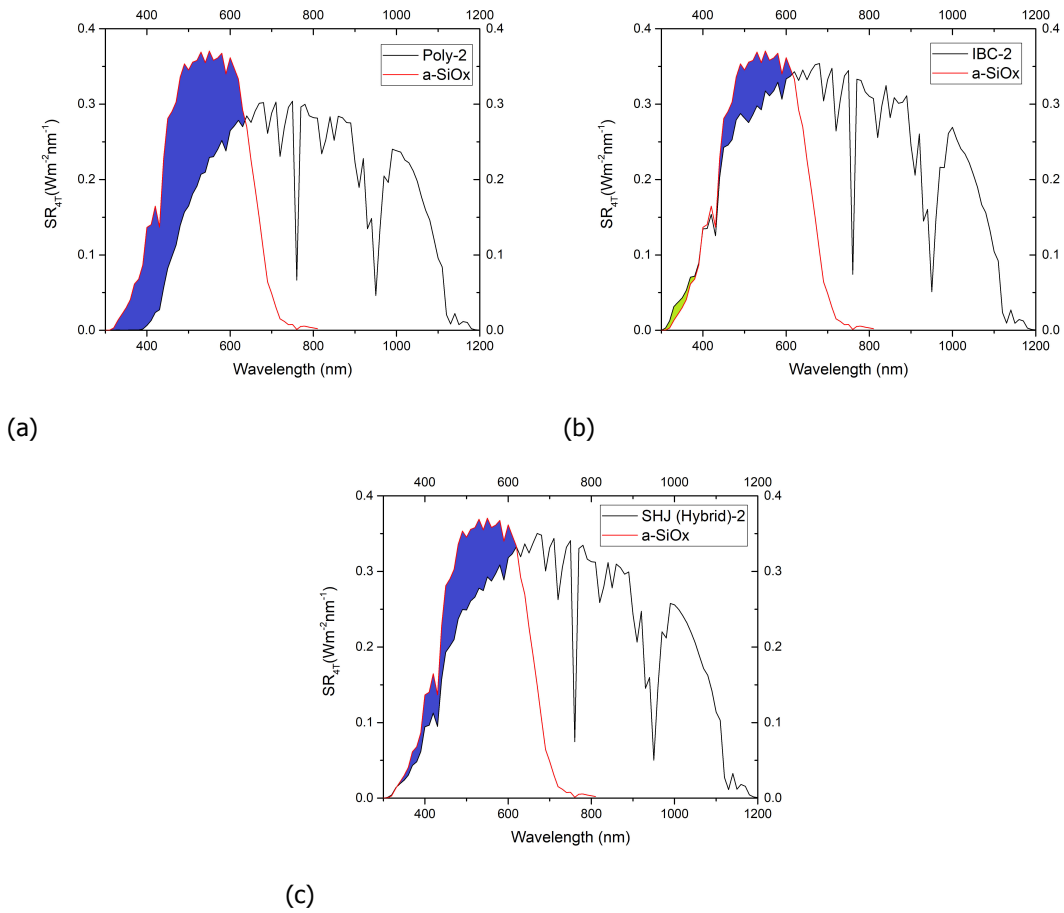

Figure 3.4: Spectral Response 4T (SR_{4T}) comparison with (a) the best poly-Si cell (Poly-2). (b) the best IBC cell (IBC-2). (c) the best SHJ (Hybrid) cell (SHJ (Hybrid)-2).

In the estimation of these values, certain assumptions are done, such as the performance of the bottom cell is not hampered due to the top cell in the red part of the spectrum. Also with a reduced current generation in the bottom cell, the open circuit voltage and fill factor will reduce. As the relation between the open circuit voltage and current is logarithmic, this decrease will not be too big. A good analysis of this is given in the work of Zhang et al. [25]. Although there is a decrease in performance of the bottom cell, but in the above calculations it is not taken into account. It is important to mention that no optical losses in the intermediate layers such as the glue and the glass are taken into account. Also, the top cell has a metallic back contact, but to show the maximum possible increment in the efficiency, it is worthwhile to use the best available cell. Hence the efficiencies calculated above can be called as maximum achievable efficiencies.

3.3. Conclusions

From the results of this chapter it is clear that four terminal approach of utilising a-SiO_x:H top cell and c-Si cell is promising. By using SR_{4T} parameter, which compares the power delivered by the cells at a specific wavelength, the efficiency gain that can achieved has been computed. Almost 1% to 4% gain can be achieved in the efficiency of the bottom cell by adding the a-SiO_x:H on top of it in a four terminal topology.

From the theoretical calculations performed in this chapter, some important points can be drawn for further work-

- The enhancement of the response of the top thin film cell in 300 to 600 nm spectral range, will lead to an increased gain in the efficiency. The higher the V_{oc} fill factor product of the top cell, higher the efficiency gain will be.

- In actual practice, the four terminal cell will have a transparent top cell. So a transparent conductive oxide for the top cell needs to be developed, such that its performance is comparable to the metal back contact.

A detailed analysis of the efficiency gain as well as optical simulations with four terminal configuration will be followed up in Chapter-7.

4

Fabrication of Hydrogenated Amorphous Silicon Oxide Cell

4.1. Introduction

This chapter will concentrate on hydrogenated amorphous silicon oxide based solar cell. The reason of using a-SiO_x:H as the top cell in comparison to conventional amorphous silicon cell has been explained in the earlier chapter.

From the results of the previous chapter, a gain of almost 4% can be obtained when an a-SiO_x:H top cell is used with a poly-Si cell in four terminal configuration. Gain between 1% and 3.7% can be realised by simply utilising four terminal topology. This is when the a-SiO_x:H cell developed in the work of Kim and Guijt is utilised as the top cell [29, 42].

A calculation of SR_{4T} can be done with a poly-Si bottom cell, with an increased V_{oc} of 1.04 V and fill factor of 0.73. The J_{sc} (12.3 mA/cm^2) of this hypothetical cell (a-SiO_x:H-2) is considered to be exactly similar to that of the 8.80% cell (a-SiO_x:H-1). In reality, the values chosen for V_{oc} and fill factor have been realised in the work of Kim et al [66]. The bottom cell is taken as the Poly-1 with parameters mentioned in the above chapter table. 3.2. The results are shown in the figure 4.1 and table 4.1. The yellow color indicates the improved response of the a-SiO_x:H-2 as compared to the a-SiO_x:H-1 cell

Table 4.1: Total efficiency that can be obtained in four terminal configuration with a-SiO_x:H-1(8.80%) and a-SiO_x:H-2 (hypothetical) top cell.

Top Cell	η_{Bottom}(%)	$\eta_{Increase}$(%)	η_{Total}(%)
a-SiO_x:H-1	14.22	3.94	18.16
a-SiO_x:H-2	14.22	4.40	18.62

Thus an increase of almost 6.58% in V_{oc} and fill factor product (0.714 vs 0.761) translates into an enhancement in the gain by 0.46% (3.94 vs 4.40%) in the four terminal configuration with a poly-Si cell. Other than the high V_{oc} and fill factor product, a good spectral response in 300 to 620 nm spectral range is also required to achieve higher efficiencies. Essentially, what this means is that we need a cell which has good response in 300 to 600 nm spectral range and has very low parasitic absorption.

Direct replication of the high efficiency cells developed in the work of Kim and Guijt was tried. But the attempts to replicate those cells failed. This can be attributed to the temporal fluctuations in the PECVD process. So, using the structure of the cells developed in their work new cells were developed and further optimisation was performed. Optimisation of thickness of the three main layers (p, i, n) to achieve high V_{oc} and fill factor product with a good spectral response is the task undertaken in this chapter. Even though there is another approach that could be used, that is by using high bandgap materials or nano crystalline layers, but in this optimisation, this approach is not utilised.

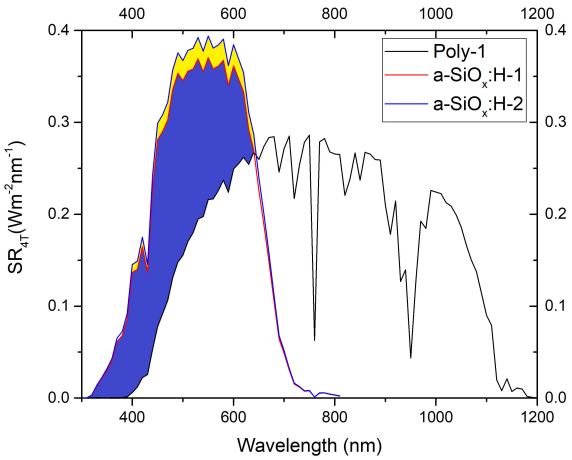

Figure 4.1: Spectral Response 4T (SR_{4T}) comparison with a-SiO_x:H-1 and a-SiO_x:H-2 top cells.

4.2. Optimised Cell Development

The first step in this optimisation is the development of a thickness series for the P doped layer, which is followed by the intrinsic layer and ultimately the n doped layer. In the end the optimised cell is developed and compared with reference cell as mentioned in chapter-2.

4.2.1. p Layer

Three samples of varying thickness- 4 nm, 5 nm, 6 nm with the reference cell of 7 nm are developed and compared. These thickness are chosen in accordance with simulations, which suggested a possible gain in blue green response. So it becomes important to see whether the other electrical properties are in good agreement with the reference cell. Specially the open circuit voltage, as it depends significantly on the p/i interface and the defects at this interface. The values obtained are plotted as shown in figure 4.2.

Looking at the figure of EQE in figure 4.3, it may appear that utilising the thinnest ie 4 nm p layer is the most obvious choice, but essentially we lose in the other two electrical parameters. As compared to the reference cell (7 nm), there is an almost 3.4% decrease in V_{oc} and a 6.5% decrease in fill factor although the short circuit current increases by about 2.1%, which is quite clear from the decreased efficiency, as shown in figure 4.2d. The reason for the improved current is the reduced parasitic absorption in the p layer, as with thin p layers more photons can be passed to the intrinsic layer. The decreased V_{oc} is due to the poor quality of the p layer. This also justifies the low fill factor. Another reason that could be a possibility is that thin p layer has a larger depleted region and hence the internal electric field is lower.

The next best available choice in terms of all the electrical properties is the 5 nm p layer, there is an increase of almost 3.1% in the J_{sc}, a 0.7% increase in V_{oc} and an almost similar fill factor. The 6 nm layer is also good option but when we see into the EQE plot there is no substantial improvement in the blue and green region of the spectrum. This justifies the choice of using the 5 nm layer.

4.2.2. i Layer

To optimise the intrinsic layer thickness, five samples were developed with thickness ranging from 100nm to 200nm (Reference cell) in steps of 25nm, these values were chosen in accordance with the results from simulation. Having thin intrinsic layers can reduce the parasitic absorption in the red and near infra red spectrum. Although, reducing it too much will start to decrease the total short circuit current, as now absorption will be reduced. Whereas, increasing the thickness will increase the current but open circuit voltage and fill factor will be reduced on account of larger number of recombination sites in the thick layer [80]. The decrease in V_{oc} on increasing the thickness of the absorber layer can also be attributed to lower diffusion length of the charge carriers. The charge carrier diffusion length decreases due to higher recombinations in a defect rich layer. The corresponding values are plotted in

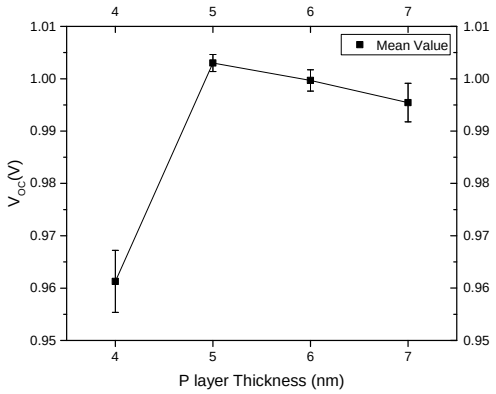

(a) Open Circuit Voltage vs p layer thickness.

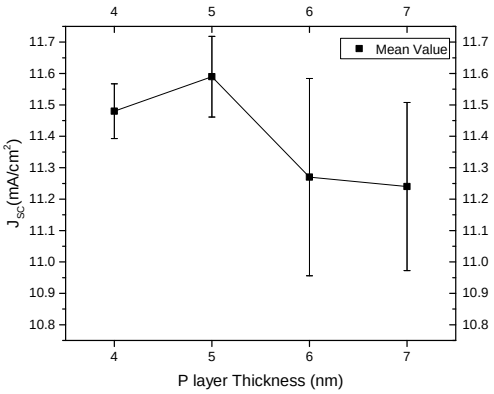

(b) Short Circuit Current vs p layer thickness.

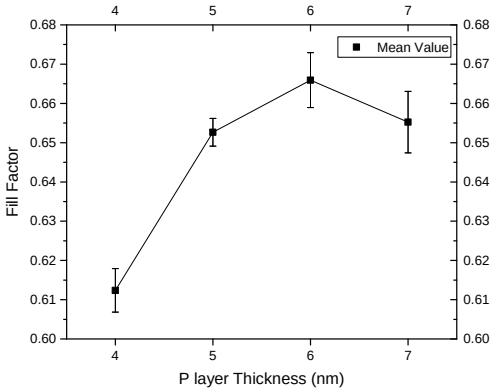

(c) Fill Factor vs p layer thickness.

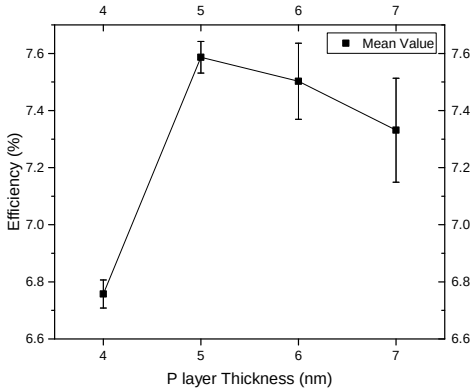

(d) Efficiency vs p layer thickness.

Figure 4.2: Electrical Parameter variations vs p layer thickness.

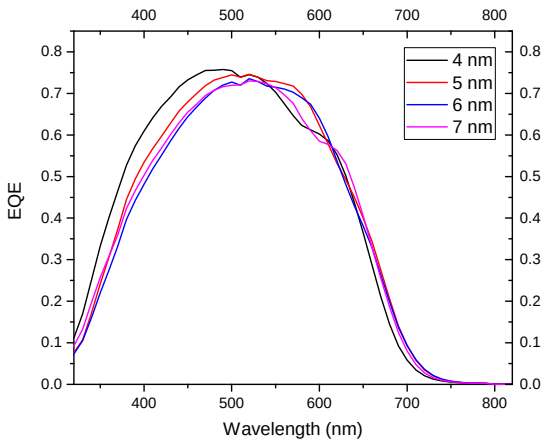

Figure 4.3: The EQE of the best cells in the p thickness series.

the figure 4.4. Only the best cell EQE is plotted in figure 4.5.

Looking at the V_{oc}, 125 nm looks to be the most promising, but the final efficiency is less than 7%. Thus to obtain best electrical properties- 175nm is chosen. The V_{oc} fill factor product is higher by almost 5% as compared to the 200 nm intrinsic layer (0.68 Vs 0.65). Although the J_{sc} is lower, the high

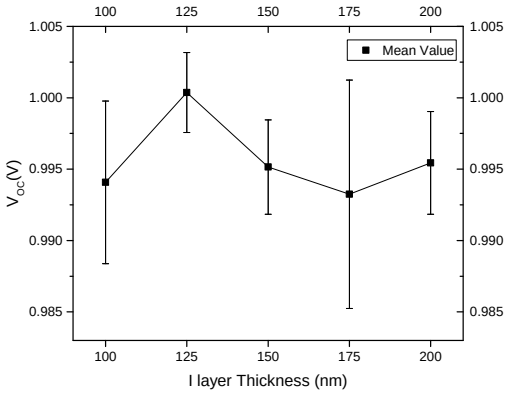

(a) Open Circuit Voltage vs i layer thickness.

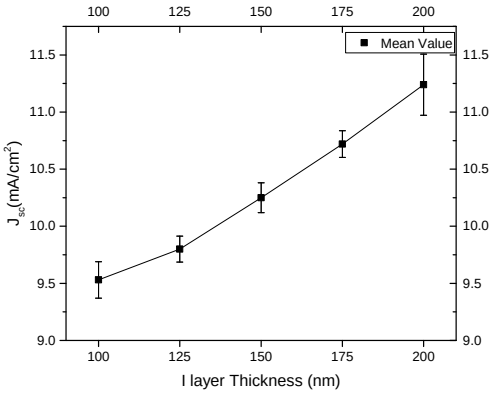

(b) Short Circuit Current vs i layer thickness.

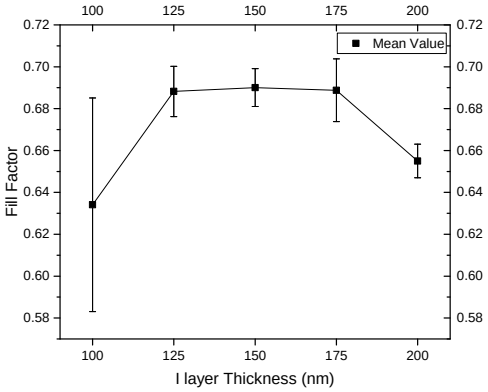

(c) Fill Factor vs i layer thickness.

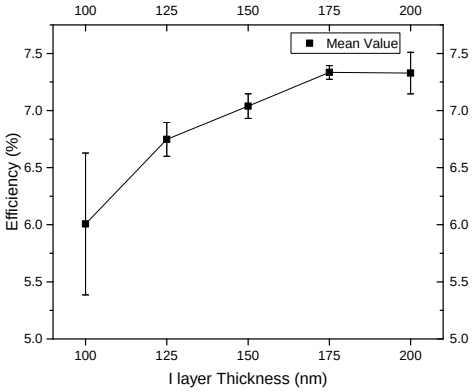

(d) Efficiency vs i layer thickness.

Figure 4.4: Electrical Parameter variations vs i layer thickness.

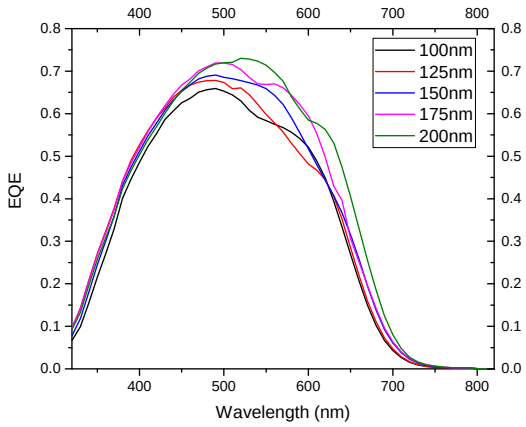

Figure 4.5: The EQE of the best cells in the i thickness series.

V_{oc} fill factor product more than compensates for it. Hence the efficiency of 175 nm cell is comparable to the reference cell. EQE plot in the figure 4.5 also support the use of 175 nm. In the red and near infra red region 175nm cell has almost similar performance as the reference cell. As there will not be any metal back contact in the final device. The target would be to have maximum transmittance to the bottom crystalline silicon cell, thus the poor response of 175 nm in the near infra red region will not

hamper the total efficiency.

4.2.3. n Layer

Taking into account the results from the simulation as well as from previous work done in PVMD group, the thickness of n layer was decreased from 100 nm to 25 nm in steps of 25 nm. The plots of the electrical parameters are shown in figure 4.6. From the figure 4.6b, it is clear that the short circuit current increases when the thickness is reduced, it is on account of reduced parasitic absorption in the n layer. From the EQE plot, it can be seen that the absorption is increased especially in 550 to 650 nm region when a thin layer is used. But in the case of the 75 nm layer, it is not true. Rather improvement is shown in the blue-green region, and no major improvement is seen by back reflection from the metal. As compared to the efficiency of the reference cell, there is an improvement in all the other cells made. The fill factor improves greatly due to reduced recombination in the thin layers, although comparing the 25 nm and 100 nm the fill factor is almost similar.

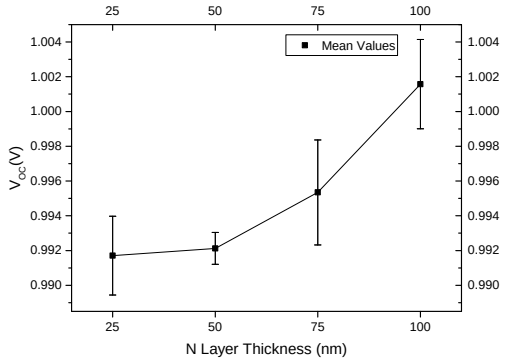

(a) Open Circuit Voltage vs n layer thickness.

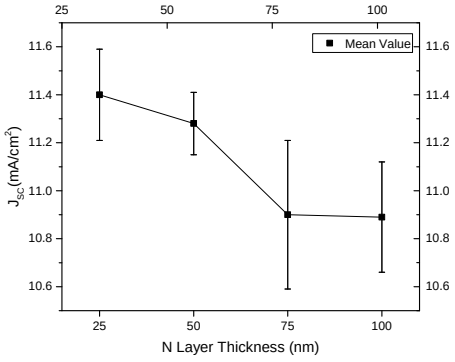

(b) Short Circuit Current vs n layer thickness.

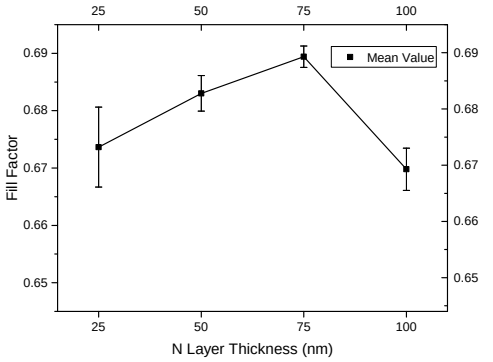

(c) Fill Factor vs n layer thickness.

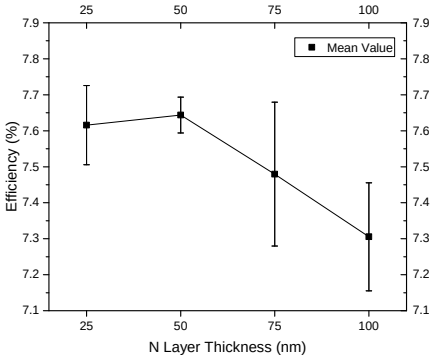

(d) Efficiency vs n layer thickness.

Figure 4.6: Electrical Parameter variations vs n layer thickness.

Due to the difference in the behaviour of the different n layers, it is not to clear which one is the best one. It would be logical to develop two cells with the structure as shown in table 4.2. All the layers except the ones mentioned in the table are kept same. It can be argued that 50 nm layer has a similar performance to the 25 nm layer in terms of V_{oc} and fill factor but the J_{sc} is almost 1.1% lower. Looking at only the efficiency plot 75 nm has lower efficiency than 25 and 50 nm. But the V_{oc} and fill factor product of this cell is almost 0.69. This is highest among all other cells in this series. This supports the development of the two cells.

The parameters in the table 4.3, clearly support the use of cell-B, as it has higher V_{oc} and fill factor product. The response is also slightly higher as shown in figure 4.8a. Even though in literature, it is said that the n layer does not influence the electrical properties strongly [81, 82], but this is not true in our case. A possible reason could be that in our case the thickness of the cell is within such a range

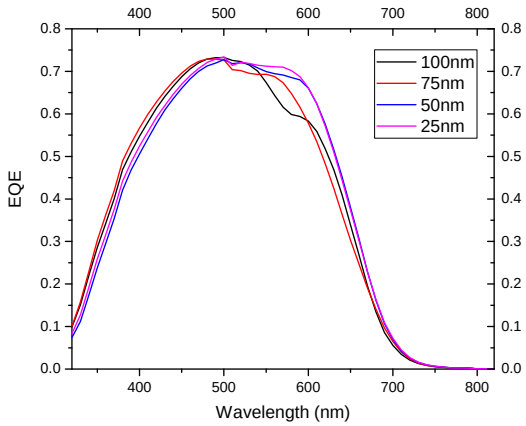

Figure 4.7: The EQE of the best cells in the n thickness series.

that the influence of the i/n interface starts to play a role. As shown in figure 4.8a, taking the reference cell developed for the n layer optimisation, there is quite a significant improvement in the blue green region of the spectrum.

Table 4.2: Thickness (in nm) of the layers used in the Cells

Cell	p-a-SiO_x:H	i-a-SiO_x:H	n-nc-SiO_x:H
Cell-A	5	175	75
Cell-B	5	175	25

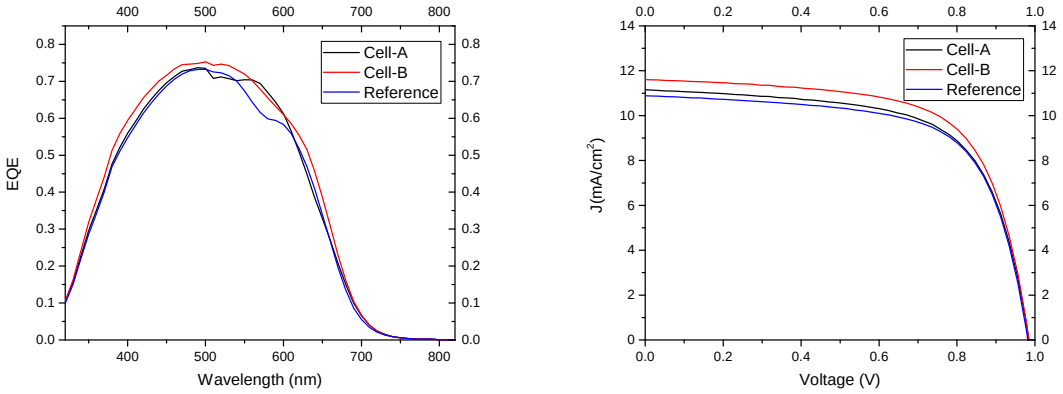

(a) The EQE of the best cells with the initial reference cell.

(b) The J-V curve for the cells, scaled with the EQE values.

Figure 4.8: Electrical Parameter for A, B and reference Cell.

Table 4.3: Electrical Parameters of the two cells compared with the reference cell.

Bottom cell	V_{oc}(V)	J_{sc}(mA/cm^2)	Fill Factor	Efficiency(%)
Cell-A	0.997±0.004	11.15±0.20	0.65±0.01	7.29±0.10
Cell-B	1.003±0.004	11.48±0.25	0.67±0.01	7.72±0.11
Ref	1.000±0.005	10.89±0.16	0.66±0.01	7.18±0.15

Also the illuminated current density (J) Vs voltage (V) curve shows the increased J_{sc} when the

structure of cell-B is used as shown in figure 4.8b. This curve is plotted for one of the cell, and the values of current density are scaled according to the value obtained from the EQE measurement. This is done because of two reasons. First, to remove any error due to the mismatch between the illuminated area. Second, to remove the errors due to mismatch between the spectrum of the light source in the J-V measurement and AM 1.5g spectrum at STC.

4.3. Conclusions

Optimisation of thickness of the three main layers (p, i, n) to achieve good V_{oc} and fill factor product with an appreciable J_{sc} has been accomplished. A cell with V_{oc} of 1.003 V, fill factor of 0.67 and J_{sc} of 11.48 mA/cm^2 with an efficiency of 7.72% has been developed. In further work, the structure of Cell-B will be used to develop the top cell for the four terminal cell.

5

Determination of Optimum Transparent Conductive Oxide Layer

5.1. Introduction

As mentioned in the earlier chapters, it is a prerequisite to have a transparent back contact for the top amorphous silicon oxide cell in our application. For that purpose, we need a transparent conductive oxide (TCO). A major research work has been done for the development and optiimsation of the front TCO in thin film cells, but the development of TCO layers as the back contact for the thin film cell is still lacking. For a conventional a-SiO_x cell the transparency of the rear TCO layer is not to important especially in the near IR range. However, for four terminal application, the transmittance in the red and near IR region is of paramount importance. The reason behind this is that the bottom cell is essentially absorbing photons in this spectral region. Another reason behind the optimisation of the back TCO is that in four terminal there is no back metal contact. Which means that the back TCO is responsible for lateral charge transport and current collection from the photoactive layers. Thus optimisation based on both optical and electrical properties of the TCO is required.

In this chapter, we will delve into the three most commonly employed TCO's namely indium tin oxide (ITO), hydrogenated-indium oxide (IO:H) and aluminium doped zinc oxide (AZO) as the back contact for the top cell. Towards the end of this chapter the development of double layer TCO's will also be discussed. The final goal of this chapter is to develop bifacial thin film cell, which is optimal for four terminal application.

5.2. Electrical and Optical Properties of the TCO layers

Three samples each of ITO, IO:H and AZO are with thickness of 50, 100 and 200 nm were developed. The electrical properties of these materials were characterised using Hall measurements, four point probe method. The sheet resistance was calculated by using equation 2.6. Mathematical relations can be seen in chapter-2 section 2.2.3. The electrical properties:- sheet resistance ($(\Omega/\square)$), resistivity (ρ) (Ω cm)), bulk concentration(N_c) (cm^{-3}) and mobility (μ) ($cm^2/V.s$) are presented in table 5.1.

Some interesting observations can be made from the table 5.1. Firstly, increasing the thickness of the ITO layer leads to a reduction of the sheet resistance. The mobility decreases when the thickness is increased. In literature also such behaviour has been observed, which has been attributed to the discrepancies in the initial growth period of the ITO film [83]. This may also be due to increased impurity scattering in the bulk of the material [54]. For IO:H layers high mobility is observed, but the resistivity and sheet resistance are on the high side. One thing that could have lead to this is the presence of an insulating oxide layer on top of the IO:H layer [59]. Another observation is the low carrier concentration for the IO:H layers. According to Drude theory, a low carrier concentration and a high mobility lead to a low absorption coefficient in IO:H (sub band gap absorption). For, AZO samples by increasing the thickness sheet resistance is reduced. This reduction can be explained from the increase in carrier concentration and carrier mobility [84, 85]. Another reason can be the increased crystallinity and grain size of the films, when thickness is increased [49]. This also satisfies the inverse

Table 5.1: Electrical parameters of the as-deposited TCO layers.

Material	Thickness (nm)	Sheet Resistance ($\Omega/\square$)	ρ ($10^{-3}\Omega$ cm)	μ (cm^2/V.s)	N$_c$ (10^{19}cm^{-3})
ITO	50	67.60	0.338	21.83	84.60
	100	42.44	0.424	15.16	98.00
	200	38.20	0.764	10.40	78.50
IO:H	50	974	4.87	58.00	2.25
	100	514	5.14	76.00	2.56
	200	231	4.62	48.40	2.80
AZO	50	1794.0	8.97	8.65	8.04
	100	975.0	9.75	7.17	8.93
	200	194.5	3.89	10.34	16.0

relation between thickness and sheet resistance. Only a slight increase in the resistivity is observed, it could be due to some error in measurement equipments. With four point probe, the measurement for 100 nm AZO layer was verified and it gave a value of 8.29 X $10^{-3}(\Omega cm)$. The sheet resistance was 828.51 $(\Omega/\square)$. Thus, there is variation in the values between Hall Measurement and four point probe. From literature, going to higher AZO thickness can even lead to a decrease in the mobility. This can be attributed to the change in the electronic state of the crystal due to carrier-carrier interaction (lattice scattering) and carrier impurity interaction (impurity scattering). These effects are collectively called many-body effects [86, 87]. In this work we will limit ourselves to 200 nm as the higher limit. Also the optical parameters of the layers are influenced when the thickness is increased. The standard deviations (error margins) for the above values are shown in appendix B.3.

The absorptance of the six different TCO layers are mentioned in the below table 5.2. This parameter is presented as an average value in percentage in the 300 to 1200 nm and 600 to 1200 nm range spectrum. The average is calculated by utilisisng the mathematical relation between transmittance (T), reflectance (R) and absorptance (A) (100 = T+R+A) in percentage at each wavelength. From this value absorptance is calculated at each wavelength and then the average is done. To correctly determine the absorptance in the TCO layer the correction for the Corning eagle XG glass substrate is also taken into account. The procedure to do this is explained in appendix A.1.2. This correction is done after subtracting the sum of transmittance and reflectance from 100. The transmittance and reflectance values are experimentally determined from spectrophotometer and the corresponding curves are shown in figure 5.1.

Table 5.2: Absorptance of the as-deposited TCO layers.

Material	Thickness (nm)	Absorptance (300-1200 nm) (%)	Absorptance (600-1200 nm) (%)
ITO	50	5.66	3.09
	100	6.70	3.69
	200	9.81	6.80
IO:H	50	3.20	0.85
	100	4.24	0.88
	200	6.79	1.82
AZO	50	1.34	0.29
	100	2.81	0.56
	200	4.32	1.74

In the table 5.2, the absorptance in the spectrum range of 600 to 1200 nm is also shown. This is done because the TCO will form the back contact of the top cell. Hence, the TCO will only receive photons with wavelength between 600-1200 nm approximately. This makes the analysis of absorptance more meaningful. The most important observation from the above results is that with increasing thickness the absorption in the material increases [84]. The curve for reflectance in figure 5.1, shows interference patterns which are the reason behind the wavy nature in the figures.

Even though we can use thicker layers but as clear from the optical measurements shown in table 5.2 and figure 5.1, using thicker layers will lead to higher absorption. This is undesirable for our

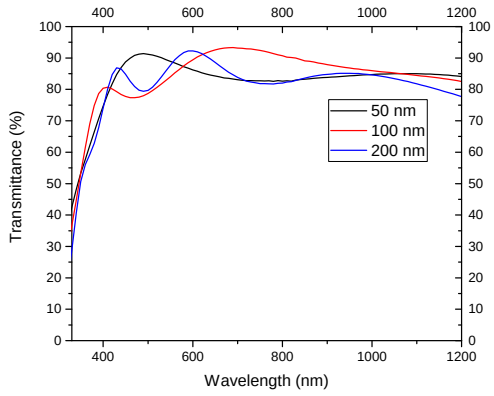

(a) Transmittance curve for the ITO layers.

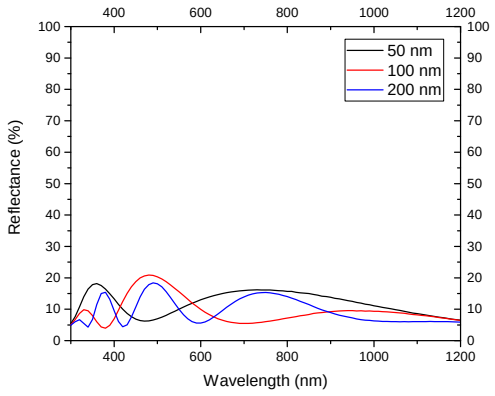

(b) Reflectance curve for the ITO layers

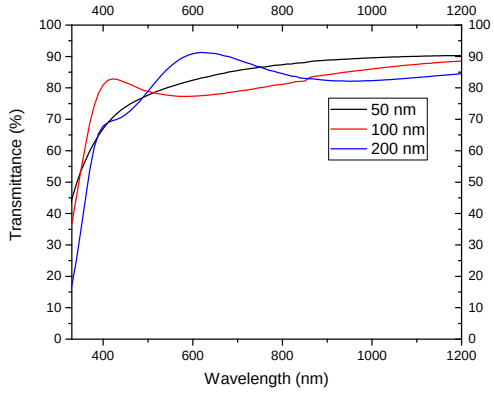

(c) Transmittance curve for the IO:H layers.

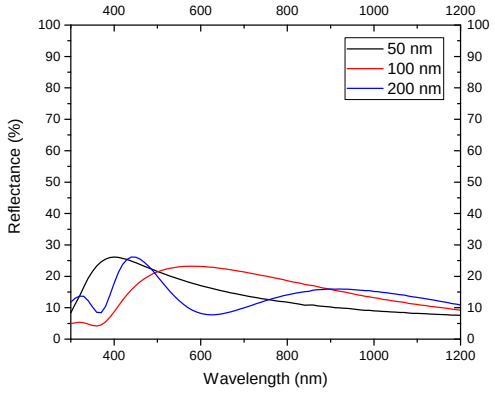

(d) Reflectance curve for the IO:H layers

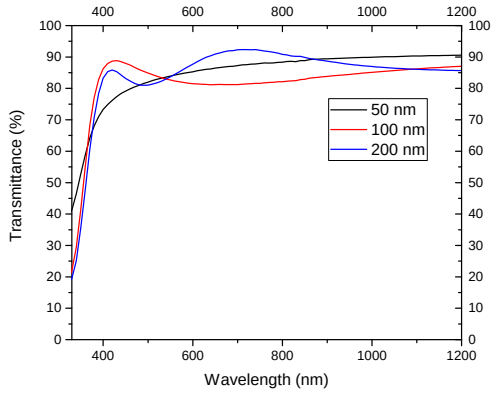

(e) Transmittance curve for the AZO layers.

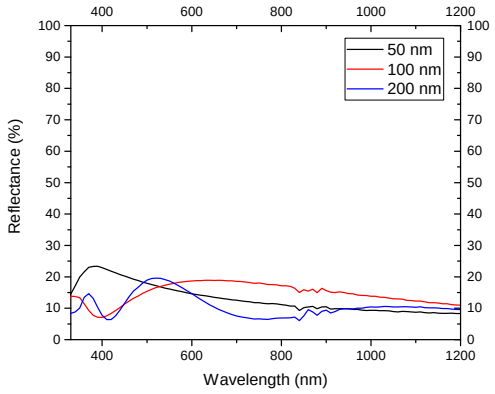

(f) Reflectance curve for the AZO layers

Figure 5.1: The plots of transmittance and reflectance for the as deposited single layer of TCO.

application. Also, higher transmission in 600 to 1200 nm is required for the proper functioning of the bottom c-Si cell.

5.3. Performance As Back Electrode

From the optical and electrical properties of the TCO, it can be seen that going for a lower sheet resistance will require thick layers, which will in turn reduce transmission to the bottom cell. This can

be related to increased absorption [49]. Out of the nine possible layers, seven layers are chosen to be tested as the back contact for the thin film in accordance with the electrical and optical measurement in the above section. These are- 50 nm ITO, 100 nm ITO, 100 nm AZO, 200 nm AZO , 50 nm IO:H, 100 nm IO:H and 200 nm IO:H layers.

The reason for not choosing 200 nm ITO layer is because of its high absorptance in the red and near IR region, which is detrimental in our application. The IO:H layers are chosen in accordance with their high mobility. The two AZO layers are chosen in accordance with the low absorptance values even though they have high sheet resistance values as compared to ITO and IO:H. The 50 nm AZO layer has very high sheet resistance, so it is not used. The reason for using AZO is also motivated from literature [88, 89]. There is a gain in terms of V_{oc} and J_{sc} when an AZO layer is used with n-type silicon layer according to literature.

Firstly, a-SiO_x:H based cells with the above mentioned TCO layers as the back contact are developed by using the parameters and the structure specified in chapter-4 and 2. Then electrical parameters of these cells are measured and compared. In this comparison, an average of five best performing cells with an area of 25 mm^2 are taken. The second step used, is the determination of the transmittance, reflectance and absorptance of the working cells.

Although these optical parameters were determined earlier. But the optical system, in that case, is not similar to the one utilised in our four terminal device (transparent top cell). In the earlier section, the optical properties were determined when the TCO was deposited on the glass substrate. In four terminal application the optical system is quite complex because it involves various a-SiO_x:H layers. So, the optical parameters need to be remeasured in accordance with the different refractive index materials in front of the back TCO. These two steps form the strategy by which the best TCO layer for the thin film cell in our application is determined.

There was a problem encountered when the cells were developed with IO:H. All the cells were found to be shunted. One reason for this can be attributed to the formation of an interfacial insulating layer at the TCO-Silver (metal) interface. In literature, this has been reported to cause a low fill factor [59]. This usually occurs when the cells are annealed. To avoid this in the second rerun, no cells were annealed but the results did not improve. Only one cell out all the cells made was working. The performance of the lone cell was very poor as compared to the cells made with other TCO back contacts. The V_{oc} and fill factor of the cell were- 0.851 V and 0.351 respectively. With a single working cell that to with a low V_{oc} fill factor product it was not viable to continue on making more IO:H back contact cells. This opens an interesting possibility to develop IO:H based bifacial a-SiO_x:H cells. This could be a good future project.

The electrical parameters of the cells are mentioned in the table 5.3.

Table 5.3: Electrical Parameters of the cells with different back TCO layers.

Material	Thickness (nm)	V_{oc}(V)	J_{sc}(mA/cm^2)	Fill Factor	Efficiency(%)
ITO	50	0.94±0.018	10.50±0.32	0.58±0.09	5.72±0.04
	100	0.95±0.002	10.75±0.53	0.65±0.01	6.64±0.08
AZO	100	0.97±0.002	10.31±0.80	0.66±0.02	6.60±0.15
	200	0.97±0.004	9.45±0.78	0.59±0.01	5.41±0.30

It can be deduced that highest efficiencies cell out of the four is the one with 100 nm ITO back contact, although the efficiency of the 100 nm AZO is nearly equal to it (6.64% Vs 6.60%). The EQE and J-V for a cell of 100 nm ITO and 100 nm AZO back contact are shown in appendix B.3. The J_{sc} in the case of cell with ITO back contact is higher as compared to that made of AZO, this could be because of the low resistivity of the ITO layer. The low resistivity of ITO layer leads to a low series resistance for the cell with ITO back contact (experimental value from J-V measurement ≈6.40 Ωcm^2) as compared to the value for cell with AZO (≈7.20 Ωcm^2). The impact of series resistance on the J_{sc} for thin film cells still needs to be verified with more experiments. Thus the advantage of using AZO/n type contact as suggested in literature (specially with nc-Si) over the use of ITO/n contact is negated by the high resistivity of the AZO film [88, 89]. The impact of series resistance is not too profound on the fill factor (0.65 vs 0.66). Even though cells with ITO have higher J_{sc}, they have lower V_{oc}. The reason for this could be higher recombination at the ITO/n interface due to higher defect density in ITO layer. Another reason mentioned in literature is the degradation of the n layer due to diffusion

of indium from the ITO layer [86]. As the ITO layer is deposited using Indium Oxide and Tin Oxide (90%/10% by weight) target. This impurity acts as an acceptor impurity. This effect is lower when AZO layers are used which is due to comparatively less Aluminium impurity atoms in AZO (ZnO/Al_2O_3 (98%/2% by weight) target is used for AZO deposition). It was expected that the values for 200 nm AZO were the best out of the lot, but the low fill factor in this case pegs the efficiency to less than 6 %. A reason could be the poor quality of the 200 nm AZO layer. Till now in literature, no values regarding the electrical parameters have been reported for bifacial a-SiO_x:H based solar cells. Hence, the values reported in table 5.3 are the first values of electrical parameters for bifacial a-SiO_x:H based solar cells. There is a drop in V_{oc} and J_{sc} as compared to the reference cells developed in the earlier chapter. The reason for this can be attributed to the band offsets when TCO are used as the contacts instead of metal contacts [90]. Next step in deciding the best back TCO, is to compare the optical properties of the cell with 100 nm ITO and 100 nm AZO. The plots of the optical properties are presented in the figure 5.2. From the plots of transmittance in figure 5.2a, the AZO layer is the best as it has higher transmittance in the red and near-IR region. The pattern of the curve in the IR region could be due to interference.

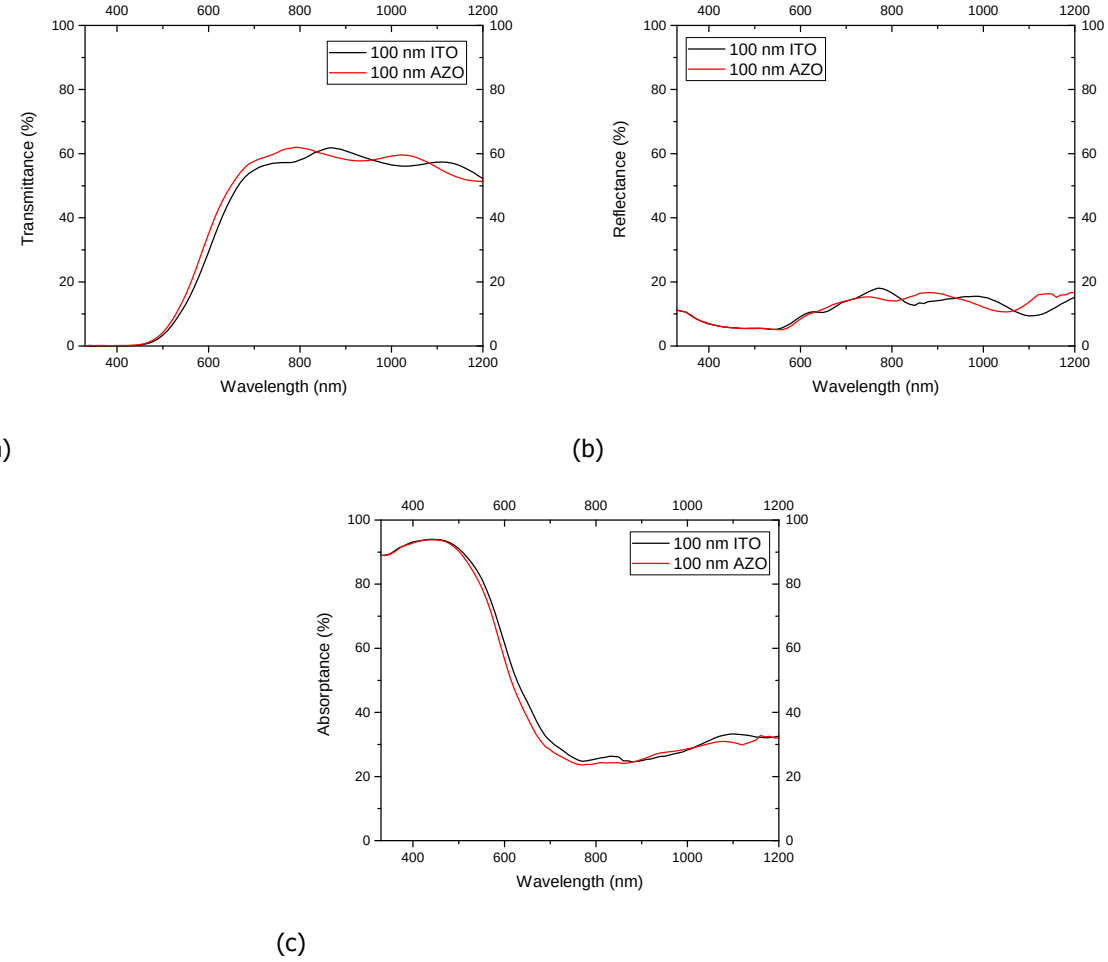

Figure 5.2: Optical parameter- a) Transmittance b) Reflectance and c) Absorptance of the cell with 100 nm ITO and 100 nm AZO back contacts.

The reflectance curve also contains some interference patterns. this is the reason behind the wavy nature of the reflectance curve in the near IR region. From the absorptance curve there is parasitic absorption in the top cell in the near IR region. The high absorptance in near UV and visible region is because the top cell is developed to absorb in that region. The absorptance curve is nearly identical for both the cells. It is also important to mention that no correction factor was applied to the absorptance of the cell as the optical system used in these measurements is the same as the one which is utilised

in this work. Thus it means that more optimisation is required to achieve ideal TCO for four terminal devices. The reflection is also high, this means that the optical system in the thin film cell needs to be optimised by changing the refractive index of the layers. This can be done by changing the deposition parameters of the layers. One more thing that was observed was that the cell made with ITO layers had more probability of having shunts. Out of 24 cells deposited on the 10 X 2.5 cm^2 of Asahi glass only 8 had a decent performance. The number for AZO layer was 18 out of 24 cells. This means that there is a possibilty that the deposition of TCO is not homogeneous. This may be also behind the large standard deviation in the electrical parameters of the cells. A more controlled and uniform deposition process needs to be developed to get more working cells, although in the next chapter where some four terminal devices are developed, 100 nm AZO will be used. One of the reason is that the AZO deposition is more uniform as compared to the one of ITO. The V_{oc} fill factor product is higher for cell with AZO back contact as compared to the ITO (0.64 Vs 0.62). This is very important in deciding the optimum top cell as explained in chapter-3.

5.4. Double Layer

Observing the electrical and optical results mentioned in the previous section some conclusions about the ITO and AZO layers can be deduced. The ITO layers have lower sheet resistance and resistivity. The AZO layers have a superior optical transmission. Also with AZO/n interface in a cell, there are advantages associated to the V_{oc}. With reduced contact energy barrier at the AZO/n as compared to ITO/n contact, higher V_{oc} can be obtained [91]. This is because of lower workfunction of AZO material. This can also be seen in the measured values in table 5.3. Utilising a double layer TCO is a good solution in improving the performance of the cells [89, 90, 92, 93]. The ITO provides high electrical conductivity whereas the AZO layer provides high optical transmission. In the multilayer structure of AZO and ITO, the electrical properties are dominated by ITO and the optical properties are influenced by AZO [88, 89, 93]. It is quite interseting that there are single values for the mobility and resistivity for the double layer stacks. According to Matthiessen's rule, the mobilty is determined from the parallel combination of the mobilities associated to various scattering mechanisms. Hence, in case of double layers the mobilities are determined from scattering mechanisms in both the layers. To develop double layer TCO's, AZO with thickness of 50 nm, 100 nm and ITO with thickness of 50 nm, 100 nm are utilised. A number of combinations of double layers could be tried but we have limited our self to double layers having a maximum thickness of 200 nm (100 + 100 nm). Four double layers are formed. Electrical parameters of the as-deposited TCO double layers are mentioned in table 5.4. In the table the thickness of the layer of AZO and ITO are separately written.

Table 5.4: Electrical parameters of the double layer TCO.

AZO (nm)	ITO (nm)	Sheet Resistance ($\Omega/\square$)	Resistivity ($10^{-3}\Omega$cm)	Mobility (cm^2/V.s)
50	50	493.00	4.93	7.66
50	100	310.00	4.66	6.45
100	50	386.67	5.80	8.34
100	100	219.50	4.39	11.50

It must be noted that four point probe was not used in these electrical measurements. This is because variable and contradictory readings were obtained for the same sample. In four point probe method, mechanical force is applied to the layer by the four probes. The measurements become inaccurate and variable due to the damage caused to the ITO layer by this force. To get the electrical parameters Hall measurements are used alone.

Comparing the values in table 5.4 and table 5.1. The value of sheet resistance of all the double layers are less than the one's for the AZO single layer of 100 and 50 nm. For example, for 50 nm single layer of AZO the value is 1794.0 ($\Omega/\square$) while for the double layer of 50 nm AZO and 50 nm ITO it is 493.0 ($\Omega/\square$). The resistivity value is also reduced by application of ITO layer on top of AZO layer For, 50 nm single layer AZO it is 8.97 X $10^{-3}\Omega$ cm, while for the double layer of 50 nm AZO and 50 nm ITO it is 4.93 X $10^{-3}\Omega$ cm. Using the notations in table 5.5 the plots of the electrical parameters Vs the type of layers, are shown in figure 5.3. It can be seen from the figure 5.3, for single layers of ITO (for example, 50 nm ITO has sheet resistance of 67.60) still have lowest sheet resistance and resistivity. These layers have the highest mobility values. So two limits can be defined for the electrical properties

of the double layers. One limit is defined by the electrical properties of the single AZO layer and the other by the ITO single layer electrical properties.

Table 5.5: Notations for the double and single layers of AZO and ITO.

Name of the layer	AZO (nm)	ITO (nm)
A	0	50
B	0	100
C	50	50
D	50	100
E	100	50
F	100	100
G	50	0
H	100	0

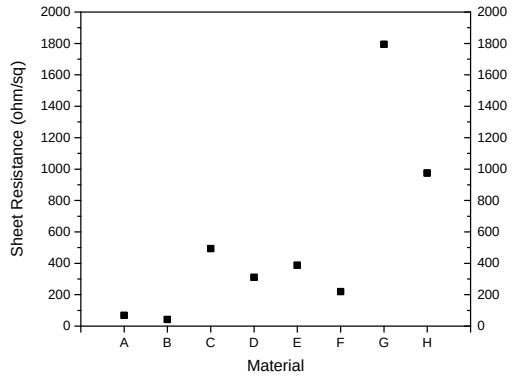

(a) Sheet resistance Vs Material

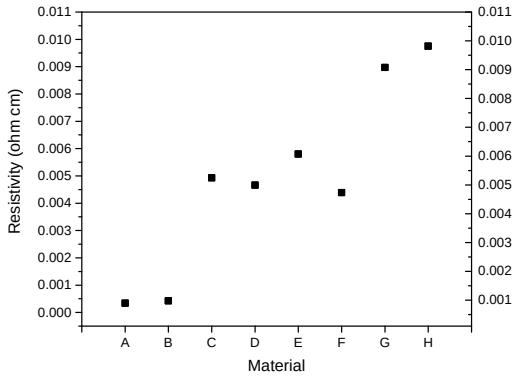

(b) Resistivity Vs Material

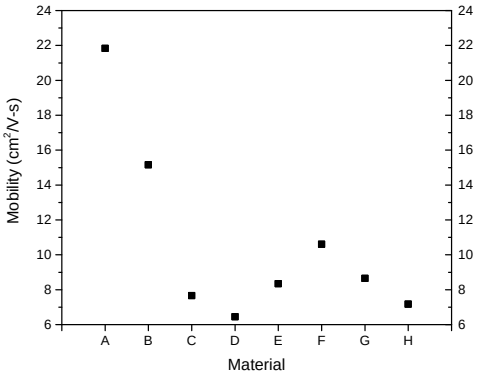

(c) Mobility Vs Material

Figure 5.3: The plots of electrical parameters comparison between double layers and single layers.

As clear from the plots of sheet resistance and resistivity, the values for double layers lie between those of AZO and ITO. Although the relationship is not linear, it is still possible to develop double layers with values between the single layers. Only in the trend of mobility there is a variation. The reason for this is not too clear.

The optical parameters of the four double layers are presented in the figure 5.4. Analysing, the curves it can be seen that the transmittance value has decreased as compared to that for a single AZO layer. In literature, average values of transmittance are compared and then inferences are made

[89, 90, 93]. But, taking average in a specific range of spectrum is not a true estimator for increase or decrease in transmittance. As, the range of spectrum can be taken such as to support the conclusion one wants to draw. This is not done in this work. Only average absorptance is used, so as to draw conclusions as, the TCO layer needs to have low absorptance in 600 to 1200 nm range. The average absorptance (%) of the four double layers are presented in the table 5.6.

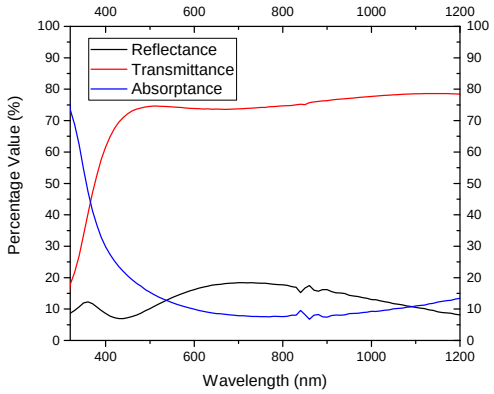

(a) Optical parameters of 50 nm AZO and 50 nm ITO.

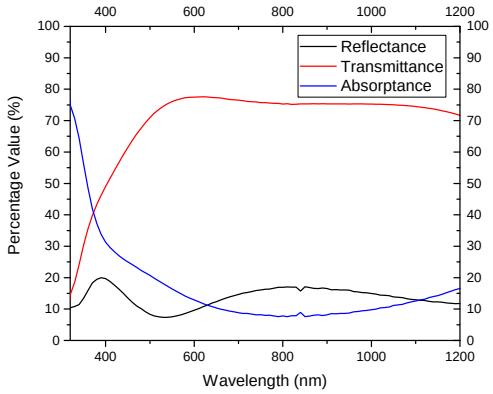

(b) Optical parameters of 50 nm AZO and 100 nm ITO.

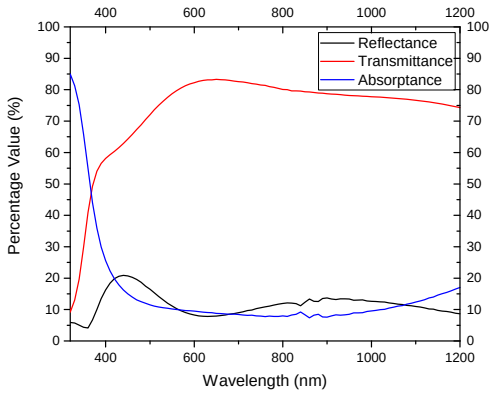

(c) Optical parameters of 100 nm AZO and 50 nm ITO.

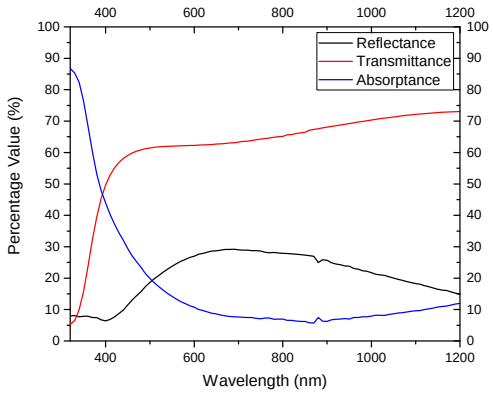

(d) Optical parameters of 100 nm AZO and 100 nm ITO.

Figure 5.4: The plots of optical parameters of the double layers of AZO and ITO.

Table 5.6: Optical parameters of the double layer TCO.

AZO (nm)	ITO (nm)	Absorptance (300-1200 nm) (%)	Absorptance (600-1200 nm) (%)
50	50	14.17	8.88
50	100	15.94	9.95
100	50	14.26	9.58
100	100	16.37	7.90

The absorptance (%) of the four double layers are presented in the table 5.6. There is a substantial absorptance in the double layers. This is because when the two samples are added there is almost double the absorption as compared to the single layer. It is quite interesting that the electrical properties are not affected by the deposition of ITO on AZO. There are two reasons why double layer TCO cells are not utilised in this work. Firstly, the deposition process of the two TCO are in separate machines and requires different masks. Though, special masks were used but still no working cell was obtained. Other reason is the optical shortcomings (high absorptance) in the double layer of ITO/AZO double layer TCO. Still, this approach of double layers can be used in future devices.

In this work, AZO depositions at higher temperature (at 325 and 350 ° Celsius, heater temperature) were tried, which gave lower sheet resistance and resistivity. This is due to increased carrier concentration and mobility at high temperature deposition [94]. Also the transmission over the spectrum was increased, specially in the blue region. The increased transmittance can be attributed to Burstein–Moss effect hypothesis, which predicts that the Fermi level inside the conduction band moves upward with increasing carrier concentration due to the filling of the conduction band by the increase of carriers [86, 95]. Hence the optical bandgap increases. This leads to higher transmission in blue region. Although, this is interesting for development of TCO, but when these TCO's were applied to thin film cell as the back transparent contact there was shunting observed. No working cells were obtained when higher substrate temperature was used for TCO deposition. This phenomenon is called as overfirring of the contacts. Thus the parameters at low temperature (300° C) for AZO were utilised for the development of the TCO layers. A 400 nm layer of AZO was also tried but there was a drop in V_{oc} and fill factor when this was done. A V_{oc} of 0.95 V, fill factor of 0.59 and 9.69 mA/cm^2 J_{sc} was obtained. Still, more thickness series could be tried in future work.

5.5. Conclusions

The selection of the suitable TCO layer out the 9 layers has been carried out in this chapter. According to the electrical and optical parameters 100 nm AZO layer has been found suitable for four terminal application. In the end, a bifacial a-SiO_x:H based thin film cell utilising 100 nm of AZO layer as the back TCO has been developed. This is a first of its kind bifacial cell of a-SiO_x:H. The first reported efficiency of this cell is 6.60%. This cell will be utilised in the final device fabrication for the four terminal solar cell in the next chapter.

6

Development and Characterisation of the Four Terminal Solar Cell

6.1. Introduction

In the previous two chapters, an optimised transparent a-SiO_x:H cell structure with a 100 nm AZO back contact has been developed. Now it becomes imperative to integrate this optimised top cell with the c-Si bottom cell. This chapter contains the fabrication details regarding the development of the four terminal cell and its characterisation. The first section contains the details for the development of the large area top a-SiO_x:H cells. Next section specifies the use of conformal coating in the development of the four terminal device. The last section contains the final steps in the development process and the results pertaining to the performance of the final devices, utilising some of the c-Si cells developed in our group, as the bottom cell. After the development of the four terminal cell, characterisation of its electrical parameters will be carried out. This will be followed by analysis of the obtained parameters. These are the main goals of this chapter.

6.2. Large area top thin film cell

To develop the four terminal cells we require a large area top cell, as the bottom cells used in this work has a size of 3 by 3 cm^2. The previous thin film cells had an area of 25 mm^2. Hence, to develop the four terminal cell, the top cell should have dimensions similar to the bottom cell. The following sequential steps were followed to achieve a large area cell:

- Asahi glass was cut into 5 cm by 4 cm and cleaned according to the steps mentioned in chapter-2 subsection 2.3.1. The size was chosen in accordance with the size of the sample holders.
- Using the mask shown in figure 6.1a, front metal contact was put on the conductive side of the Asahi glass.
- After the front contact metal deposition, the required a-SiO_x:H films were deposited by PECVD so as to have the thin film cell. The dimensions of the thin film cell are 4 cm by 3.5 cm. This is done so that the front metal bar is not fully covered by the cell.
- The back TCO was deposited in Amigo (RF magnetron Sputtering-DPC 6), followed by deposition of the back metal contact using the mask shown in figure 6.1b. The metal mask is covered with an aluminium foil such that well defined back contact could be deposited.

Following the above steps, the large area thin film top cells were developed. One big recurring problem of shunting was observed while developing these cells. Shunting means that there were shunt paths in the cells because of which V_{oc} becomes zero. All the large area cells were shunted. One reason could be the inhomogeneous deposition in Amigo. Another reason could be that when the TCO was deposited there might be overfiring in some part of the cell and hence leading to shunts.

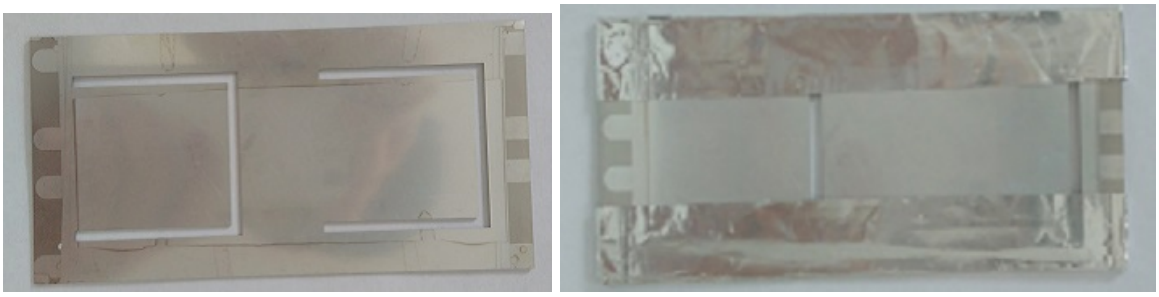

(a) (b)

Figure 6.1: Actual image of the metal mask used for a) Front metal contact b) Back metal contact for the top a-SiO_x:H cell.

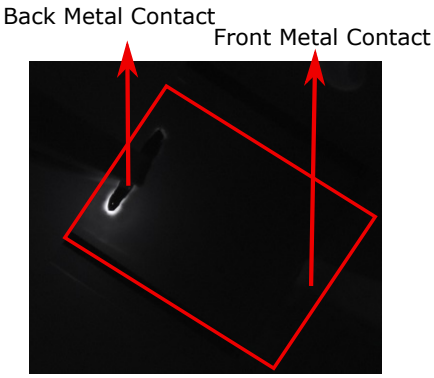

Figure 6.2: The EL image of a large top cell with 100 nm AZO as the back contact. The applied voltage is 2.2 V and current is 0.5 A.

To correctly observe the reason for this shunting problem, Electroluminescence (EL) test at various voltages were performed to see where the majority of the shunts lie. Going at a very high voltage damages the cell so careful monitoring of voltage is required in EL tests. In the EL image in figure 6.2, there is some glow near the metal contacts but in the centre and the edges it is dark. The dark areas in the EL images show a non working cell. This means that shunts are present all over the cell. These shunts could have developed when the a-SiO_x:H layers are deposited or when the TCO is deposited. To assess the actual reason, EL images were taken of a 9 cm^2 cell with a metal back contact as shown in figure 6.3 no bright spots in the centre area of the cell are visible. This means that not only the TCO deposition causes the shunts, but the process of deposition of the layers of the cell is also responsible for the shunting problem. This supports the reason that PECVD process in Amigo leads to shunts. When looking at the EL images of a working small area (25 mm^2) cell, with a 100 nm AZO back contact as shown in figure 6.4. The bright glow shows that in the case of small area the discrepancy in deposition is not present. In the image of small cell only the back contact is shown. The small cells are deposited on a 10 cm by 2.5 cm strip, where the front contact lies on the edge of the strip. One important thing to mention is that on an Asahi sample of 10 cm by 2.5 cm about 24 cells are made and only 18 of the cells worked properly on an average. This amounts to a failure rate of 25%. This implies that when we scale the area of the cells the chances of having a shunt is increased. Even with small shunts in a large area cell, the chances of obtaining a working cell is reduced.

To remove this problem various methods were applied, such as plasma etch using CF_4 and Oxygen. This was done to etch some of the n layer present at the edges of the cell, which was not covered with the TCO. As there are high chances of shunts at the edges. This is clear from the dark areas in the EL images of the large area cells. This approach was not successful. Another approach used, was by applying a reverse bias voltage sweep across the cell so as to oxidise some of the shunt paths [96]. By applying a voltage across the cell an increase in shunt resistance is observed, which means that shunts present in the material are removed. But this approach was not successful on the large area cells. Finally, it was decided to use the electrical parameters of the 0.25 cm^2 cells made with 100

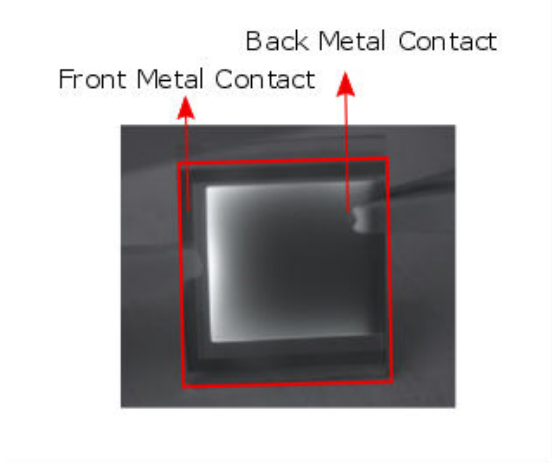

Figure 6.3: The EL image of a 9 cm^2 cell with Silver as the back contact. The applied voltage is 2 V and current is 0.6 A.

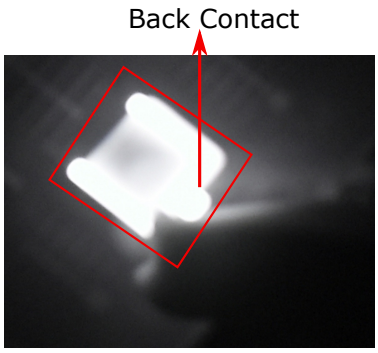

Figure 6.4: The EL image of a 0.25 cm^2 cell with 100 nm AZO as the back contact. The applied voltage is 2 V and current is 0.5 A.

nm of AZO as the back contact. The parameters mentioned in the table 5.3 are used as the electrical parameters for the top cell.

6.3. Conformal coating

The actual fabrication of the four terminal device requires use of an adhesive between the two cells. In this work, an acrylic based conformal coating composed of ethyl acetate and butyl acetate solvents, commercially sold as PLASTIK 70, was used. It is a colourless, transparent, insulating and protective coating based on acrylic resins [97]. This was chosen because of the rather simple and easy process of applying it, as well as the electrical insulating and very high transmission as shown in figure 6.5.

Taking the absorptance of the Corning eagle XG glass substrate from appendix A.1.2, the average absorptance in 300 to 1200 nm spectral range of the conformal coating was calculated. The absorptance of the conformal coating is 0.63%. With the low absorptance, this coating is suitable for our application. Considering the glass substrate as perfectly transparent, the absorption coefficient (α) of the coating can be derived by using basic optics and the measured transmittance and reflectance values [98]. The formula of the absorption coefficient (α) is shown in appendix A.1.3, equation A.2. A thickness of 1 um is considered in the calculation. The solution from this calculation did not yield meaningful result. This is because the derived formula has meaning when there is appreciable absorption in the layer (the absorption coefficient becomes negative for 1200 to 350 nm spectral range). Only meaningful results are in the near UV spectrum. At 300 nm the value of α is $2.12X10^4 cm^{-1}$.

To characterise the coating, the measurements relating to this material were done by applying the material on glass slab of 10 by 10 cm^2 area. As this material was applied by spraying, the exact thickness of the material could not be estimated. This problem was also present when the refractive

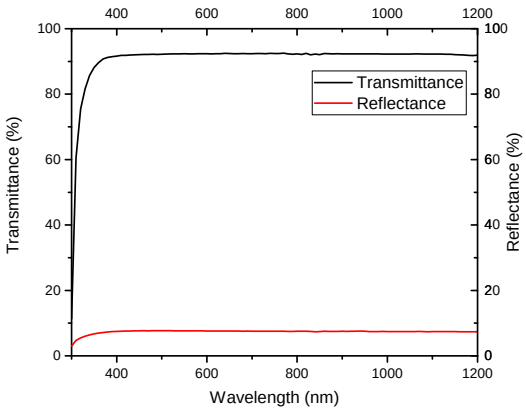

Figure 6.5: The transmittance and reflectance curve for the Conformal Coating used.

index was being determined. Hence to check whether this coating will increase reflection from the bottom cell or not, a small series of tests were done. In the tests, the reflection was measured from a c-Si wafer (S1), a c-Si wafer with a layer of conformal coating (S2), c-Si with conventional anti reflection coating (ARC) of 60 nm Silicon Nitride (S3) and c-Si with conventional ARC and a layer of conformal coating (S4). The plots are shown in the figure 6.6.

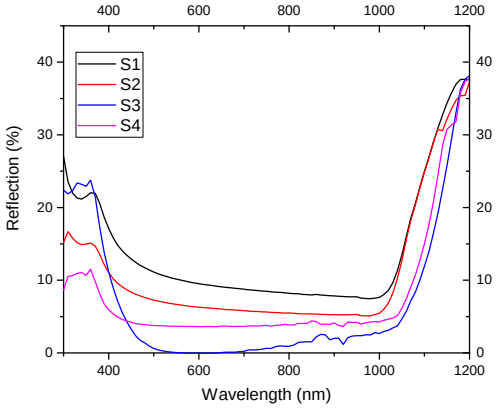

Figure 6.6: The reflectance in percentage for crystalline silicon wafer with No ARC (S1), Conformal coating (S2), ARC (S3) and ARC+Conformal Coating (S4).

It can be seen that although reflectance decreases by application of the conformal coating (S1 vs S2) it is not enough to bring it to the level of the ARC (S3). One reason could be that as this coating is sprayed on the sample, the layer thickness is not uniform. Visual inspection of the wafer revealed some glossy surfaces as seen in figure 6.7, which might have caused reflection. In case of an ARC the thickness of the Silicon Nitride layer is optimised to produce destructive interference but in case of conformal coating the control of thickness is not possible. To do so, a new process needs to be used such as, spin coating to produce uniform layers with the required thickness. Looking at S4, it can be observed that although the reflection is higher in the wavelength region of 450 to 1150 nm, it is substantially reduced in the near UV region as compared to S3. This can be attributed to absorption in this region which can also be seen in the transmission curve. The results from these tests prove that the conformal coating can be used as an ARC coating if the process of applying it is a controlled process. Another interesting observation during these experiments was that the silicon wafer (with ARC) turned black when conformal coat was applied as shown in figure 6.7. This also confirms that it has a potential to be used as an ARC.

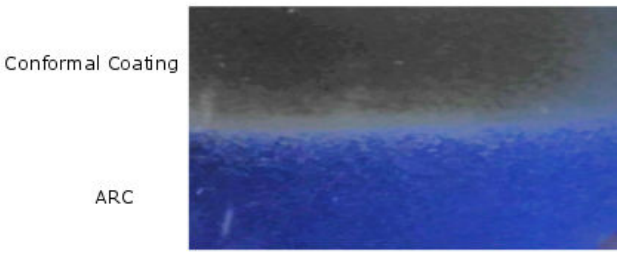

Figure 6.7: Actual image used for visual inspection of the silicon wafer with different coatings. The part shown as conformal coating contains both ARC and the conformal coat.

6.4. Final device fabrication and Results

The final four terminal device is fabricated using the a-SiO_x:H cell with 100 nm AZO transparent back contact as the top cell. The electrical parameters of this cell are listed in table 5.3. Three different types of c-Si cell namely- poly-Si, IBC and SHJ (Hybrid) cells developed in the PVMD group were used as the bottom cell. To make the front contact of the bottom cell, a wire was connected with silver paste to the metal busbar as shown in figure 6.8. This is done because the front contact of the bottom cell is fully covered with the top cell. Then the sample was annealed for one hour to cure the silver paste. In this way, the front connection of the bottom cell was formed. A glass slide of 700 um is used between the top cells to provide complete electrical isolation. This also provides mechanical stability to the cell. The electrical parameters of the bottom cells, prior to the development of the four terminal device, are provided in the table 6.1.

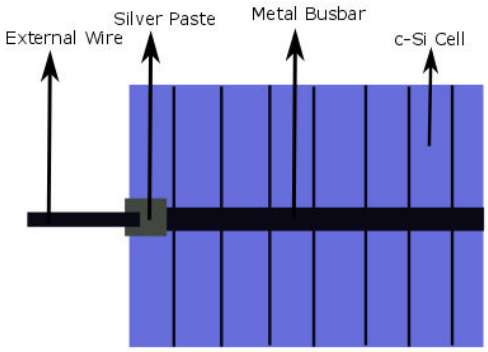

Figure 6.8: Schematic of the c-Si cell the silver paste is attached to the metal busbar.

Table 6.1: Electrical Parameters of the bottom cells used for the actual development of four terminal device.

Bottom cell	V_{oc}(V)	J_{sc}(mA/cm^2)	Fill Factor	Efficiency(%)
poly-Si	0.67	32.76	0.59	12.87
IBC	0.71	32.86	0.70	16.33
SHJ (Hybrid)	0.68	36.27	0.63	15.54

From the above table it is clear that the bottom cells are not of very high efficiency. The performance of these cells is lower than the bottom cells used in chapter-3. The fill factors of the poly-Si cell and the SHJ (hybrid) cell are quite low, a probable reason of this could be the formation of a high resistance silver-aluminium alloy, when the silver paste is applied to form the connection. This was seen in the increased series resistance of the cells before and after addition of the silver paste and the metal wire. These cells will be used to develop the four terminal devices. Then the new parameters will be analysed. The EQE of the above bottom cells before applying the top cell are shown in the figure 6.9.

Thus, utilising the above bottom cells, the four terminal cells were developed. The actual images of the devices are shown in figure 6.10. In figure 6.11, the four terminals are shown for the four terminal

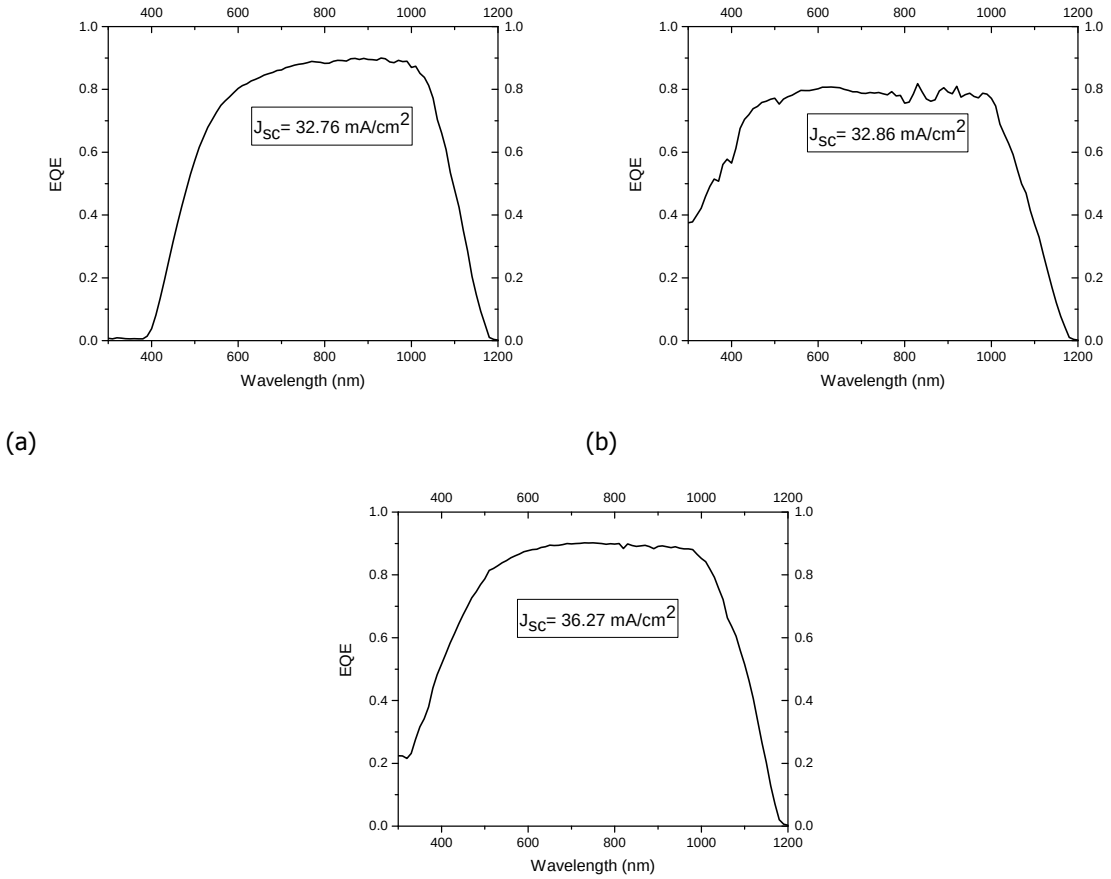

Figure 6.9: EQE of the bottom cell- a) poly-Si b) IBC c) SHJ (Hybrid) cell. The J_{sc} of the cells are written in the plot.

cell with a poly-Si bottom cell. The terminal-1 and 2 refer to the front and back contacts of the top a-SiO_x:H cell. While the terminal-3 and 4 are the front and back contacts of the bottom c-Si cell. For the four terminal cell with IBC back contact the figure 6.12 shows the four terminals. As clear from the image both the terminal 3 and 4 lie at the back of the bottom cell. All the measurements of the bottom cell were taken with the front cell short circuited. This is done to avoid any possible luminescent coupling, which might impact the bottom cell parameters[22, 23].

The electrical parameters of the bottom cell in the four terminal configuration are shown in table 6.2. As clear from the parameters obtained, there is a drop in V_{oc} of the bottom cell. This can be related to the reduced current generation in the bottom cell. Mathematically, the photo current is related to V_{oc} by a logarithmic function (Shockley diode equation). A quite interesting observation can be made about the fill factor. The fill factor for poly-Si and IBC cell has increased, when they are utilised in the four terminal configuration. For the SHJ (Hybrid) cell the fill factor has fallen. The electrical parameters are deduced from current density-voltage plots and the EQE measurements.

Table 6.2: Electrical Parameters of the bottom cells in the four terminal configuration.

Bottom cell	V_{oc}(V)	J_{sc}(mA/cm^2)	Fill Factor	Efficiency(%)
poly-Si	0.66	16.72	0.61	6.73
IBC	0.64	16.71	0.76	8.13
SHJ (Hybrid)	0.66	17.38	0.58	6.65

The EQE plots of the four terminal devices are shown in figure 6.13. The EQE plots show a drop in the J_{sc} of the bottom cell. Using the values of efficiencies mentioned in the table 5.3 for the top

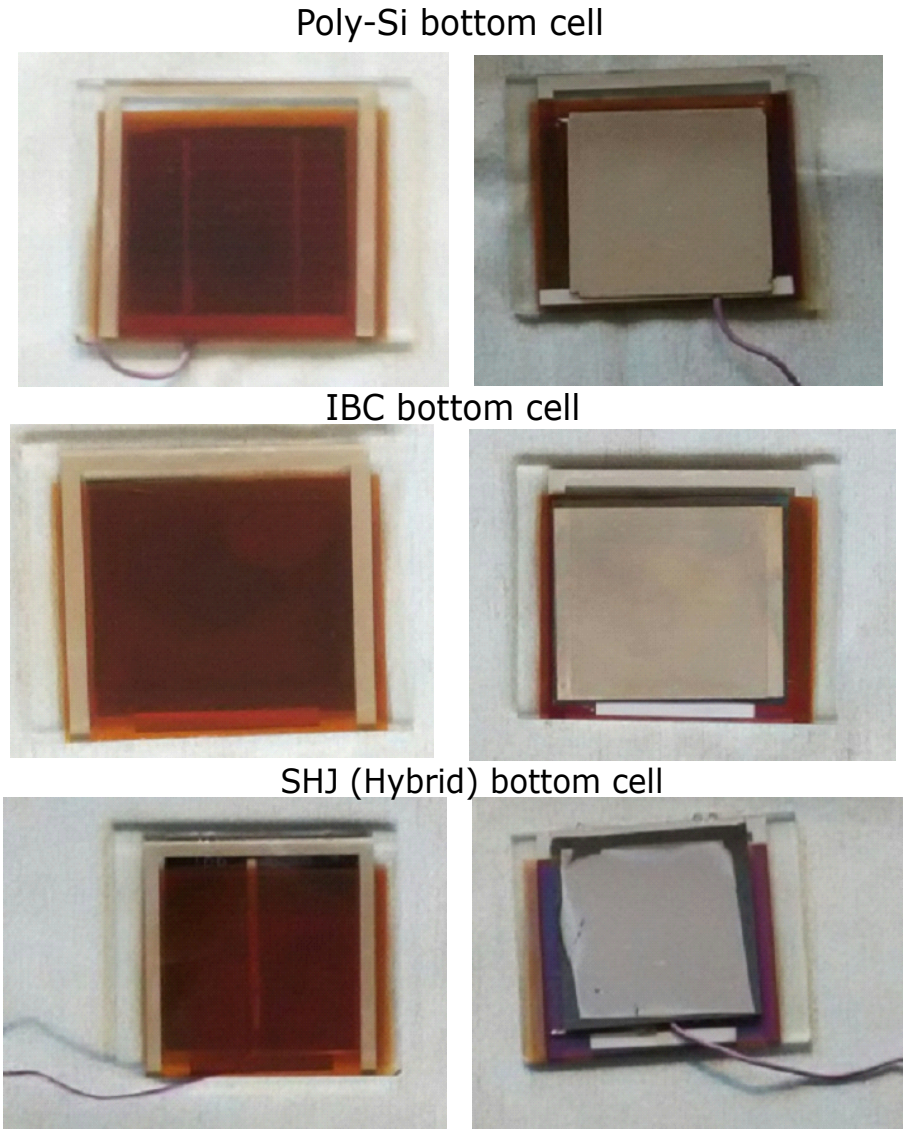

Figure 6.10: Actual image of the four terminal cell with poly-Si, IBC and SHJ (Hybrid) bottom cell from top side at the left side and back side at the right side.

a-SiO_x:H cell with 100 nm AZO back contact and table 6.2 for the bottom cell, the efficiency of the four terminal device can be computed. The total efficiency is the sum of the efficiency of the top cell and the bottom cell in four terminal configuration. The corresponding values are shown in table 6.3.

Comparing the efficiency of poly-Si cell without the top cell and in four terminal configuration, there is a rise of 0.46% (12.87 vs 13.33 %). With IBC and SHJ (Hybrid) cells, there is a loss of 1.6% and 2.29%, respectively. This huge loss in the efficiencies needs to be analysed in detail. One major reason is the parasitic absorption in the AZO layer. It has been mentioned earlier, that eventhough optimisation of AZO layer was tried, it is still not near the ideal TCO required for four terminal application. Putting our focus back on the EQE plots for the bottom cells, some more loss mechanisms can be identified. Comparing the EQE plots for poly-Si cell as shown in figure 6.14, there is a decrease in EQE values in

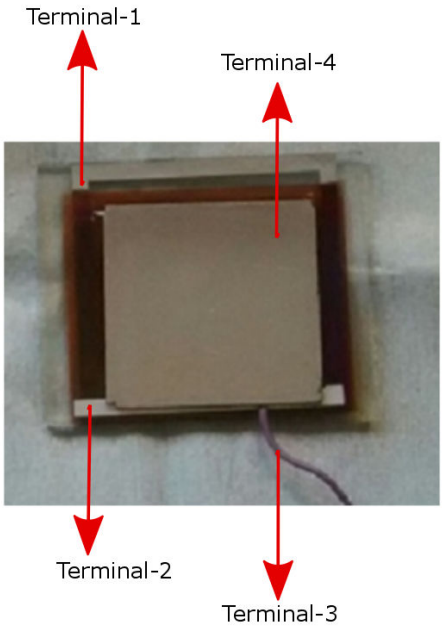

Figure 6.11: Actual image of the four terminal cell with poly-Si cell, all the terminals are marked in this image.

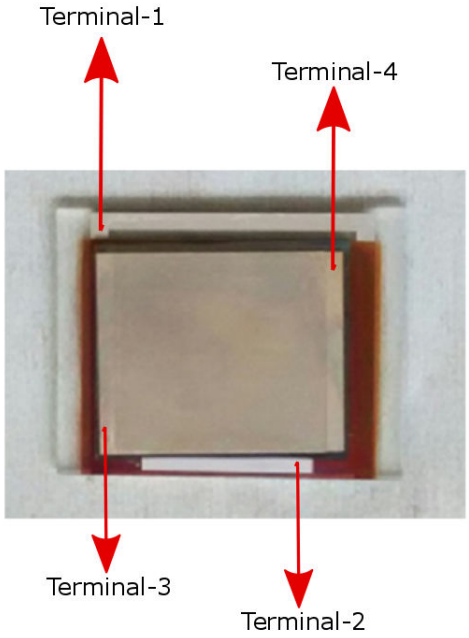

Figure 6.12: Actual image of the four terminal cell with IBC cell, all the terminals are marked in this image.

Table 6.3: Efficiency of the four terminal devices.

Cell	Efficiency(%)	Total Efficiency(%)
a-SiO_x:H	6.60	
poly-Si	6.73	13.33
IBC	8.13	14.73
SHJ (Hybrid)	6.65	13.25

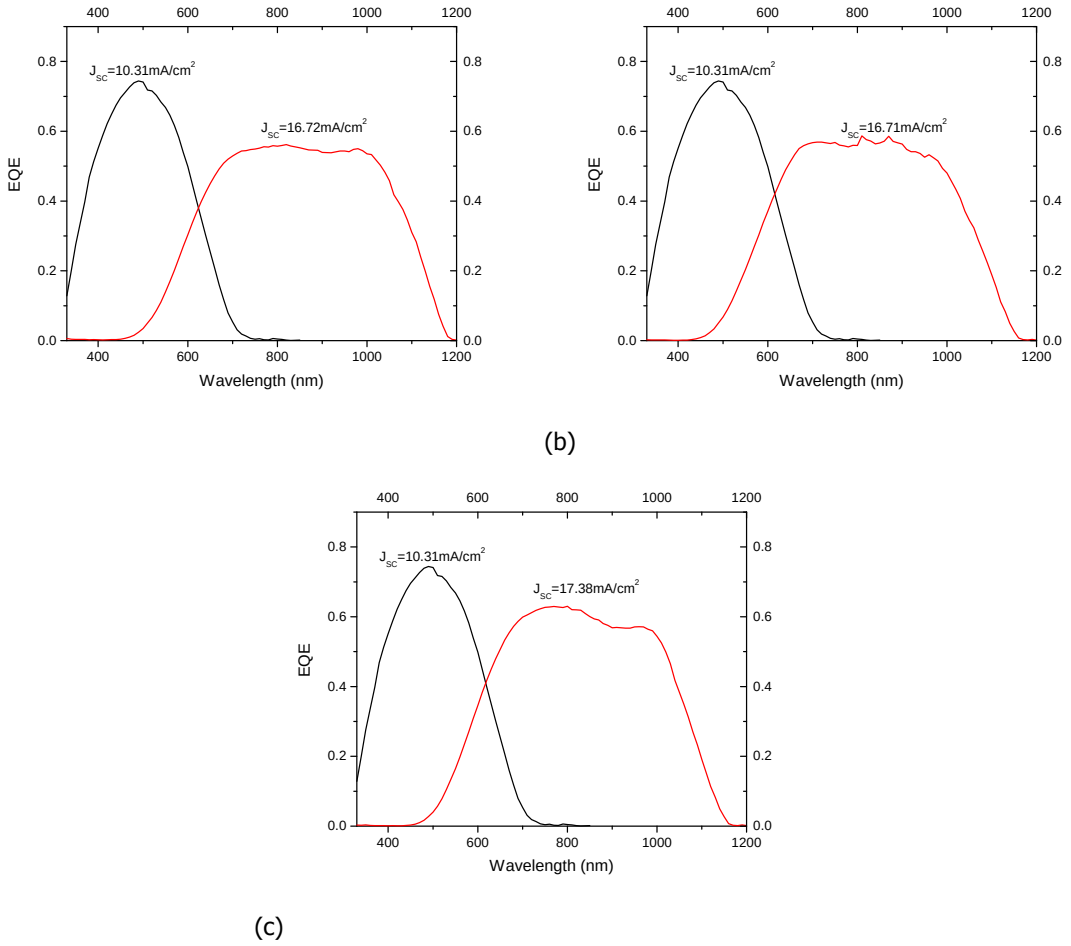

Figure 6.13: EQE of the four terminal cells with a-SiO_x:H top cell and bottom cell of a) poly-Si b) IBC c) SHJ (Hybrid) cell. The black and red curve correspond to the top and bottom cell respectively.

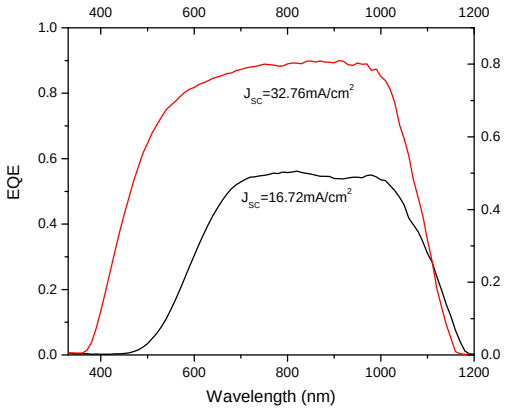

Figure 6.14: The comparison between EQE for poly-Si cell without top cell (black curve) and with top cell (red curve).

the visible and the IR spectrum. The probable reason for the decrease in the visible region, can be explained on account of the absorption in the a-SiO_x:H top cell. The decrease in IR region is probably, because of enhanced reflection from the top cell. In the other four terminal cells, similar losses are observed.

To analyse the reflection losses, the reflectance of the four terminal devices are measured. The

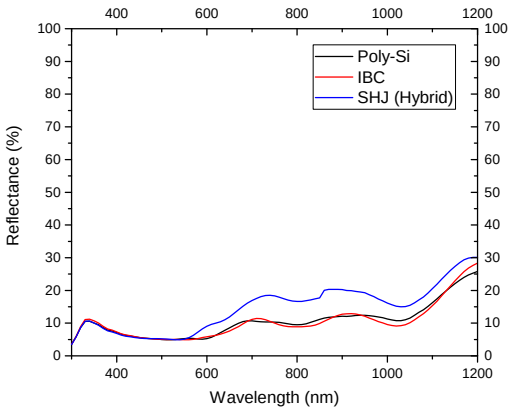

Figure 6.15: The reflectance of four terminal device. The bottom cells used in the four terminal device are mentioned in the figure.

plot of reflectance versus wavelength for the three cells is shown in figure 6.15. The reflectance curve shows very high reflection in the IR range, about 11.5 % of the spectrum incident on the poly-Si cell is reflected in the 600 to 1000 nm range. This range is taken because the c-Si cell have the best EQE values in this region. So the impact of a reduction in the high EQE region will be more profound on the J_{sc}. The reflectance of IBC cell is 10 % in the same spectral range whereas there is a tremendous loss of 16.75 % for the SHJ (Hybrid) bottom cell. Another spectrum range can also be defined, as 600 to 1108 nm (bandgap of Silicon). In this range, the average reflectance is 10.92 % for the four terminal cell with poly-Si bottom cell, 10.35% for IBC cell and 16.84% for SHJ cell. This reflectance loss clearly accounts for a low EQE. With the reduced EQE, there is a decrease in J_{sc} of the bottom cell. This leads to a low efficiency of the bottom cell.

Theoretical calculations with SR_{4T} parameters are also performed and they give an efficiency rise of 2.72% for the four terminal cell with poly-Si bottom cell. This value is almost 4 times the measured value. Similarly, the gain for IBC cell is 0.60% and for SHJ (Hybrid) bottom cell is 1.22%. Though in actual device there was a loss for both the IBC and SHJ (Hybrid) case. This also supports the fact that the loss in the bottom cell current is way to high to achieve high efficiencies. The plot of SR_{4T} are shown in appendix B.4.

6.5. Conclusion

Finally, four terminal cells utilising a-SiO_x:H top cell and c-Si bottom cells have been developed. These are the first four terminal cells developed using a-SiO_x:H and c-Si cells in the world. Three different types of four terminal cells with different c-Si bottom cells were characterised and analysed. A new type of organic adhesive called conformal coating has been studied and its optical properties have been characterised. The anti reflection potential of this coating has also been realised. There is an efficiency gain of 0.46% for the four terminal device when a poly-Si bottom cell is utilised as compared to the two terminal poly-Si cell. Although there is no gain for IBC and SHJ (Hybrid) bottom cells in the first prototypes. But with reduced reflection loss and high performing bottom cells, a larger gain can be easily realised.

7

Optical Analysis Using GenPro4 Simulations

7.1. Introduction

In the previous chapter four terminal cells have been developed. Still, there is a lot of scope in the efficiency gain that can be realised with these devices. This chapter is dedicated to optical simulations utilising GenPro4 [99, 100]. This software is developed in PVMD group to figure out all the important optical parameters related to a solar cell by utilising wave and ray optics. These simulations give the absorptance of each layer in terms of the current generated by them. This value of current is related to the product of absorption of the layer (number of photons absorbed) and AM1.5 (Global) spectrum. This leads to a good approximation that the absorptance of the absorber layer can be used to calculate the short circuit current density of the cell [100]. Also, the optical losses can be estimated from the value of the current obtained from the simulations results. The main goal of this chapter is to analyse the room for improvement in the four terminal configuration from an optical point of view. Towards the end of this chapter, an idealised condition is utilised to estimate the efficiency of the four terminal cell. In this chapter, the parameters of the bottom cells mentioned in Chapter-3 will be utilised. The reason for this is that the cells used for actual development of the four terminal cells in the previous chapter were of inferior quality. It seems more logical to consider more optimised and higher efficiency devices for simulation. So the simulations in this chapter are considered as a tool to investigate the potential of the a-SiO_x:H and c-Si four terminal cell.

7.2. GenPro4 Simulations

In this section, simulation results are presented. The current generated from the top and bottom cell, mentioned in the plots of the EQE, is calculated by taking into account the absorption in the absorber (active) layer [100]. This current is used to calculate the efficiency of the cells by taking into account the parameters mentioned in the table 7.1 and the table 4.3. The simulation results for top and bottom cell are given in figure 7.1, which is followed by the results when they are used in four terminal configuration. The structure of the top a-SiO_x:H is the one as developed in chapter-4. The structures of the bottom cells are shown in the figure 2.5. In the simulations, only silver is shown as the back contact, because the transmission through silver is zero for the required part of the spectrum.

In figure 7.1, the simulated EQE plots of the cells are given, when they are optically isolated (i.e. before four terminal configuration). These values are obtained from the results of the absorption calculated in the simulation. The concerned results are provided in the appendix B.5.1. As compared to the experimental values of the a-SiO_x:H cell a difference in the short circuit current density in the simulations is present. The difference in these values can be attributed to the electrical losses such as the series and shunt resistances which come into play when measurements are done. One more contributing factor to the losses is the recombination and deterioration at the p/i and i/n interface [81, 82, 101]. The actual structure of the thin film cell contains some buffer layers which can have parasitic absorption. These layers are not utilised in the device simulations. In the case of c-Si cells,

there are reflection and shading losses due to the front metal grid. These are also not taken into account in the simulation.

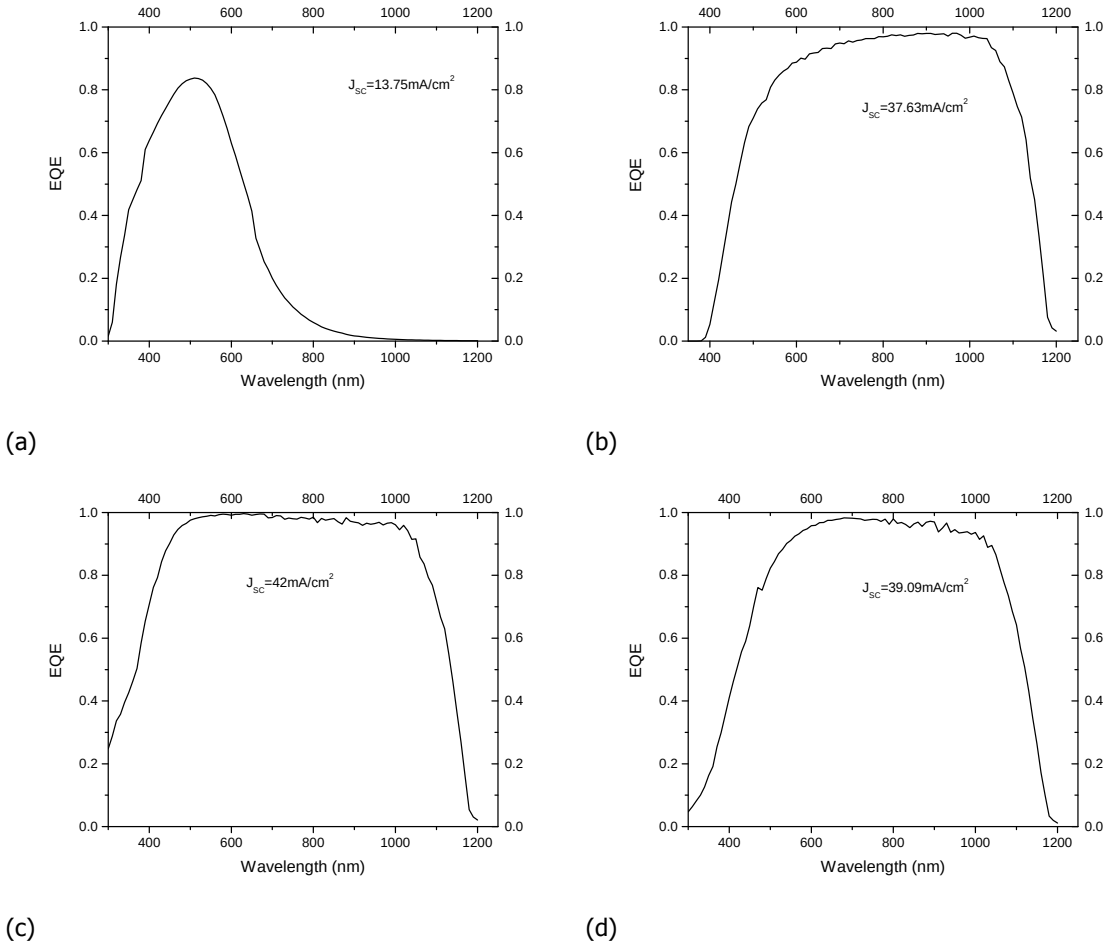

Figure 7.1: EQE of the (a) a-SiO$_x$:H cell. (b) poly-Si cells (c) IBC cell (d) SHJ (Hybrid) cell.

Table 7.1: Electrical Parameters of the simulated cells. The V_{oc} and fill factor used are taken from table. 3.2 for the bottom cells. For the top cell the parameters (Cell-B) are taken from table. 4.3.

Cell	V_{oc}(V)	J_{sc}(mA/cm^2)	Fill Factor	Efficiency(%)
a-SiO$_x$:H	1.003	13.75	0.67	9.24
poly-Si	0.68	37.63	0.66	16.88
IBC	0.70	42.00	0.70	20.44
SHJ (Hybrid)	0.69	39.12	0.71	19.16

The simulation uses the structure of the layers as shown in the figure 7.2. There is texturing at the interface between Asahi glass and the thin film a-SiO$_x$:H cell. The c-Si wafer used has pyramidal texturing. Both the textures are simulated in the GenPro4 simulations. The schematic for the four terminal cell with the poly-Si bottom cell is shown. A similar structure is used in all the other simulations. For the IBC bottom cell the four terminal structure is shown in appendix B.5.1.

The analysis of losses in the four terminal device can be done in terms of current (absorption). But it will be interesting to see the effect of the losses on the total efficiency of the device. For this purpose, some of the experimental values are used. The table 7.1 contains the values of the V_{oc} and fill factor from the experimental data, whereas the value of J_{sc}(mA/cm^2) is taken from the simulations. The results pertaining to the J_{sc}(mA/cm^2) are presented in the figure 7.3. It should be clear that in the simulations for four terminal cells an intermediate layer of 100 μm of EVA (Ethylene vinyl acetate) is

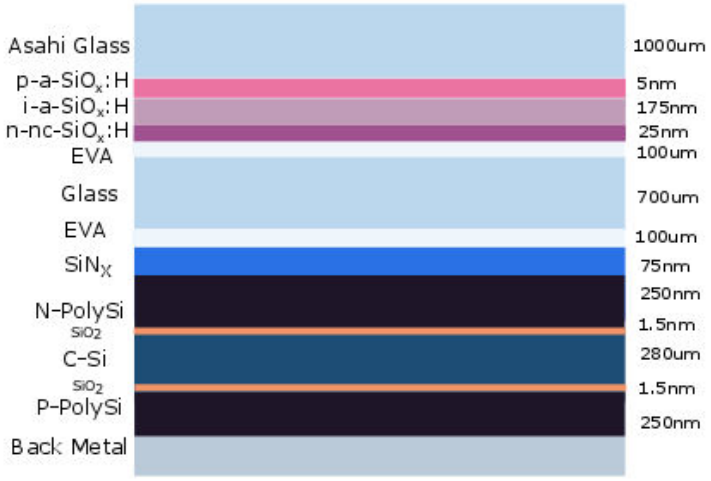

Figure 7.2: Schematic of the layer structure for the four terminal cell with poly-Si bottom cell used for simulations. The textures present at the interfaces are not shown in this schematic.

used as adhesive in between the two cells with an intermediate glass slide to give it mechanical stability. Usually, for this purpose industrial glues such as Tra-Bond-931-1, Loctite Eccobond 931-1 or silicon oil have been used in literature. The reason for this is the requirement of refractive index matching with the bottom cell so as to avoid reflection losses and electrical insulating properties of these materials. EVA is used as the adhesive because of its nearly transparent and electrically insulating properties. As clear from the previous chapter the use of conformal coating requires more optimisation. The optical parameter identification of this material is difficult due to a lack of a good model for spectroscopic ellipsometry. This is the reason for use of EVA in the optical model.

It is clear that by using four terminal approach the current in both the top and bottom cell reduces, that means that V_{oc} of the two cells should be scaled accordingly. The drop in V_{oc} of the cells is calculated by using ideal Shockley diode equation. It is important to note that the ideality factor in the case of crystalline silicon cells is taken as 1 [102]. Experimental data of V_{oc} and fill factor from the table 5.3 are used for the a-SiO_x:H cell. The new parameters are provided in the table 7.2. The parameters in case of the a-SiO_x:H are mentioned only once as there is only a slight change in the current in case of the three cases as seen in the figure. 7.3.

Table 7.2: Electrical Parameters of the simulated cells in four terminal configuration. The V_{oc} for the bottom cells is scaled by using ideal Shockley diode equation.

Cell	V_{oc}(V)	J_{sc}(mA/cm^2)	Fill Factor	Efficiency(%)	Total Efficiency(%)
a-SiO_x:H	0.97	9.73	0.66	6.23	
poly-Si	0.67	25.49	0.66	11.27	17.50
IBC	0.69	26.53	0.70	12.81	19.04
SHJ (Hybrid)	0.68	25.55	0.71	12.34	18.57

The total efficiency of the four terminal cell is calculated from the values of the efficiencies from the table 7.2 by adding the efficiency of the top a-SiO_x:H cell with the bottom cell. Thus the total efficiency that can be obtained is 17.50% for the poly-Si cell, 19.04% for IBC cell and 18.57% for the SHJ (Hybrid) cell as shown in the table 7.2. Thus a gain of 0.62% is achievable with a poly-Si bottom cell, this gain is calculated by taking the reference efficiency from the table 7.1. There is a loss of 1.40% when IBC and 0.59% when SHJ (Hybrid) cell is utilised in four terminal topology.

A contrasting view as compared to the calculations from SR_{4T} in the table 3.3 in chapter-3 is obtained from the above calculations. Some of the reasons for this could be -

- The top cell used in calculations for SR_{4T} has a metal back contact hence the EQE is higher as

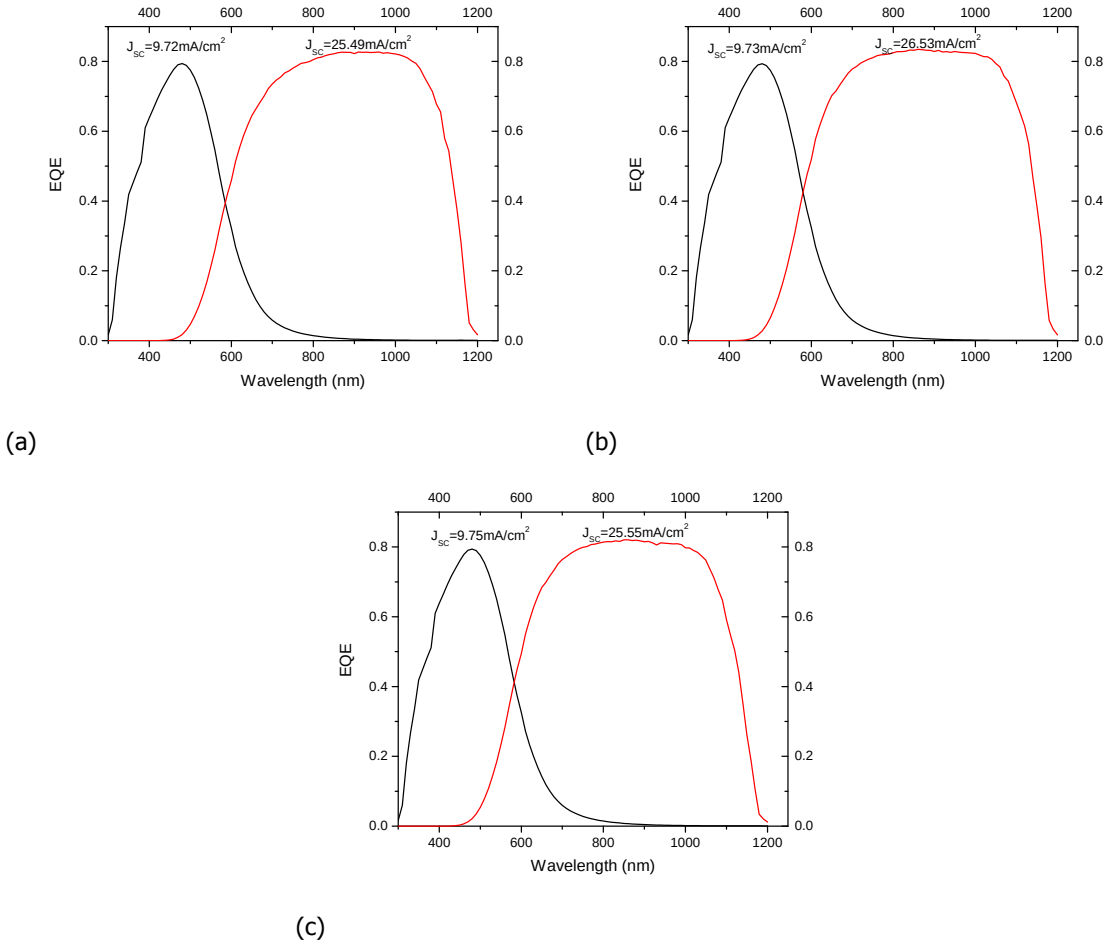

Figure 7.3: EQE of the four terminal cells with top cell of a-SiO_x:H cell and bottom cell of a) poly-Si b) IBC c) SHJ (Hybrid) cell. The black and red curve correspond to the top and bottom cell respectively.

compared to the ones used in the simulation of the four terminal cells. This is because of the increased optical path length due to back reflection from the metal back contact.

- The open circuit voltage of the bottom cell is taken to be constant in four terminal configuration in the calculation of SR_{4T}. Whereas in the case of simulations, it is taken into account according to the ideal Shockley equation.

- It is assumed in the calculations of the SR_{4T}, that the top cell does not absorb anything after the wavelength of approximately 600 nm. This aspect is not taken into account in the optical simulations.

7.2.1. Reflection Losses

Looking at the absorptance of the layers in the four terminal cell with the poly-Si bottom cell as shown in the figure 7.4, some important observations can be made. The reflection losses, account for 6.23 mA/cm^2, which is almost 13.5% of the absorption in the whole four terminal device. The value of reflectance is estimated from the absorptance in the air medium. This is because air is also simulated as a material, hence reflection loss is essentially the absorption in the air medium. There is a combined 2.68% loss (parasitic absorption) in the p and n layer a-SiO_x:H top cell. The poly-Si layer used in the c-Si cell accounts for 2.33 % of the total absorption. This parasitic loss is specific to the poly-Si cell only.

From the simulations and the figure 7.4, it can be seen that reflection loss is the dominant loss. The reason for this is that the optical system in case of four terminal cell has some interfaces that are not

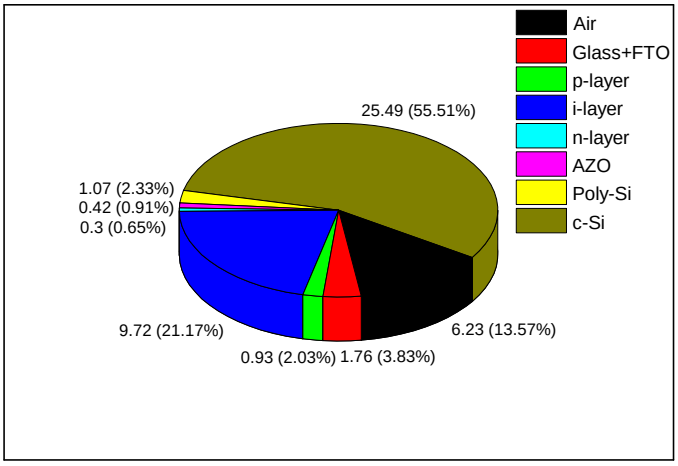

Figure 7.4: Pie chart of the absorption of the four terminal cell with poly-Si bottom cell. The absorption is in terms of current density mentioned near the corresponding area (mA/cm^2).

optimised for reduced reflection. This is because the materials utilised in the four terminal device have different refractive indexes. The comparison between the reflection loss for the bottom cell without and with the top cell is shown in the table 7.3.

Table 7.3: Reflectance at the air top cell glass interface in terms of current density (mA/cm^2).

Cell	Without Top Cell	With Top Cell
poly-Si	2.64	6.23
IBC	2.23	6.31
SHJ (Hybrid)	2.18	6.00

It can be seen that reflectance for four terminal case almost becomes 2.5 times the reflectance when the bottom cell is utilised without the top cell. Considering the result of one of the simulation i.e. poly-Si cell in four terminal configuration, the total reflectance can be divided into separate reflectance terms from the different interfaces of the four terminal device. This is done because GenPro4 takes into account reflection from all the interfaces and gives the sum of those values in the final results. Five major interfaces can be defined in these simulations as shown in the figure 7.5, with the specific reflectance terms- R_1, R_2, R_3, R_4 and R_5 respectively. This is done to see which interface contributes the maximum to the total reflectance. Even though there are some other interfaces in the actual structure, but simulation results did not give any major influence on the losses due to them. Hence they are not shown separately. The five major components as defined earlier can be identified by carefully modulating the thickness of the layers [103]. This is shown in appendix B.5.2. It must be noted that the schematic shown in figure 7.5 is only a sketch, the actual path of light will be determined by Snell's law.

From simulation results, the values of corresponding reflectance terms are shown in table 7.4. The corresponding simulation results are shown in appendix B.5.2 and in the appendix table B.2.

Similarly, the reflectance components for the IBC and SHJ (Hybrid) cell can be estimated. The simulation results for those are mentioned in appendix B.5.2. Reducing the reflection losses by application of anti reflective coatings (ARC) and texturing on the front side of the top cell looks promising, although this will add to the processing steps. According to literature, this will lead to a significant drop in the R_1 term. A set of simulations were done, where the use of a single layer ARC of magnesium fluoride (MgF_2) (quarter-wave coating) as an ARC is studied. Although ideally if a material with 1.22 refractive index is used, the best single layer ARC film can be developed. The thickness of the material is taken according to the quarter wave coating at 500 nm. The refractive index of the ARC material is taken to be constant and without any absorption [104].

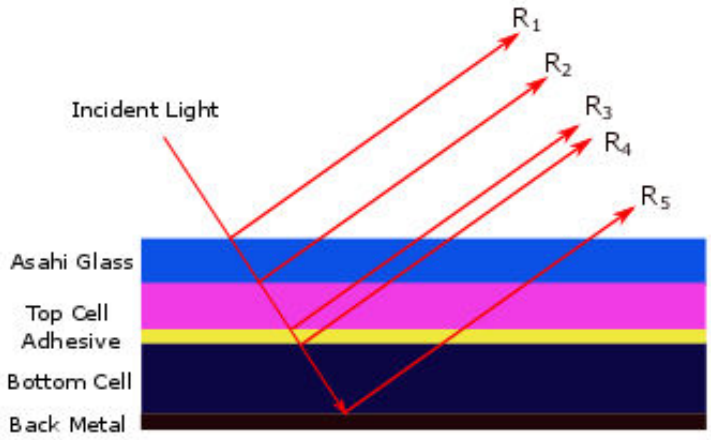

Figure 7.5: Schematic of reflection losses at the interfaces of the four terminal device. To determine the exact path of light Snell's law should be applied.

Table 7.4: Numerical value of each reflectance term in terms of current density (mA/cm^2) obtained from the simulations.

Reflectance Term	Numerical value
R_1	1.82
R_2	2.29
R_3	1.16
R_4	0.05
R_5	0.90

It is also interesting to note that by using pyramidal texturing, which is similar to the one used on crystalline silicon-lower reflection was observed. This is also supported by literature [25]. Three tests were done to see the influence of texturing on the front surface of the glass. These were- no texture, pyramidal texturing, texturing similar to the Asahi glass bottom texture. The pyramidal texturing on the glass surface needs a lot of experimental optimisation steps. This is because there is a requirement to achieve a balance between the etching time and the concentration of acid for achieving pyramidal structures. Also, the TCO at the bottom of the glass needs to be protected from the etching steps. This process is quite complex and time consuming process hence it was not tested experimentally. Though, this kind of approach has been applied in the case of perovskite and c-Si tandem device fabrication to reduce reflection losses [105]. But till now there is no good procedure available to apply this with thin film a-SiO_x:H cells.

Combining both the ARC and pyramidal texturing on the front side of the glass there is a reduction in reflection losses. The schematic shown in the figure 7.6 shows the pyramidal texturing and ARC of magnesium fluoride (MgF_2) of 90 nm thickness. This structure was used for the simulations. The simulation results pertaining to the ARC materials and texturing are presented in the table 7.5 and 7.6. Clearly, the reflectance of the four terminal device can be reduced by almost 30%, when a pyramidal texturing with an ARC coating is used. The GenPro4 results for the different bottom cell with an ARC of MgF_2 are provided in appendix B.5.2. Simulations with double ARC coatings of MgF_2 and Al_2O_3/CeF_3 were also tried but the results did not give a significant reduction in the reflection loss.

Table 7.5: Reflection losses in terms of current density (mA/cm^2). Only the results with pyramidal texturing which is similar to silicon wafer are given.

Bottom Cell	Reduced Reflection loss
poly-Si	4.28
IBC	4.44
SHJ (Hybrid)	4.14

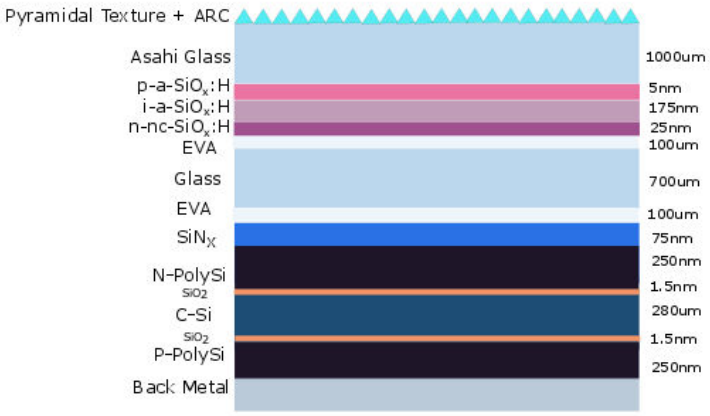

Figure 7.6: Schematic of the layer structure for the four terminal cell with poly-Si bottom cell used for simulations. The textures present at the interfaces in the two cells are not shown in this schematic.

The same approach as explained above is used to calculate the new reflectance terms. The new reflectance terms after the application of an ARC and pyramidal texture are shown in the table 7.6. Comparing these results with the previous results in the table 7.4, the term R_1 has reduced by 97%. This means that this approach is promising for reducing the reflection loss from the front side of the glass substrate which is used for a-SiO_x:H cell. The R_2 term has also reduced, but a rather interesting observation is the increase in the R_3, R_4 and R_5 terms. Though this increase is less than the overall reduction, still this is quite interesting. A reduction of almost 30% in total reflectance is obtained by utilising ARC and pyramidal texture.

Table 7.6: Numerical value of each reflectance term in terms of current density (mA/cm^2) obtained from the simulations with ARC and pyramidal texturing.

Reflectance Term	Numerical value
R_1	0.06
R_2	1.64
R_3	1.35
R_4	0.14
R_5	1.09

With texturing and ARC coating, there is an increment in the current for both the top and bottom cells. The J_{sc} of the a-SiO_x:H cell has improved by almost 0.64 mA/cm^2 (9.73 vs 10.37 mA/cm^2). The J_{sc} of the top cell is taken from the average of the results in figure 7.7. Thus the new efficiency of the top cell becomes 6.64% (10.37 mA/cm^2 $\cdot$ 0.97 vs $\cdot$ 0.66). This value is now used to calculate the new total efficiency of the four terminal cells. By taking the electrical parameters from the table 7.2 and the J_{sc} from the simulation with reduced front reflection from the figure 7.7, the efficiency of the four terminal cells is calculated. An efficiency of 18.30% (6.64+11.66%) with the poly-Si bottom cell is obtained. Thus an improvement of 1.42% (18.30% vs 16.88%) can be realised if front texturing and an ARC coating are used in four terminal configuration. This gain is 0.80% larger as compared to the efficiency when no front reflection reduction approach was applied (18.30% vs 17.50%). Similarly, for IBC cell, an efficiency of 19.89% (6.64+13.25%) is obtained. There is no gain in the four terminal cell with IBC bottom cell. For the SHJ (Hybrid) cell an efficiency of 19.39% (6.64+12.75%) can be obtained. This implies that by reducing the front reflection- an increase of 0.23% (19.39% vs 19.16%) can be obtained. From the table 7.5, it can be observed that the reflection loss for IBC bottom cell is the highest. More simulations were performed to verify this fact. The results of the simulations also support that reflection in case of IBC cell is maximum, out of the three bottom cells. More analysis into this odd behaviour of IBC cell needs to be explored.

From the above results, it becomes clear that optimum ARC coupled with a textured front surface

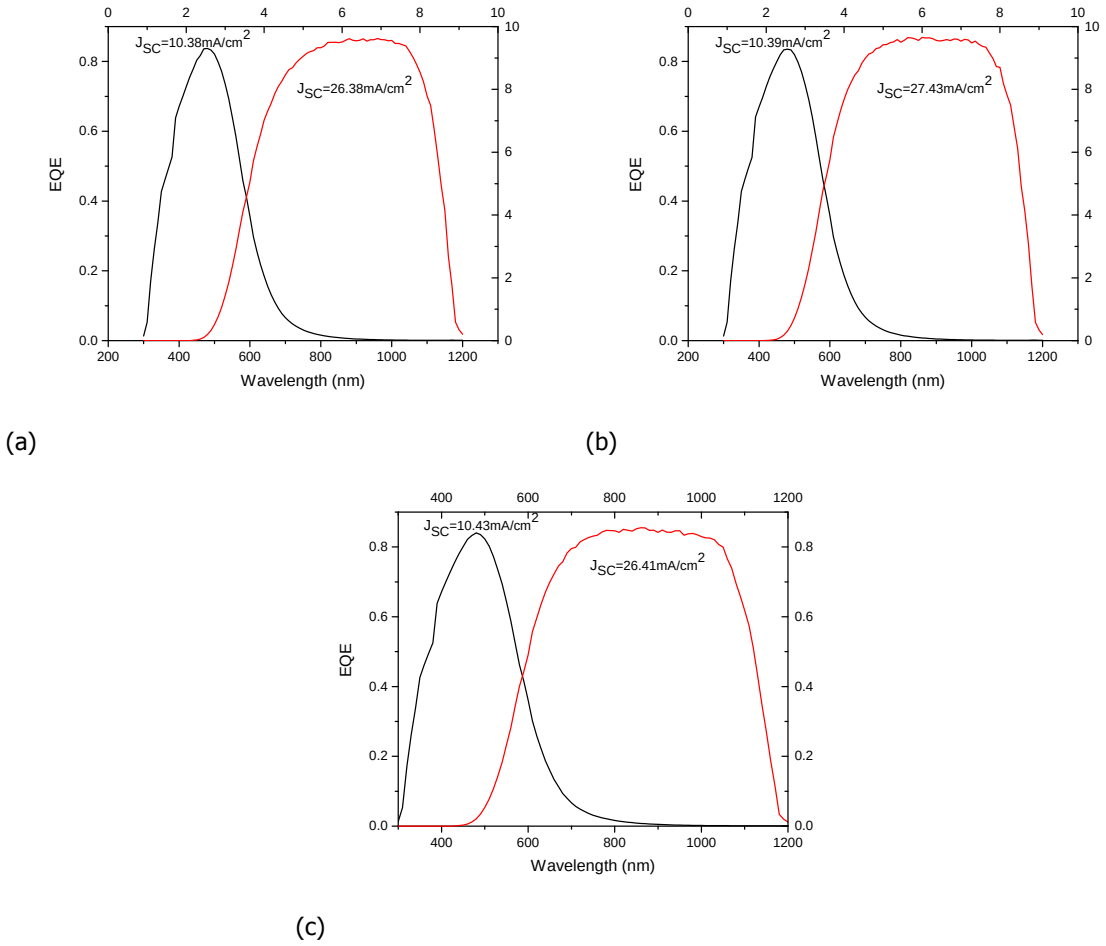

Figure 7.7: EQE of the four terminal cells with top cell of a-SiO_x:H cell and bottom cell of a) poly-Si b) IBC c) SHJ (Hybrid) cell after reduction of front reflectance. The black and red curve correspond to the top and bottom cell respectively.

reduces reflection losses and hence increases the total efficiency of the four terminal cells. More optimisation targeting the specific reflectance terms can further reduce the overall reflection.

The loss component R_2 accounts for almost 37% of the total reflection loss. This component can be reduced further by optimising the rear texture of the Asahi substrate used for the thin film cell. For this purpose simulations were performed. In the simulations, the height, as well as the width of the textures (Asahi textures), was changed. Another set of simulations were done by using three of the textures developed in PVMD group. Only a slight reduction in reflection was obtained. This could be because these textures are not optimised for use as rear textures. More optimisation of these textures is not performed in this work. Another approach that could be utilised is the application of an intermediate layer. This requires an optical model, so as to calculate the refractive index of the layer. This approach can be utilised in future work. The reflectance component from AZO and EVA interface (R_3) also contributes to the total reflection loss. The reduction of this can be accomplished by adding an intermediate layer between the two materials. The intermediate layer must be non absorbing. Another approach could be to modulate the refractive index of AZO layer by changing the amount of Aluminium in AZO or its deposition parameters [106]. Though this optimisation may be beneficial according to optics but will require significant optimisation to obtain appreciable electrical parameters (V_{oc} and fill factor) for the top cell. The other two components (R_4 and R_5) can also be reduced by using some refractive index grading or buffer layers.

7.2.2. Ideal Conditions

A calculation can be done by considering an ideal ARC and the best texture such that there is no excess reflection loss when the top cell is applied. Thus all the excess reflected photons are transferred to the bottom cell absorber layer. So, the current in the bottom cell becomes the sum of the current calculated from reduced reflection loss (in term of current density) from the table 7.3 and the generated current mentioned in table 7.2. This will yield enhanced efficiencies, which can be seen in the table 7.7. This table is with an idealised assumption that the reflection by the top cell is mostly in the longer wavelength range (near-IR), hence the loss can be directly added to the bottom cell current. The other electrical parameters are taken from the table 7.2.

Table 7.7: Efficiency of the simulated cells in four terminal configuration, taking into account no excess reflection from the top cell.

Cell	Efficiency(%)	Total Efficiency(%)
a-SiO_x:H	6.23	
poly-Si	12.86	19.09
IBC	14.78	21.01
SHJ (Hybrid)	14.17	20.40

Thus a gain can clearly be seen in all the three cases- a gain of 2.21% (19.09 vs 16.88%) for the poly-Si bottom cell, 0.57% for IBC (21.01 vs 20.44%) and 1.24% (20.40 vs 19.16%) for the SHJ (Hybrid) based four terminal cells. The gain is calculated by taking the single cell efficiencies from the table 7.1.

Another important loss that can be identified from the simulation is the parasitic absorption in the p and n layer of the top cell. The magnitude of this loss is almost equal for every four terminal cell irrespective of the bottom cell. The values of current loss in these layers are mentioned in the table 7.8.

Table 7.8: Parasitic absorption in terms of the current density (mA/cm^2) in the p and n layer of the top cell when used in the four terminal stack.

Cell	p-layer	n-layer
poly-Si	0.93	0.30
IBC	0.93	0.29
SHJ (Hybrid)	0.93	0.29

So, almost 1.23 mA/cm^2 of current is lost in the carrier selective layers of the top cell as a parasitic loss. This loss is almost 12.64% of the total current, generated by the top cell in four terminal configuration. Thus if this loss is reduced, more current can be generated from the top cell, as well as more photons will be transmitted to the bottom cell. This can be done by making the layers thin and more transparent. Although a 100% reduction seems far fetched in an idealised scenario, the impact of this reduction can be analysed. Considering this loss to be zero, one can clearly see that if the current from p layer is transferred to the top cell and the n layer current is transferred to the bottom cell, the total efficiency will be enhanced. The results of the total efficiency are shown in the table 7.9. This is done by taking V_{oc} and fill factor from the table 7.2.

Table 7.9: Efficiency of the simulated cells in four terminal configuration, taking into account no parasitic absorption in the top cell n and p layers.

Cell	Efficiency(%)	Total Efficiency(%)
a-SiO_x:H	6.82	
poly-Si	11.40	18.22
IBC	12.95	19.78
SHJ (Hybrid)	12.47	19.29

This clearly shows an increased efficiency (except the IBC cell) as compared to the single cell efficiency. A gain of almost 1.34% is obtained when poly-Si cell is used as the bottom cell. Although

with the SHJ (Hybrid), a gain of 0.13 % is obtained. The parasitic losses can be reduced by using thin layers. But, the thickness of the layers have already been experimentally optimised to obtain appreciable electrical parameters. So, this approach is not used in simulations. Other way to reduce this loss is to make transparent layers. But that needs more optimisation on the deposition parameters so, as to change the refractive index and extinction coefficient of the layers. This task is left for future work.

This means that if the above two losses are reduced to an idealised situation, one can expect to obtain total efficiencies, which are shown in the table 7.10. In these calculations, the short circuit current density is taken such that both the losses are taken to be in an ideal condition. Then this current is essentially the sum of the generated current, excess current from the reflection losses and the current from the parasitic absorption.

Table 7.10: Efficiency of the simulated cells in four terminal configuration, taking into account no reflection losses and no parasitic absorption in the top cell n and p layers.

Cell	Efficiency(%)	Total Efficiency(%)
a-SiO_x:H	6.64	
poly-Si	12.99	19.63
IBC	14.92	21.56
SHJ (Hybrid)	14.32	20.96

This idealised situation shows the potential of four terminal approach- a gain of 2.75% for poly-Si (19.63 vs 16.88%), 1.12% for the IBC (21.56 vs 20.44%) and 1.8% for the SHJ (Hybrid) (20.96 vs 19.16%) as compared to two terminal devices can be obtained. These results are comparable to the values, obtained from the efficiency calculated by utilising SR_{4T} parameter. Thus in an idealised condition, the utilisation of four terminal approach can yields efficiencies in excess of 21%.

It is not possible to compare the results from Chapter-6 with the results from this chapter as the bottom cells used in the actual development of the four terminal devices do not have the same performance as the ones used in the simulation. Simulations are performed to identify the major loss mechanisms and provide an insight into, how these losses can be reduced. The aim of these simulations is not to replicate the experimental results in chapter-6.

Although the results from this chapter give an insight into the performance of the four terminal cells, they still can be improved by more optimisation. This opens up the possibility to develop dedicated top cell with reduced reflectance and a specific textured substrate. If all the additional losses are reduced, high efficiencies can be realised for a four terminal device.

7.3. Conclusions

The potential of the four terminal approach can be seen from the calculations utilising the simulation results from GenPro4. With the addition of a top a-SiO_x:H cell on a c-Si based cell, higher efficiencies can be obtained. The simulation results show that with an average performing poly-Si cell (16.88%) efficiency of almost 17.50% can be realised by simple application of a top a-SiO_x:H cell. Further analysis of the optical system points to two factors limiting the efficiency of the device. These are- Reflection losses and parasitic losses. Measures such as, pyramidal texture and ARC coating on the front side of the top cell, lead to a reduction of 30% in reflection losses. An idealised condition where both this losses are reduced, shows that efficiencies in excess of 21% can be obtained (this also depends on the electrical parameters of the bottom cell).

8

Conclusions and Recommendations

In past, many combinations of four terminal mechanically stacked solar cells have been developed, but in this thesis, a novel combination was developed. The novel device built in this work utilises an a-SiO_x:H top cell and c-Si bottom cell. Three types of bottom cells (Polycrystalline-Silicon (poly-Si), Interdigitated back contact (IBC) and Silicon heterojunction (SHJ (Hybrid)) are used to develop the four terminal cells. To accomplish the task of developing the four terminal device a systematic approach was followed. Firstly, the optimum configuration, as well as the efficiency gain of the four terminal cells, was assessed. This was followed by optimisation to achieve a suitable a-SiO_x:H based thin film cell. For the purpose of utilising the a-SiO_x:H cell as the top cell transparent conductive oxide (TCO) was required. The TCO was used as the back electrical contact of the top cell. After the selection of the optimum TCO layer, the final fabrication process of combining the top and bottom cell was undertaken. Finally, the devices fabricated were characterised and analysed. In the last part of the work, the devices were analysed using optical simulations.

Coming to the first step towards the development of the four terminal device, it was necessary to determine the best suitable combination for the top and bottom cell. For this purpose, numerical parameters called Response 4T (R_{4T}) and Spectral Response 4T (SR_{4T}) were developed. From these parameters, not only the suitable combinations but, the efficiency gain of a four terminal device as compared to the two terminal conventional device was also determined. The parameters show that it is theoretically possible to boost the efficiency of a c-Si cell by placing an a-SiO_x:H cell on top of it. The results of the numerical parameters suggest an absolute efficiency gain between 0.82% and 3.94% by utilising four terminal topology.

Optimisation of the top a-SiO_x:H cell and the TCO for its back contact was also undertaken in this work. The target of this optimisation was not only to obtain the best top cell in terms of electrical parameters (high V_{oc} fill factor product) but also to achieve high transmittance in the red and near IR spectrum. The reason for this is to have an appreciable current generation from the bottom c-Si cell. The optimum cell structure comprised of 5 nm p-a-SiO_x:H layer, 175 nm i-SiO_x:H-layer and 25 nm n-nc-SiO_x:H. The best TCO obtained was 100 nm AZO. An a-SiO_x:H cell with 100 nm AZO as back contact having an efficiency of 6.60% (V_{oc} of 0.97 V, 10.31 mA/cm^2 J_{sc} and 0.66 fill factor) was developed. This is one of the first efficiency reported for a bifacial a-SiO_x:H cell. Double layer of indium tin oxide and aluminium doped zinc oxide based TCO were also developed and analysed.

A dedicated fabrication process utilising a new type of adhesive called conformal coating was utilised to develop the final device. This work is the first instance where a conformal coating is used as an adhesive. The anti reflection property for application in the c-Si based cell of the conformal coating is also reported. This easy to apply coating not only has anti reflection properties but is also water and dust resistant. The first prototypes of the four terminal devices were built utilising some of the c-Si cells developed in PVMD group. These are the first four terminal mechanically stacked devices that are based on an a-SiO_x:H top cell and c-Si bottom cell in the world. An efficiency rise of 0.46% was obtained for the four terminal device based on poly-Si bottom cell. This gain is a clear indicator of the potential of the four terminal solar cell concept.

To investigate efficiency potential in more detail, optical simulations were performed. This was done by utilising an in house developed optical simulation tool- GenPro4. Reflection losses, as well as

parasitic losses, were studied and analysed in detail. Reflection losses from interfaces in the complex optical system of the four terminal device were determined. Strategies such as utilisation of front texturing and anti reflection coating for the top cell lead to a decrease in reflection loss by almost 30%. The impact of reducing these losses on the efficiency of the final device was also determined. The final results of simulations after the reduction of losses ascertain an increase in efficiency of 1.12% to 2.75% for the bottom c-Si cell.

8.1. Recommendations

From the work undertaken in this thesis, several recommendations for future work on this promising approach can be drawn. Some of these are-

- The calculations of Response 4T (R_{4T}) and Spectral Response 4T (SR_{4T}) suggest that if a top cell with higher V_{oc} fill factor product is utilised, higher efficiencies of the four terminal approach will be realised. So, development of a device with higher V_{oc} fill factor product should be done.
- The optimisation of the top cell of a-SiO_x:H can also be done by changing the material properties such as, the bandgap of the absorber or activation energy of the doped layers. Development of thin and more transparent carrier selective layers for the top cell should be done. This will reduce parasitic absorption in the four terminal cell. Large area thin film cells should be developed.
- A glass substrate with optimised texture could be used instead of the Asahi glass substrate for the deposition of the top cell.
- A more rigorous optimisation of TCO should be undertaken. To do so, deposition parameters of the TCO layer could also be varied.
- Double layers of ITO/AZO are good alternative to the single TCO layers but still they need more analysis and characterisations.
- The conformal coating used in this work, should be analysed and characterised in more detail. A dedicated process to apply a uniform thickness coating can be developed in future.
- Actual utilisation of the front texture and anti reflection coating for the top cell should be done. A more in-depth analysis into the type of texture for the top cell could be undertaken.
- One interesting thing that can be done, is the utilisation of a substrate configuration for the top cell. In this way the optical system can be simplified, as there will be no need of an intermediate glass between the top and bottom cell. This will require the use of transparent substrate, which can have dedicated texturing to enhance the four terminal device performance.
- The simulation tool, takes the absorptance value as the difference between the incident photon flux and the outgoing photon flux. This does not correctly yields the exact value of short circuit current in a four terminal device. So, a new model to take this into account should be used.
- If a top cell with textured surface and an ARC coating is utilised, then the ARC on the bottom c-Si can be removed. This will require more optimisation. This opens up the possibility to develop dedicated bottom cells for the four terminal application.

Bibliography

[1] Kaneka, *http://www.kaneka.co.jp/kaneka-e/images/topics/1473811995/1473811995*$_1$*01.pdf,* .

[2] K. Yoshikawa, H. Kawasaki, W. Yoshida, T. Irie, K. Konishi, K. Nakano, T. Uto, D. Adachi, M. Kanematsu, H. Uzu, *et al.*, *Silicon heterojunction solar cell with interdigitated back contacts for a photoconversion efficiency over 26%,* Nature Energy **2**, 17032 (2017).

[3] A. Richter, M. Hermle, and S. W. Glunz, *Reassessment of the limiting efficiency for crystalline silicon solar cells,* IEEE Journal of Photovoltaics **3**, 1184 (2013).

[4] A. Smets, K. Jager, O. Isabella, and R. Swaaij, *Solar Energy: The Physics and Engineering of Photovoltaic Conversion, Technologies and Systems* (UIT Cambridge, 2016).

[5] S. Essig, M. A. Steiner, C. Allebé, J. F. Geisz, B. Paviet-Salomon, S. Ward, A. Descoeudres, V. LaSalvia, L. Barraud, N. Badel, *et al.*, *Realization of gainp/si dual-junction solar cells with 29.8% 1-sun efficiency,* IEEE Journal of Photovoltaics **6**, 1012 (2016).

[6] D. E. Carlson, *Amorphous-silicon solar cells,* IEEE Transactions on Electron Devices **36**, 2775 (1989).

[7] Y. Matsumoto, G. Hirata, H. Takakura, H. Okamoto, and Y. Hamakawa, *A new type of high efficiency with a low-cost solar cell having the structure of a* μ *c-sic/polycrystalline silicon heterojunction,* Journal of applied physics **67**, 6538 (1990).

[8] W. Ma, T. Horiuchi, M. Yoshimi, K. Hattori, H. Okamoto, and Y. Hamakawa, *Approaching 20% efficiency with a-si/poly-si tandem solar cell,* in *Photovoltaic Specialists Conference, 1991., Conference Record of the Twenty Second IEEE* (IEEE, 1991) pp. 1380–1384.

[9] G. Yang, *High-efficient nip thin-film silicon solar cells*, Ph.D. thesis, TU Delft, Delft University of Technology (2015).

[10] L. Gupta, A. Mansingh, and P. Srivastava, *Band gap narrowing and the band structure of tin-doped indium oxide films,* Thin solid films **176**, 33 (1989).

[11] G. B. Haxel, J. B. Hedrick, G. J. Orris, P. H. Stauffer, and J. W. Hendley II, *Rare earth elements: critical resources for high technology*, Tech. Rep. (2002).

[12] R. van Schie, *Individual cell analysis of micromorph tandem solar cells,* (2016).

[13] D. A. Neamen, *Semiconductor physics and devices: basic principles* (McGraw-Hill Education, 2012).

[14] W. R. Thurber, *https://www.nist.gov/pml/engineering-physics-division/hall-effect,* .

[15] P. Inc, *Applications and Use of Integrating Spheres With the LAMBDA 650 and 850 UV/Vis and LAMBDA 950 UV/Vis/NIR Spectrophotometers, 2004. URL www.perkinelmer.com.*

[16] NREL, *http://rredc.nrel.gov/solar/spectra/am1.5/astmg173/astmg173.html,* .

[17] C. Philibert, *https://www.iea.org/publications/freepublications/publication/technologyroadmapsolarphotovoltaicenergy*$_2$*014edition.pdf,* .

[18] W. Shockley and H. J. Queisser, *Detailed balance limit of efficiency of p-n junction solar cells,* Journal of applied physics **32**, 510 (1961).

[19] J. D. McCambridge, M. A. Steiner, B. L. Unger, K. A. Emery, E. L. Christensen, M. W. Wanlass, A. L. Gray, L. Takacs, R. Buelow, T. A. McCollum, *et al.*, *Compact spectrum splitting photovoltaic module with high efficiency,* Progress in Photovoltaics: Research and Applications **19**, 352 (2011).

[20] P. Chiu, D. Law, R. Woo, S. Singer, D. Bhusari, W. Hong, A. Zakaria, J. Boisvert, S. Mesropian, R. King, *et al.*, *35.8% space and 38.8% terrestrial 5j direct bonded cells,* in *Photovoltaic Specialist Conference (PVSC), 2014 IEEE 40th* (IEEE, 2014) pp. 0011–0013.

[21] H. Sai, T. Matsui, T. Koida, K. Matsubara, *et al.*, *Triple-junction thin-film silicon solar cell fabricated on periodically textured substrate with a stabilized efficiency of 13.6%,* Applied Physics Letters **106**, 213902 (2015).

[22] S. Essig, S. Ward, M. A. Steiner, D. J. Friedman, J. F. Geisz, P. Stradins, and D. L. Young, *Progress towards a 30% efficient gainp/si tandem solar cell,* Energy Procedia **77**, 464 (2015).

[23] S. Essig, J. F. Geisz, M. A. Steiner, A. Merkle, R. Peibst, J. Schmidt, R. Brendel, S. Ward, D. J. Friedman, P. Stradins, *et al.*, *Development of highly-efficient gainp/si tandem solar cells,* in *Photovoltaic Specialist Conference (PVSC), 2015 IEEE 42nd* (IEEE, 2015) pp. 1–4.

[24] M. A. Green and K. Emery, *Solar cell efficiency tables,* Progress in Photovoltaics: Research and Applications **1**, 25 (2017).

[25] D. Zhang, W. Soppe, and R. E. Schropp, *Design of 4-terminal solar modules combining thin-film wide-bandgap top cells and c-si bottom cells,* Energy Procedia **77**, 500 (2015).

[26] J. Werner, L. Barraud, A. Walter, M. Bräuninger, F. Sahli, D. Sacchetto, N. Tétreault, B. Paviet-Salomon, S.-J. Moon, C. Allebé, *et al.*, *Efficient near-infrared-transparent perovskite solar cells enabling direct comparison of 4-terminal and monolithic perovskite/silicon tandem cells,* ACS Energy Letters **1**, 474 (2016).

[27] T. Duong, Y. Wu, H. Shen, J. Peng, X. Fu, D. Jacobs, E.-C. Wang, T. C. Kho, K. C. Fong, M. Stocks, *et al.*, *Rubidium multication perovskite with optimized bandgap for perovskite-silicon tandem with over 26% efficiency,* Advanced Energy Materials (2017).

[28] Y. Matsumoto, K. Miyagi, H. Takakura, H. Okamoto, and Y. Hamakawa, *a-si/poly-si two-and four-terminal tandem type solar cells,* in *Photovoltaic Specialists Conference, 1990., Conference Record of the Twenty First IEEE* (IEEE, 1990) pp. 1420–1425.

[29] D. Y. Kim, E. Guijt, R. A. van Swaaij, and M. Zeman, *Hydrogenated amorphous silicon oxide (a-sio x: H) single junction solar cell with 8.8% initial efficiency by reducing parasitic absorptions,* Journal of Applied Physics **121**, 133103 (2017).

[30] H. Sterling and R. Swann, *Chemical vapour deposition promoted by rf discharge,* Solid-State Electronics **8**, 653 (1965).

[31] D. E. Carlson and C. R. Wronski, *Amorphous silicon solar cell,* Applied Physics Letters **28**, 671 (1976).

[32] A. Luque and S. Hegedus, *Handbook of photovoltaic science and engineering* (John Wiley & Sons, 2011).

[33] K. W. Böer, *Handbook of the physics of thin-film solar cells* (Springer Science & Business, 2014).

[34] J. Tauc, *Optical properties of non-crystalline solids,* Optical properties of solids , 277 (1972).

[35] R. A. Street, *Doping and the fermi energy in amorphous silicon,* Physical Review Letters **49**, 1187 (1982).

[36] S. Inthisang, K. Sriprapha, S. Miyajima, A. Yamada, and M. Konagai, *Hydrogenated amorphous silicon oxide solar cells fabricated near the phase transition between amorphous and microcrystalline structures,* Japanese Journal of Applied Physics **48**, 122402 (2009).

[37] E. Chen, G. Du, Y. Zhang, X. Qin, H. Lai, and W. Shi, *Rf-pecvd deposition and optical properties of hydrogenated amorphous silicon carbide thin films,* Ceramics International **40**, 9791 (2014).

[38] M. Stutzmann, R. Street, C. Tsai, J. Boyce, and S. Ready, *Structural, optical, and spin properties of hydrogenated amorphous silicon-germanium alloys,* Journal of applied physics **66**, 569 (1989).

[39] L. V. Mercaldo, I. Usatii, and P. Delli Veneri, *Advances in thin-film si solar cells by means of siox alloys,* Energies **9**, 218 (2016).

[40] Y. Xu, B. Yan, B. P. Nelson, E. Iwaniczko, R. C. Reedy, A. Mahan, and H. Branz, *Devices fabrication with narrow-bandgap a-sige: h alloys deposited by hwcvd,* in *MRS Proceedings*, Vol. 808 (Cambridge Univ Press, 2004) pp. A9–51.

[41] B. Yan, G. Yue, L. Sivec, J. Yang, S. Guha, and C.-S. Jiang, *Innovative dual function nc-siox: H layer leading to a> 16% efficient multi-junction thin-film silicon solar cell,* Applied Physics Letters **99**, 113512 (2011).

[42] E. Guijt, *Application of intrinsic amorphous silicon oxide in multi-junction solar cells,* (2014).

[43] W. van Sark, L. Korte, and F. Roca, *Physics and technology of amorphous-crystalline heterostructure silicon solar cells* (Springer, 2012).

[44] A. Ingenito, G. Limodio, P. Procel, G. Yang, H. Dijkslag, O. Isabella, and M. Zeman, *Silicon solar cell architecture with front selective and rear full area ion-implanted passivating contacts,* Solar RRL .

[45] G. Yang, A. Ingenito, N. van Hameren, O. Isabella, and M. Zeman, *Design and application of ion-implanted polysi passivating contacts for interdigitated back contact c-si solar cells,* Applied Physics Letters **108**, 033903 (2016).

[46] G. Yang, A. Ingenito, O. Isabella, and M. Zeman, *Ibc c-si solar cells based on ion-implanted poly-silicon passivating contacts,* Solar Energy Materials and Solar Cells **158**, 84 (2016).

[47] P. J. Isherwood, N. Neves, J. W. Bowers, P. Newbatt, and J. Walls, *High quality aluminium doped zinc oxide target synthesis from nanoparticulate powder and characterisation of sputtered thin films,* Thin Solid Films **566**, 108 (2014).

[48] W. Beyer, J. Hüpkes, and H. Stiebig, *Transparent conducting oxide films for thin film silicon photovoltaics,* Thin Solid Films **516**, 147 (2007).

[49] W.-J. Jeong and G.-C. Park, *Electrical and optical properties of zno thin film as a function of deposition parameters,* Solar Energy Materials and Solar Cells **65**, 37 (2001).

[50] R. Mereu, S. Marchionna, A. L. Donne, L. Ciontea, S. Binetti, and M. Acciarri, *Optical and electrical studies of transparent conductive azo and ito sputtered thin films for cigs photovoltaics,* physica status solidi (c) **11**, 1464 (2014).

[51] A. Klein, C. Körber, A. Wachau, F. Säuberlich, Y. Gassenbauer, S. P. Harvey, D. E. Proffit, and T. O. Mason, *Transparent conducting oxides for photovoltaics: manipulation of fermi level, work function and energy band alignment,* Materials **3**, 4892 (2010).

[52] K. Badeker, *Electrical conductivity and thermo-electromotive force of some metallic compounds,* Ann. Phys **22**, 749 (1907).

[53] H. Köstlin, R. Jost, and W. Lems, *Optical and electrical properties of doped in2o3 films,* physica status solidi (a) **29**, 87 (1975).

[54] R. Bel Hadj Tahar, T. Ban, Y. Ohya, and Y. Takahashi, *Tin doped indium oxide thin films: Electrical properties,* Journal of Applied Physics **83**, 2631 (1998).

[55] R. Weiher and R. Ley, *Optical properties of indium oxide,* Journal of Applied Physics **37**, 299 (1966).

[56] J. C. Fan M and J. B. Goodenough, *X-ray photoemission spectroscopy studies of sn-doped indium-oxide films,* Journal of Applied Physics **48**, 3524 (1977).

[57] N. Balasubramanian and A. Subrahmanyam, *Electrical and optical properties of reactively evaporated indium tin oxide (ito) films-dependence on substrate temperature and tin concentration,* Journal of Physics D: Applied Physics **22**, 206 (1989).

[58] T. Koida, H. Fujiwara, and M. Kondo, *High-mobility hydrogen-doped in2o3 transparent conductive oxide for a-si: H/c-si heterojunction solar cells,* Solar Energy Materials and Solar Cells **93**, 851 (2009).

[59] L. Barraud, Z. Holman, N. Badel, P. Reiss, A. Descoeudres, C. Battaglia, S. De Wolf, and C. Ballif, *Hydrogen-doped indium oxide/indium tin oxide bilayers for high-efficiency silicon heterojunction solar cells,* Solar Energy Materials and Solar Cells **115**, 151 (2013).

[60] J. J. Meléndez and M. Wierzbowska, *In2o3 doped with hydrogen: electronic structure and optical properties from the pseudopotential self-interaction corrected density functional theory and the random phase approximation,* The Journal of Physical Chemistry C **120**, 4007 (2016).

[61] H. Hartnagel, A. Dawar, A. Jain, and C. Jagadish, *Semiconducting transparent thin films,* Bristol and Ph (1995).

[62] C. G. Granqvist, *Transparent conductors as solar energy materials: A panoramic review,* Solar energy materials and solar cells **91**, 1529 (2007).

[63] K. Ellmer, *Transparent conductive zinc oxide and its derivatives,* in *Handbook of Transparent Conductors* (Springer, 2011) pp. 193–263.

[64] W. L. Bragg, *Lxii. the crystalline structure of zinc oxide,* The London, Edinburgh, and Dublin Philosophical Magazine and Journal of Science **39**, 647 (1920).

[65] O. Kluth, G. Schöpe, J. Hüpkes, C. Agashe, J. Müller, and B. Rech, *Modified thornton model for magnetron sputtered zinc oxide: film structure and etching behaviour,* Thin solid films **442**, 80 (2003).

[66] D. Y. Kim, E. Guijt, R. A. Swaaij, and M. Zeman, *Development of a-siox: H solar cells with very high voc* ff product,* Progress in Photovoltaics: Research and Applications **23**, 671 (2015).

[67] A. Chowdhury, S. Mukhopadhyay, and S. Ray, *Effect of electrode separation on pecvd deposited nanocrystalline silicon thin film and solar cell properties,* Solar Energy Materials and Solar Cells **94**, 1522 (2010).

[68] K. Carl, H. Schmitt, and I. Friedrich, *Optimization of sputtered ito films with respect to the oxygen partial pressure and substrate temperature,* Thin Solid Films **295**, 151 (1997).

[69] C. S. Solanki, *Solar photovoltaics: fundamentals, technologies and applications* (PHI Learning Pvt. Ltd., 2015).

[70] M. Bennett and R. Arya, *Measurement techniques for evaluation of a-si: H solar cells,* Solar cells **18**, 289 (1986).

[71] L. van der PAUYV, *A method of measuring specific resistivity and hall effect of discs of arbitrary shape,* Philips Res. Rep **13**, 1 (1958).

[72] O. Breitenstein, J. Bauer, K. Bothe, D. Hinken, J. Müller, W. Kwapil, M. C. Schubert, and W. Warta, *Luminescence imaging versus lock-in thermography on solar cells and wafers,* in *26th European Photovoltaic Solar Energy Conference and Exhibition* (2011) pp. 1031–1038.

[73] K. Jäger, *On the Scalar Scattering Theory for Thin-Film Solar Cells*, Ph.D. thesis, TU Delft, Delft University of Technology (2012).

[74] H. Fujiwara, *Spectroscopic ellipsometry: principles and applications* (John Wiley & Sons, 2007).

[75] H. G. Tompkins, *https://www.aps.org/units/fiap/meetings/presentations/upload/tompkins.pdf,* .

[76] H. Tan, R. Santbergen, A. H. Smets, and M. Zeman, *Plasmonic light trapping in thin-film silicon solar cells with improved self-assembled silver nanoparticles,* Nano letters **12**, 4070 (2012).

[77] B. Vet and M. Zeman, *Relation between the open-circuit voltage and the band gap of absorber and buffer layers in a-si: H solar cells,* Thin Solid Films **516**, 6873 (2008).

[78] T. P. White, N. N. Lal, and K. R. Catchpole, *Tandem solar cells based on high-efficiency c-si bottom cells: top cell requirements for> 30% efficiency,* IEEE Journal of Photovoltaics **4**, 208 (2014).

[79] J. Y. Zhengshan, K. C. Fisher, B. M. Wheelwright, R. P. Angel, and Z. C. Holman, *Pvmirror: a new concept for tandem solar cells and hybrid solar converters,* IEEE Journal of Photovoltaics **5**, 1791 (2015).

[80] D. Y. Kim, E. Guijt, F. T. Si, R. Santbergen, J. Holovskỳ, O. Isabella, R. A. van Swaaij, and M. Zeman, *Fabrication of double-and triple-junction solar cells with hydrogenated amorphous silicon oxide (a-siox: H) top cell,* Solar Energy Materials and Solar Cells **141**, 148 (2015).

[81] S. Inthisang, T. Krajangsang, I. A. Yunaz, A. Yamada, M. Konagai, and C. R. Wronski, *Fabrication of high open-circuit voltage a-si1–xox: H solar cells by using p-a-si1–xox: H as window layer,* physica status solidi (c) **8**, 2990 (2011).

[82] M. I. Kabir, S. A. Shahahmadi, V. Lim, S. Zaidi, K. Sopian, and N. Amin, *Amorphous silicon single-junction thin-film solar cell exceeding 10% efficiency by design optimization,* International Journal of Photoenergy **2012** (2012).

[83] G. Mei-Zhen, R. Job, X. De-Sheng, and W. Fahrner, *Thickness dependence of resistivity and optical reflectance of ito films,* Chinese Physics Letters **25**, 1380 (2008).

[84] C. Guillen and J. Herrero, *Optical, electrical and structural characteristics of al: Zno thin films with various thicknesses deposited by dc sputtering at room temperature and annealed in air or vacuum,* Vacuum **84**, 924 (2010).

[85] B.-Z. Dong, G.-J. Fang, J.-F. Wang, W.-J. Guan, and X.-Z. Zhao, *Effect of thickness on structural, electrical, and optical properties of zno: Al films deposited by pulsed laser deposition,* Journal of Applied Physics **101**, 033713 (2007).

[86] T. Minami, H. Nanto, and S. Takata, *Highly conductive and transparent aluminum doped zinc oxide thin films prepared by rf magnetron sputtering,* Japanese Journal of Applied Physics **23**, L280 (1984).

[87] T. Minami, H. Nanto, and S. Takata, *Optical properties of aluminum doped zinc oxide thin films prepared by rf magnetron sputtering,* Japanese journal of applied physics **24**, L605 (1985).

[88] M. Kumar, J.-H. Yun, and J. Kim, *Metal/semiconductor and transparent conductor/semiconductor heterojunctions in high efficient photoelectric devices: progress and features,* International Journal of Photoenergy **2014** (2014).

[89] J.-H. Yun and J. Kim, *Double transparent conducting oxide films for photoelectric devices,* Materials Letters **70**, 4 (2012).

[90] J.-H. Yun, J. Kim, Y. C. Park, S.-J. Moon, and W. A. Anderson, *Double transparent conducting layers for si photovoltaics,* Thin Solid Films **547**, 17 (2013).

[91] R. G. Gordon, *Deposition of transparent conducting oxides for solar cells,* AIP Conference Proceedings **394**, 39 (1997).

[92] K. Ravichandran, N. J. Begum, K. Swaminathan, and B. Sakthivel, *Fabrication of a double layered fto/azo film structure having enhanced thermal, electrical and optical properties, as a substitute for ito films,* Superlattices and Microstructures **64**, 185 (2013).

[93] J. M. Cho, J. Kim, H. Kim, M. Kim, S.-J. Moon, J. Jo, and W. S. Shin, *Ito/azo double-layered transparent conducting oxide films for organic photovoltaic cells,* Molecular Crystals and Liquid Crystals **597**, 1 (2014).

[94] Y.-K. Moon, S.-H. Kim, and J.-W. Park, *The influence of substrate temperature on the properties of aluminum-doped zinc oxide thin films deposited by dc magnetron sputtering,* Journal of Materials Science: Materials in Electronics **17**, 973 (2006).

[95] T. Moss, *The interpretation of the properties of indium antimonide,* Proceedings of the Physical Society. Section B **67**, 775 (1954).

[96] S. Dongaonkar, J. D. Servaites, G. M. Ford, S. Loser, J. Moore, R. M. Gelfand, H. Mohseni, H. W. Hillhouse, R. Agrawal, M. A. Ratner, *et al.*, *Universality of non-ohmic shunt leakage in thin-film solar cells,* Journal of Applied Physics **108**, 124509 (2010).

[97] K. Chemie, *https://www.distrelec.nl,* (2007).

[98] G. Benno and K. Joachim, *Optical properties of thin semiconductor films,* October, 31st (2003).

[99] R. Santbergen, *http://www.ewi.tudelft.nl/fileadmin/faculteit/ewi/documentenafdelingen/electrical*$_{s}$*ustainable*$_{e}$*nergy/pvmd/genpro4*$_{m}$*anual.pdf,* (2016).

[100] R. Santbergen, T. Meguro, T. Suezaki, G. Koizumi, K. Yamamoto, and M. Zeman, *Genpro4 optical model for solar cell simulation and its application to multijunction solar cells,* IEEE Journal of Photovoltaics **7**, 919 (2017).

[101] J. Santos, S. Fernández, and J. Cárabe, *Effect of azo–coating thickness on a-si:h p-i-n solar-cell performance,* 26th European Photovoltaic Solar Energy Conference and Exhibition **26**, 2727 (2011).

[102] F. Meillaud, A. Shah, C. Droz, E. Vallat-Sauvain, and C. Miazza, *Efficiency limits for single-junction and tandem solar cells,* Solar energy materials and solar cells **90**, 2952 (2006).

[103] R. Santbergen, R. Mishima, T. Meguro, M. Hino, H. Uzu, J. Blanker, K. Yamamoto, and M. Zeman, *Minimizing optical losses in monolithic perovskite/c-si tandem solar cells with a flat top cell,* Optics express **24**, A1288 (2016).

[104] P. Buskens, M. Burghoorn, M. C. D. Mourad, and Z. Vroon, *Antireflective coatings for glass and transparent polymers,* Langmuir **32**, 6781 (2016).

[105] B. W. Schneider, N. N. Lal, S. Baker-Finch, and T. P. White, *Pyramidal surface textures for light trapping and antireflection in perovskite-on-silicon tandem solar cells,* Optics express **22**, A1422 (2014).

[106] O. Gençyılmaz, F. Atay, and I. Akyüz, *Deposition and ellipsometric characterization of transparent conductive al-doped zno for solar cell application,* Journal of Clean Energy Technologies **4**, 90 (2016).

[107] M. J. Dodge, *Refractive properties of magnesium fluoride,* Applied Optics **23**, 1980 (1984).

[108] H. K. Raut, V. A. Ganesh, A. S. Nair, and S. Ramakrishna, *Anti-reflective coatings: A critical, in-depth review,* Energy & Environmental Science **4**, 3779 (2011).

[109] I. Malitson and M. Dodge, *Refractive-index and birefringence of synthetic sapphire,* in *Journal Of The Optical Society Of America*, Vol. 62 (AMER INST PHYSICS CIRCULATION FULFILLMENT DIV, 500 SUNNYSIDE BLVD, WOODBURY, NY 11797-2999, 1972) pp. 1405–1405.

[110] Merck, *http://www.merck-performance-materials.com,* (2016).

[111] H. Kanda, A. Uzum, N. Harano, S. Yoshinaga, Y. Ishikawa, Y. Uraoka, H. Fukui, T. Harada, and S. Ito, *Al2o3/tio2 double layer anti-reflection coating film for crystalline silicon solar cells formed by spray pyrolysis,* Energy Science & Engineering **4**, 269 (2016).

[112] S.-Y. Lien, D.-S. Wuu, W.-C. Yeh, and J.-C. Liu, *Tri-layer antireflection coatings (sio 2/sio 2–tio 2/tio 2) for silicon solar cells using a sol–gel technique,* Solar Energy Materials and Solar Cells **90**, 2710 (2006).

A

Appendix

A.1. General

A.1.1. Shockley equation

$$J(V_a) = J_0 \cdot (exp(\frac{e \cdot V_a}{nkT}) - 1) \tag{A.1}$$

Here n is the ideality factor. in case of ideal conditions it is equal to one. J_0 is the reverse saturation current density, e is the elementary charge, k is Boltzmann constant, T is temeprature and V_a is the applied voltage.

A.1.2. Optical parameters for Croning Eagle XG glass substrate

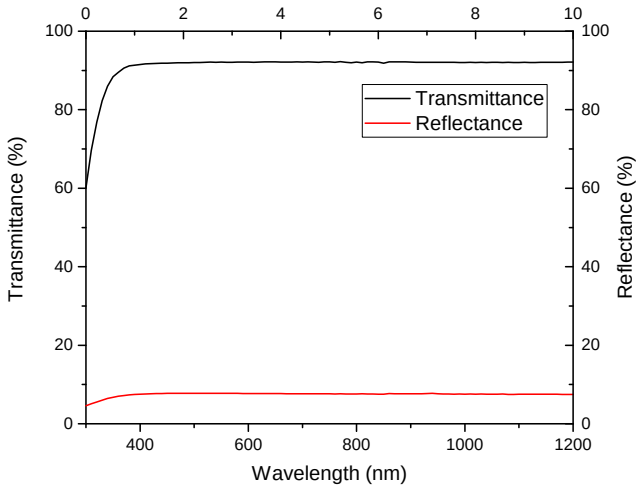

Figure A.1: The plot of the transmittance and reflection (in percentage) versus the wavelength for the Croning XG glass .

From the values of transmittance and reflectance, the absorptance of the Croning Eagle XG glass can be computed. The average value in the spectral range of 300 to 1200 nm is 1.5%. This value will be used to correct for the absorptance for different materials deposited on the Croning Eagle XG glass substrate. The plot of transmittance and reflectance is shown in Figure. A.1.

A.1.3. Absorption Coefficient

From the experimentally determined transmittance (T) and reflectance (R), the value of absorption coefficient (α) can be determined by using the below mathematical equation.

$$\alpha = -\frac{1}{d} \cdot ln\frac{T}{(1-R)^2} \tag{A.2}$$

In the above formula d is the thickness of the layer. This formula is based on some approximations. The substrate on which the layer whose R and T are measured has perfect transmittance. The layer has appreciable absorption. In low energy spectrum (above 1200 nm) the formula is not valid.

A.1.4. Material Depositions

The parameters used for the deposition of the a-SiO_x:H cell were taken from the work of Erwin Guijt and Do Yun Kim [42]. The temperature of deposition for n and p layer was 300 deg Celsius for the i layer it was 200 was deg Celsius. The bandgap of a-SiO_x:H intrinsic layer was 1.96 pm 0.07 eV. The activation energy of the p layer was- 0.52 pm 0.04 eV and for n (nc-a-SiO_x:H) layer was 0.14 pm 0.02 eV. The bandgap of p layer was- 2.01 pm 0.03 eV and for n (nc-a-SiO_x:H) layer it was 2.62 pm 0.06 eV. The deposition parameters for the AZO, ITO and IO:H were taken from the past work done in PVMD group. The heater temperature of deposition for AZO was 300 deg Celsius.

B

Appendix

B.1. Chapter-3

B.1.1. Derivation for Spectral Response 4T (SR_{4T})

The derivation of this parameter can be obtained from the definition of conversion efficiency of a solar cell. Conversion efficiency or efficiency(η) can be mathematically written as,

$$\eta = \frac{OutputPower}{InputPower} \tag{B.1}$$

In case of solar cells, the Output power is defined as the product of open circuit voltage (V_{oc}) , fill Factor (FF) and short circuit current density (J_{sc}). The input is taken as the integral of the AM 1.5 (global) spectrum as shown in figure. 3.3. According to the definition of J_{sc} (taken to be positive value), it can be written as shown below,

$$J_{sc} = \int_{280}^{4000} EQE(\lambda) \cdot \phi(\lambda) \cdot q \cdot d(\lambda) \tag{B.2}$$

The limits of integration are taken according to the AM1.5 spectrum and these wavelength values are in nanometer. Here the photon flux ($\phi(\lambda)$) at the specific wavelength and elementary charge (q) are taken. To calculate the photon flux (ϕ), AM1.5 (Global spectrum) was used. Mathematically, the spectral irradiance ($I(\lambda)$) as a function of wavelength at AM 1.5 can be related to the photon flux at that wavelength as shown below,

$$\phi(\lambda) = \frac{I(\lambda) \cdot \lambda}{hc} \tag{B.3}$$

In the above equation h is the Planck's constant and c is the speed of light in vacuum. Thus equation. B.2 can be written as shown below,

$$J_{sc} = \int_{280}^{4000} \frac{EQE(\lambda) \cdot I(\lambda) \cdot \lambda \cdot e}{hc} \cdot d(\lambda) \tag{B.4}$$

Using equation B.4 to write the output response of the PV cell, and taking the terms V_{oc} and FF inside the integral. They are taken as constants. The output becomes,

$$Output = \int_{280}^{4000} \frac{EQE(\lambda) \cdot I(\lambda) \cdot \lambda \cdot e \cdot V_{oc} \cdot FF}{hc} \cdot d(\lambda) \tag{B.5}$$

Finally, the spectral response 4T (SR_{4T}) can be defined mathematically as follows,

$$SR_{4T} = \frac{EQE(\lambda) \cdot I(\lambda) \cdot \lambda \cdot e \cdot V_{oc} \cdot FF}{hc} \tag{B.6}$$

This term can be decomposed to get the unitless R_{4T} term, which is independent of the spectrum. The quantity SR_{4T} has a unit of $Wm^{-2}nm^{-1}$, which is same as that of Spectral irradiance. To take into

account all the units involved in the calculations a factor of 10^{-9} is multiplied to the results obtained from the equation 3.3.

So the efficiency of the cell as defined in equation B.1 becomes,

$$\eta = \frac{\int_{280}^{4000} SR_{4T} \cdot d(\lambda)}{\int_{280}^{4000} I(\lambda) \cdot d(\lambda)} \tag{B.7}$$

Hence from the computation of SR_{4T}, we can determine the efficiency of the PV cell. It is also important to mention that there is a slight difference in the efficiency calculations from SR_{4T} and the experimental value of efficiency, which is due to errors present in the J-V measurements as well as the errors present in the integration involved. This error is between 0.5 to 1% as compared to experimental values.

B.2. Chapter-4

The Genpro4 results pertaining to the reference cell and the optimised cell-B are shown in figure B.1. It can be seen that with the new cell structure an gain of 0.52 mA/cm^2 can be obtained, although this may seem very low, but if we go in more detail and compare the EQE of the two cells, we can see that this gain lies in the blue green part of the spectrum. This increase in the specific part of spectrum is most important in our application.

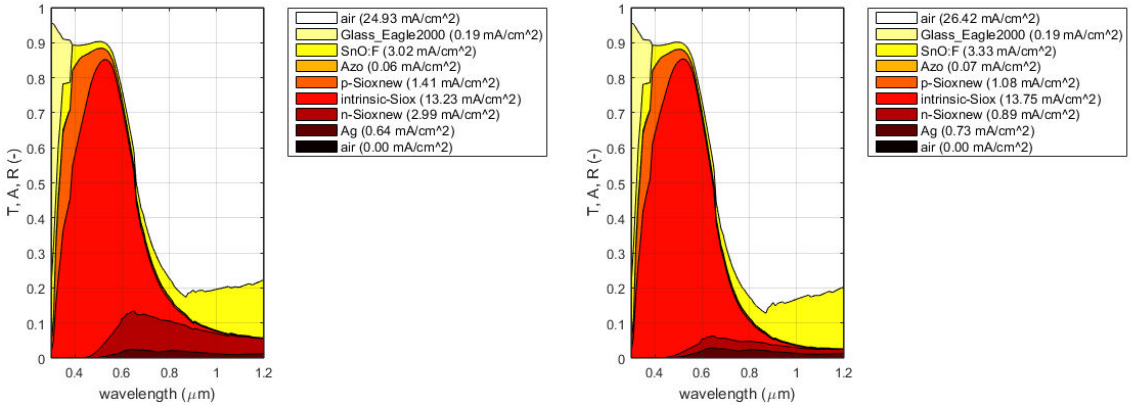

(a) (b)

Figure B.1: GenPro4 results of the (a) Reference a-SiO$_x$:H cell (b) New optimised a-SiO$_x$:H cell(Cell-B)

B.2.1. Bias EQE

To verify whether there is some scope of further development regarding the thickness of layers of the thin film cell a biased EQE test is performed. In this test the optimised cell is given an reverse bias, and then the EQE is measured. As the optical system remains same, no additional optical losses occur. In thin film cells the quantum efficiency is bias dependent as the collection of charges is field assisted. Hence by applying a reverse bias the charge collection should increase. In case the cell is optimised such that all the charge carriers are already collected, no influence of reverse bias should be observed [70]. Otherwise if this is not the case then it means that the collection of charge carriers is poor. The EQE plots at reverse bias voltage ranging from 0 to 4 volts in steps of 0.5 volts is shown in figure B.2. The voltage was limited at 4V as after that some transients effects were observed. Even at 3.5V some transients can be seen. The reason of this could be some field build up in the absorber layer, or could be due to loading effect in the measuring instrument.

From these measurements no significant gain in the J_{sc} was obtained, this means that the a-SiO$_x$:H cell device structure is not having large parasitic absorption.

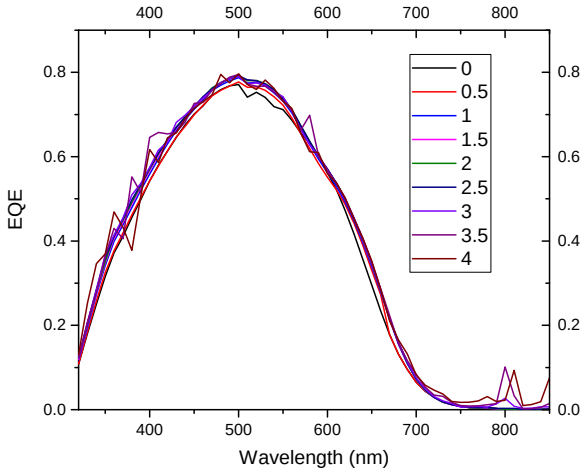

Figure B.2: The EQE at reverse bias voltage (in volts) of the optimised Cell

B.3. Chapter-5

Error margins (Standard Deviation) for the sheet resistance and resistivity of the TCO layers are negligible. Hence, the error margins are not shown. For example the error in resistivity of the 50 nm ITO layer is 2.21 X 10^{-3}. Standard deviation for mobility and carrier concentration.

Table B.1: Standard deviation in mobility and carrier concentration of the as-deposited TCO layers.

Material	Thickness (nm)	μ (cm^2/V.s)	N_c ($10^{19} cm^{-3}$)
ITO	50	0.27	1.10
	100	0.23	1.49
	200	0.21	1.68
IO:H	50	2.06	0.08
	100	1.82	0.73
AZO	50	0.02	
	100	0.03	0.04
	200	0.05	

The EQE of the two cells with 100 nm of AZO and 100 nm of ITO back contact are shown in figure B.3. There is an interesting observation about the response in the near UV and blue region of the spectrum, the 100 nm AZO cell has higher response. The reason of this is not too clear. The J-V curve of one of the best cells with 100 nm of AZO and 100 nm of ITO back contact are shown in figure B.4. The value of series resistance per unit area of the 100 nm AZO cell is 0.000719 ω/m^2 and for 100 nm ITO is 0.000644 ω/m^2. The value of shunt resistance per unit area are 0.131 ω/m^2 for 100 nm AZO and 0.133 ω/m^2 for 100 nm ITO. The shunt resistance values are almost similar for the two cells. These values are for only one cell, but in the chapter-5 the average values are shown.

B.4. Chapter-6

The SR_{4T} plot utilising the experimental values of the cells used for actual fabrication of the four terminal device are shown below. Maximum efficiency rise of 2.72% can be obtained when the poly-Si cell is utilised as the bottom cell. The plots for the three different bottom cells are shown in figure B.5. There is a gain of 0.60% for the IBC bottom cell and a gain of 1.22% for the SHJ (Hybrid) bottom cell.

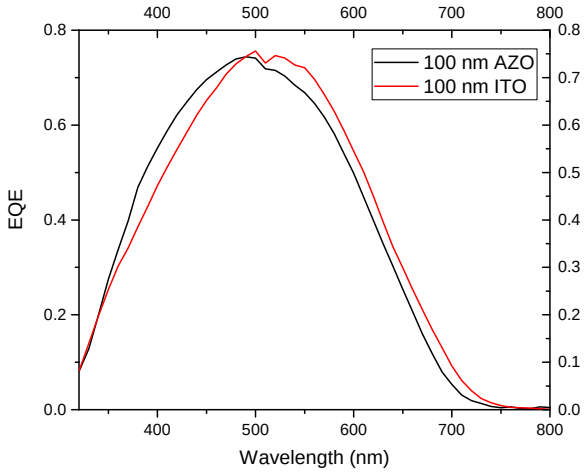

Figure B.3: The EQE of the two cells with 100 nm of AZO and 100 nm of ITO back contact.

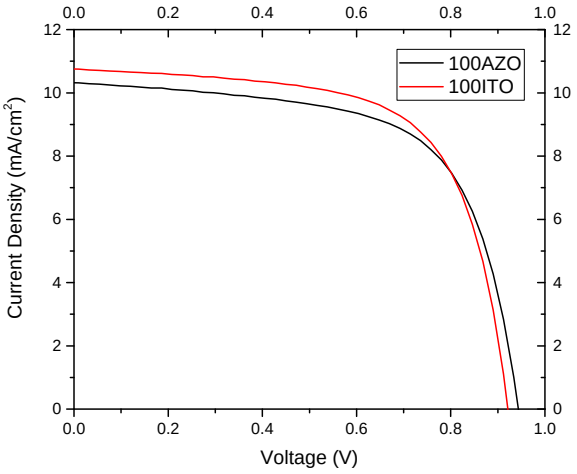

Figure B.4: The JV of the two cells with 100 nm of AZO and 100 nm of ITO back contact.

B.5. Chapter-7

B.5.1. Simulation

The simulation results are compared with the measured EQE plots in the plots shown in figure B.6. The measured values can be found in table 3.2, only the best cells are compared. The simulated results are mentioned in figure B.8. The J_{sc} values are the current in the c-Si layer. The a-SiO_x:H parameters are mentioned in chapter-5. Exact match between the simulated and measured values is not possible due to various electrical losses due to recombination, series and shunt resistance. Errors could also be due to the measurement apparatus of EQE and J-V. The error is between 3-6% for the values.

The schematic structure for the four terminal cell with IBC bottom cell is shown in figure. B.7.

Here are all the simulation results with the actual GenPro4 plots are shown. The numbers in the box signify the actual absorption in the material. As air is also simulated as a material, hence reflection losses are estimated to be the absorption in the air medium. Similarly, the short circuit current generated by the cell is equal to the absorption in the absorber or active layer. The names of the layers for the simulations are- p-Sioxnew is the p-a-SiO_x:H, intrinsic-Siox is the i-a-SiO_x:H, n-Sioxnew is the n-nc-SiO_x:H for the top cell. For the bottom cells, the name of the layers are- SiN-IBC is SiN ARC, c-Si-doped is the poly-Si, Sio2 is the silicon oxide and c-Si is the crystalline silicon wafer.

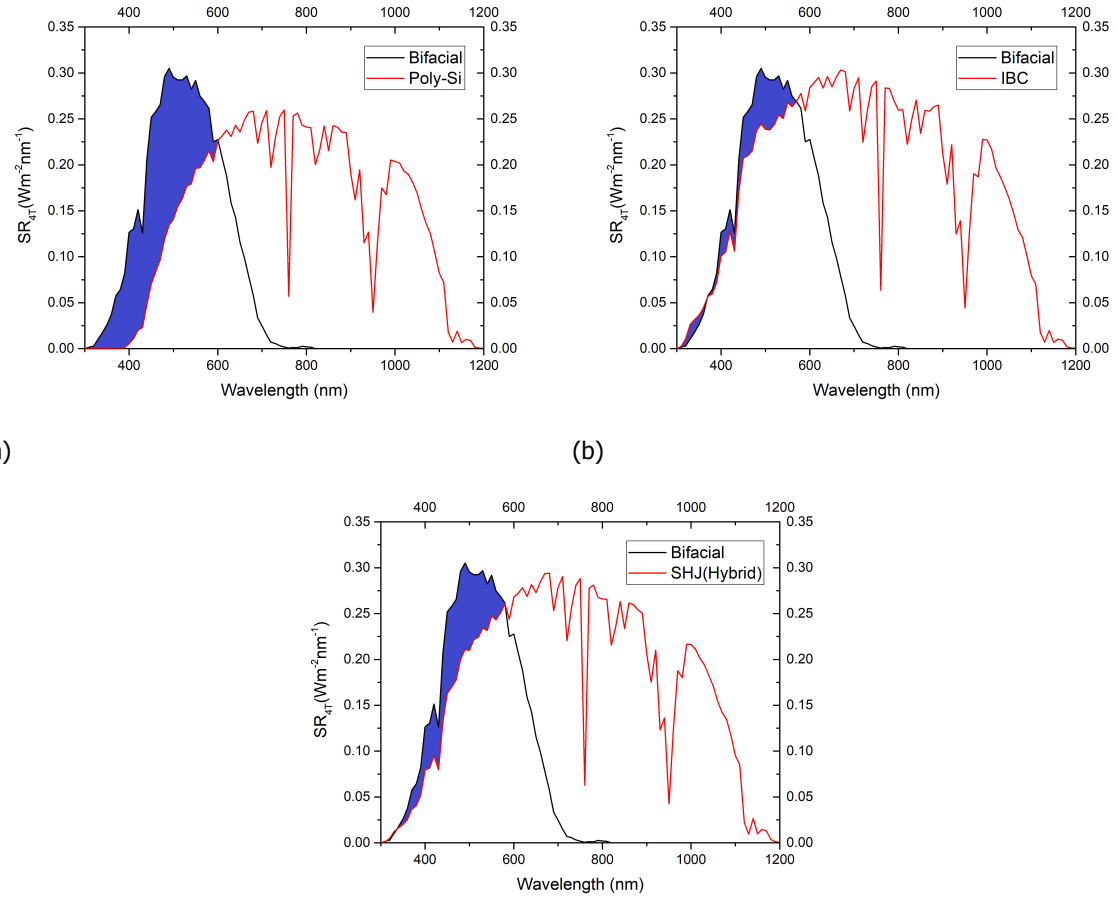

Figure B.5: SR_{4T} plot for the four terminal device with bifacial a-SiO_x:H top cell and a) poly-Si b)IBC c)SHJ (Hybrid) bottom cell.

The Asahi glass is simulated by using a glass of 1000 um thickness and a layer of FTO. The results are presented in the figure B.8.

The results for the simulation results when the cell are in four terminal are shown in figure B.9.

B.5.2. Calculation of the components of the reflection losses

The simulations corresponding to the reflection losses in case of a poly-Si four terminal device are presented. To calculate these values the thickness of the layers are changed. To get R_1 the glass of the top cell is made infinite. Similarly, to get the sum of R_1+R_2, the thin film cell p layer is made infinitely thick. Likely for the sum of R_1+R_2+R_3+R_4 the c-Si cell is made infinitely thick. In this way, the reflectance components are computed. The simulation results can be seen in figure B.10.

The simulation results for IBC and SHJ (Hybrid) cell are shown in the figure B.11. As the optical system remains same for computation of the first three reflection terms, thus only results for the case with infinite crystalline silicon cell and metal back contact.

The magnitude of the various reflection losses for the four terminal cell with poly-Si bottom cell is shown in table B.2.

The reflection losses are shown in figure B.12. It is clear that at the top glass and air interface almost 4% light (in comparison to total absorption) is lost to reflection which is in accordance with literature and Fresnel's equations [100]. It can be seen that the reflection component from the second interface i.e. the textured glass and thin film cell contributes the maximum to reflection. This was not expected as Asahi glass is specifically designed to improve the optical path length. A possible reason could be that the texturing used still needs more optimisation.

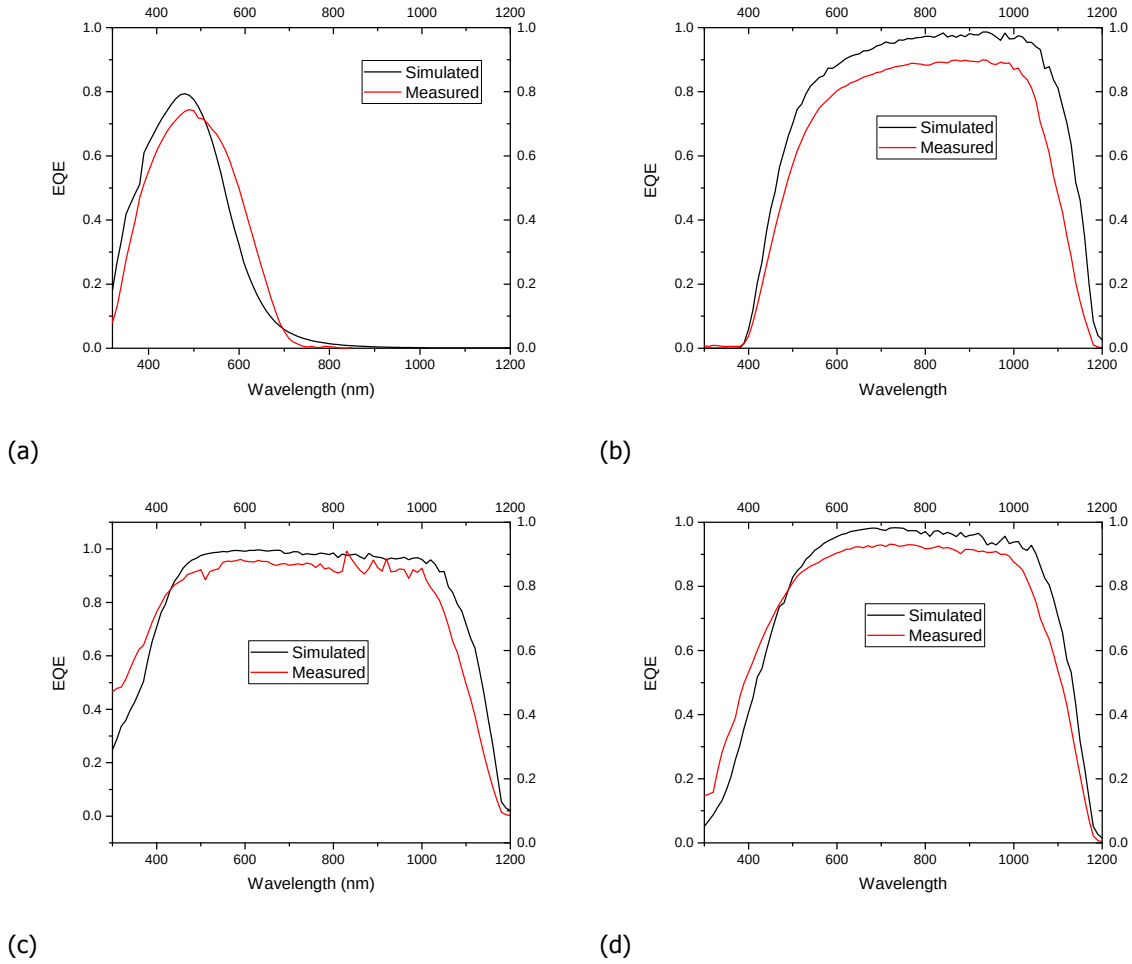

Figure B.6: GenPro4 results comparision with measured values for a) a-SiO_x:H b) poly-Si c) IBC d) SHJ (Hybrid) cell, when simulated without the top cell.

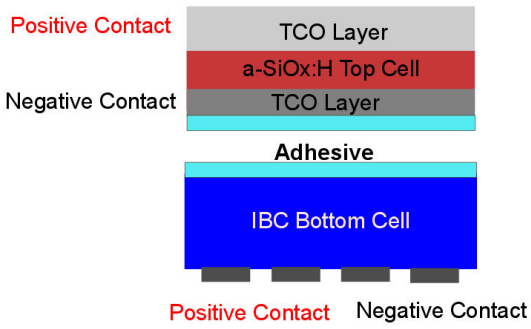

Figure B.7: The schematic structure for four terminal cell with IBC bottom cell. All the layers are not shown in this schematic.

B.5.3. Optimum refractive index and thickness calculations

According to Fresnel equations, the optimum refractive index ($n_{optimum}$ for a single Anti reflective coating can be calculated by utilising the formula given below,

$$n_{optimum} = \sqrt{n_{glass} \cdot n_{air}} \tag{B.8}$$

Putting the values for glass as 1.5 the formula yields an optimum refractive index of 1.22. The

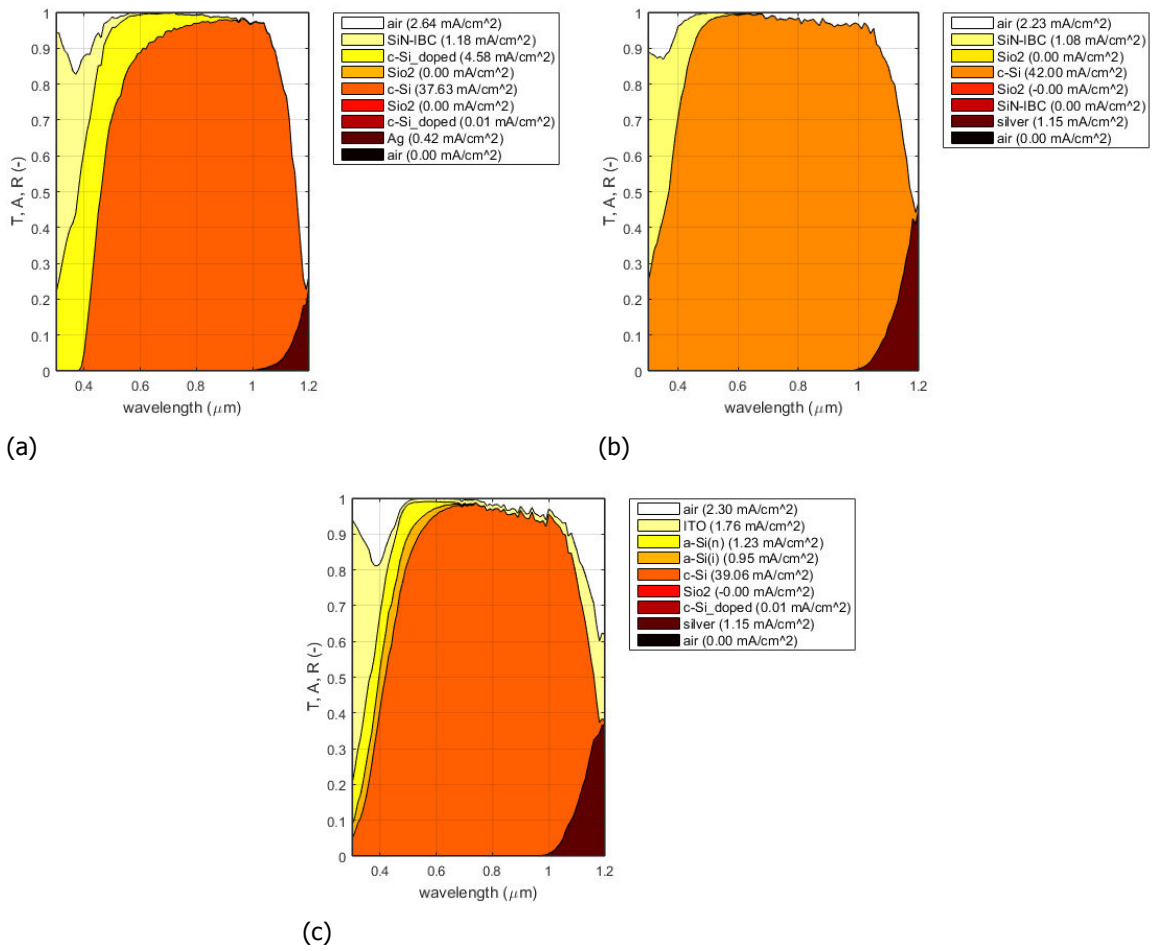

Figure B.8: GenPro4 results for a) poly-Si b) IBC c) SHJ (Hybrid) cell, when simulated without the top cell.

Table B.2: Numerical value of reflectance from the five major interfaces in terms of current density (mA/cm^2).

Reflectance Term	Numerical value
R_1	1.82
R_1+R_2	4.11
$R_1+R_2+R_3$	5.27
$R_1+R_2+R_3+R_4$	5.32
$R_1+R_2+R_3+R_4+R_5$	6.22

material that is nearest to this is magnesium fluoride (MgF_2) with a refractive index of approximately 1.38 [107]. For the calculation of optimum thickness quarter wave coating was used, this yielded a result of 90.57 nm for MgF_2 at 500 nm wavelength. The formula used is shown below,

$$Thickness = \frac{\lambda}{n_{optimum} \cdot 4} \tag{B.9}$$

Double layer ARC can also be utilised to further reduce reflectance from the top cell. The utilisation of double layer not only adds to the production steps but also requires calculations and simulations to determine the optimum refractive index and thickness. A simple approach is explained below to calculate the refractive index for double layer coating. The mathematical relation which is applied pertains to one single minimum [108]. In these quarter wave coating was used for both the layers. The mathematical relation is shown below,

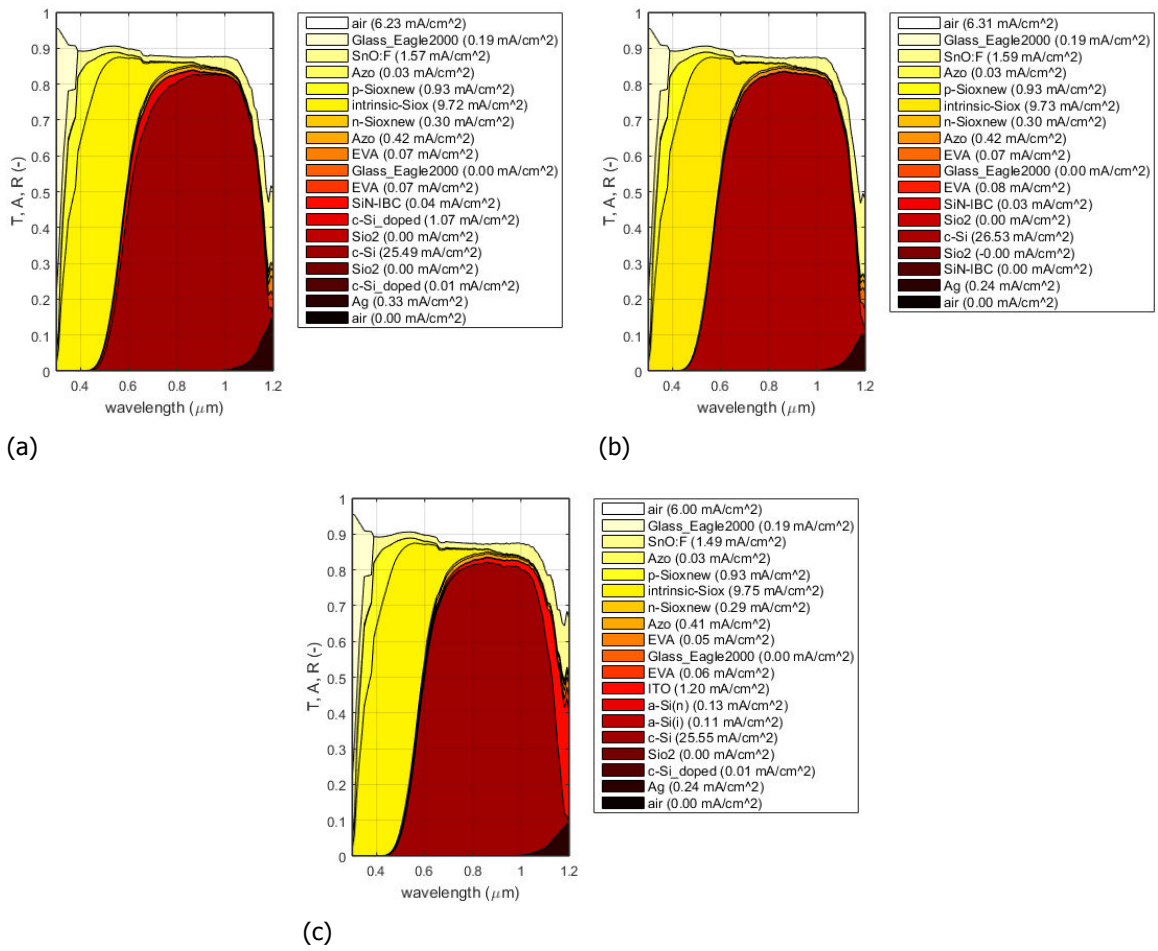

Figure B.9: GenPro4 results with the top cell for a) poly-Si b) IBC c) SHJ (Hybrid) cell.

$$\frac{n_1}{n_2} = \sqrt{\frac{n_{air}}{n_{glass}}} \tag{B.10}$$

where, n_1 implies the refractive index of the first coating and n_2 is the second coating refractive index. The first coating faces the air medium. With the first layer of MgF_2, this gives a value of 1.69 for the other layer. Thus the materials that can be chosen for the double layers are- Aluminium Oxide (Al_2O_3) with a refractive index of 1.77 and Cerium Fluoride (CeF_3) with a refractive index of 1.64 [109, 110]. The quarter wave thickness at 500nm for Al_2O_3 is 70.62 nm and for CeF_3 is 76.22 nm. The refractive index of these materials are mentioned in table B.3. Only three materials were tried in the simulation although more materials can be applied [111, 112].

Material	Refractive Index
Magnesium Fluoride (MgF_2)	1.38
Aluminium Oxide (Al_2O_3)	1.77
Cerium Fluoride (CeF_3)	1.64

Table B.3: Refractive Index of some available ARC materials suitable for glass substrate.

Only the best results with front pyramidal texturing and single layer ARC (with quarter wave thickness) are shown in figure B.13. The simulation results used to calculate the reflectance terms for the four terminal cell with poly-Si bottom cell after the reduction in reflection loss by using front pyramidal texturing and single layer ARC are presented in figure B.14.

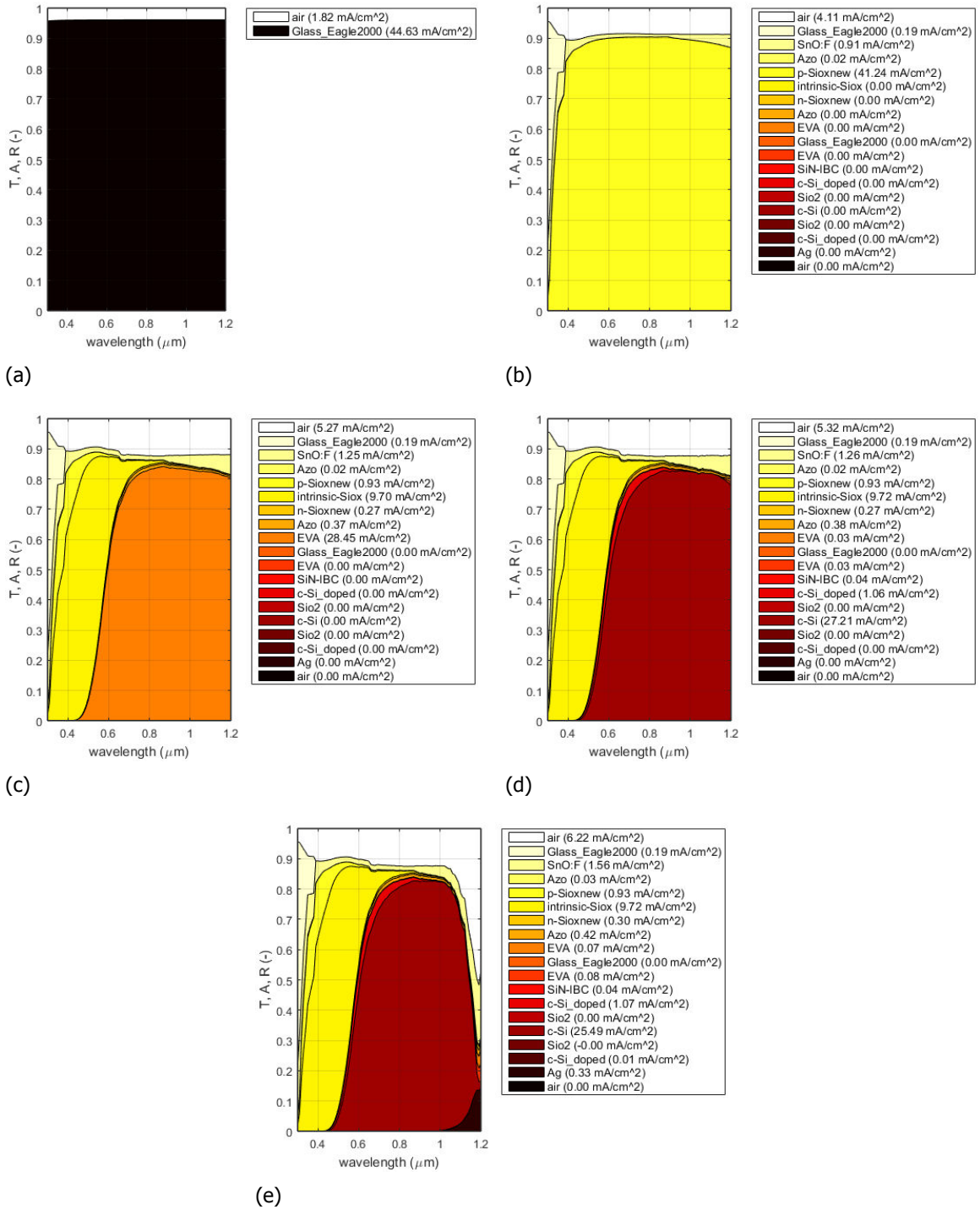

Figure B.10: GenPro4 results for Infinite Thick a) Top Glass b) Thin Film Cell c) First EVA layer d) Crystalline Silicon cell e) Metal Back Contact

B.5.4. AFM

The three textures with (σ_{rms}) of 430.1 nm, 326.5 nm and 737 nm, utilised in simulations to reduce R_2 component. The below AFM images were supplied by Dr.Guangtao Yang of PVMD group, TU Delft as shown in figure B.16. The image shown in b is zoomed in.

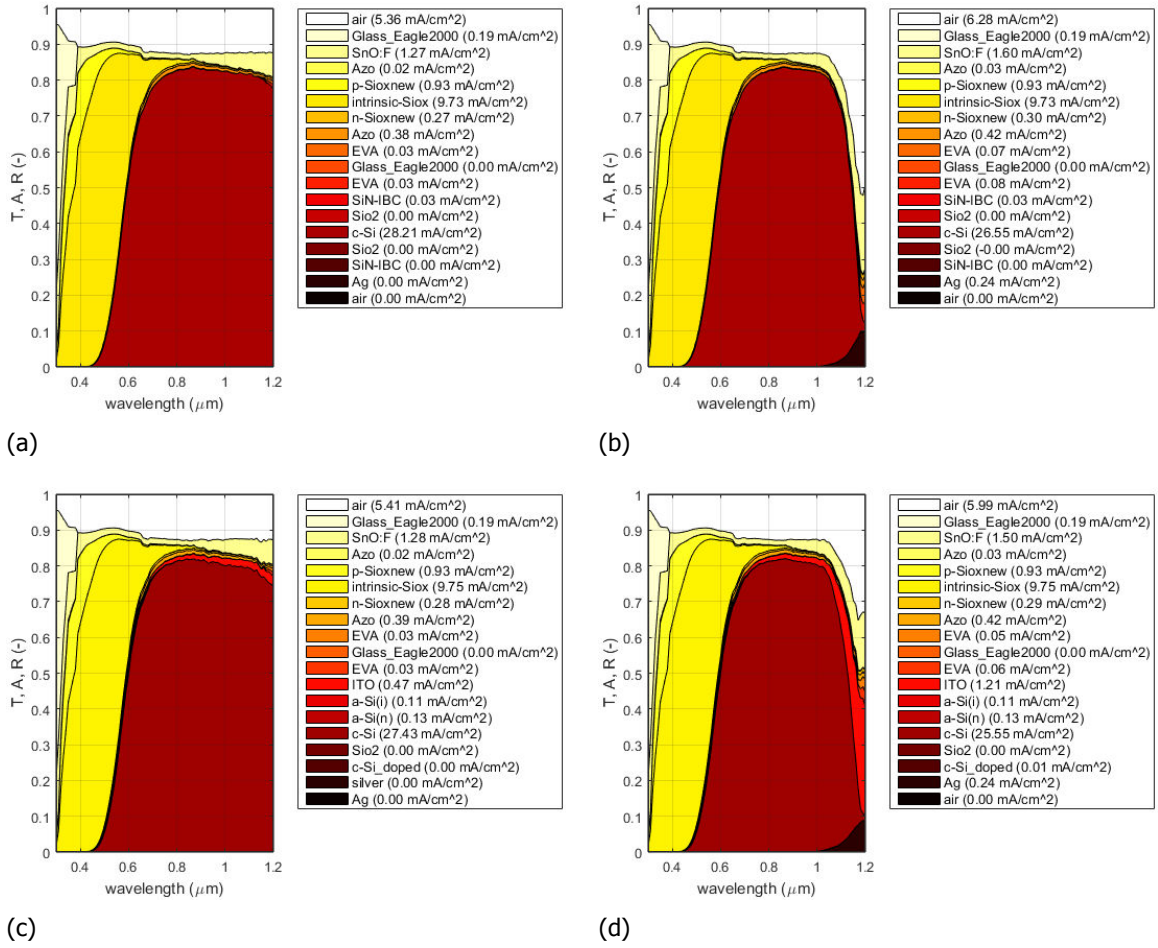

Figure B.11: GenPro4 results for infinite thick a) c-Si-IBC b) IBC metal back contact c) c-Si-SHJ (Hybrid) d) SHJ (Hybrid) metal back contact

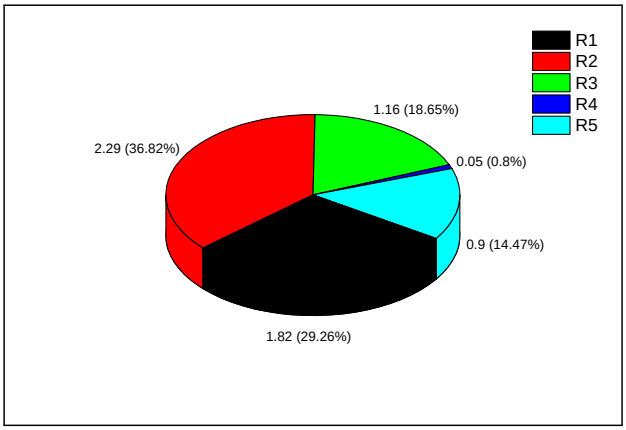

Figure B.12: The values of the reflectance terms.

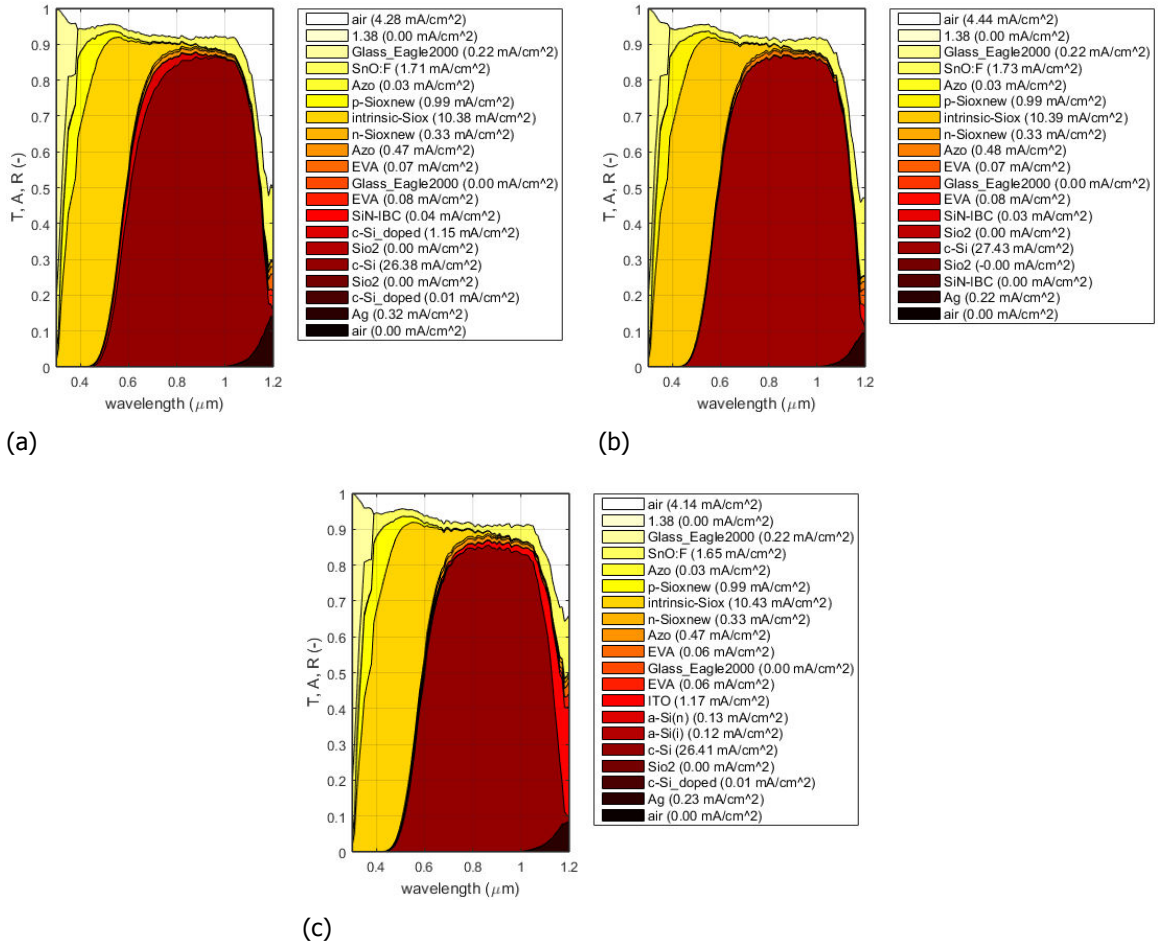

Figure B.13: GenPro4 results for a) poly-Si b) IBC c) SHJ (Hybrid) cell, when simulated with the top cell having pyramidal texturing and quarter wave thickness ARC.

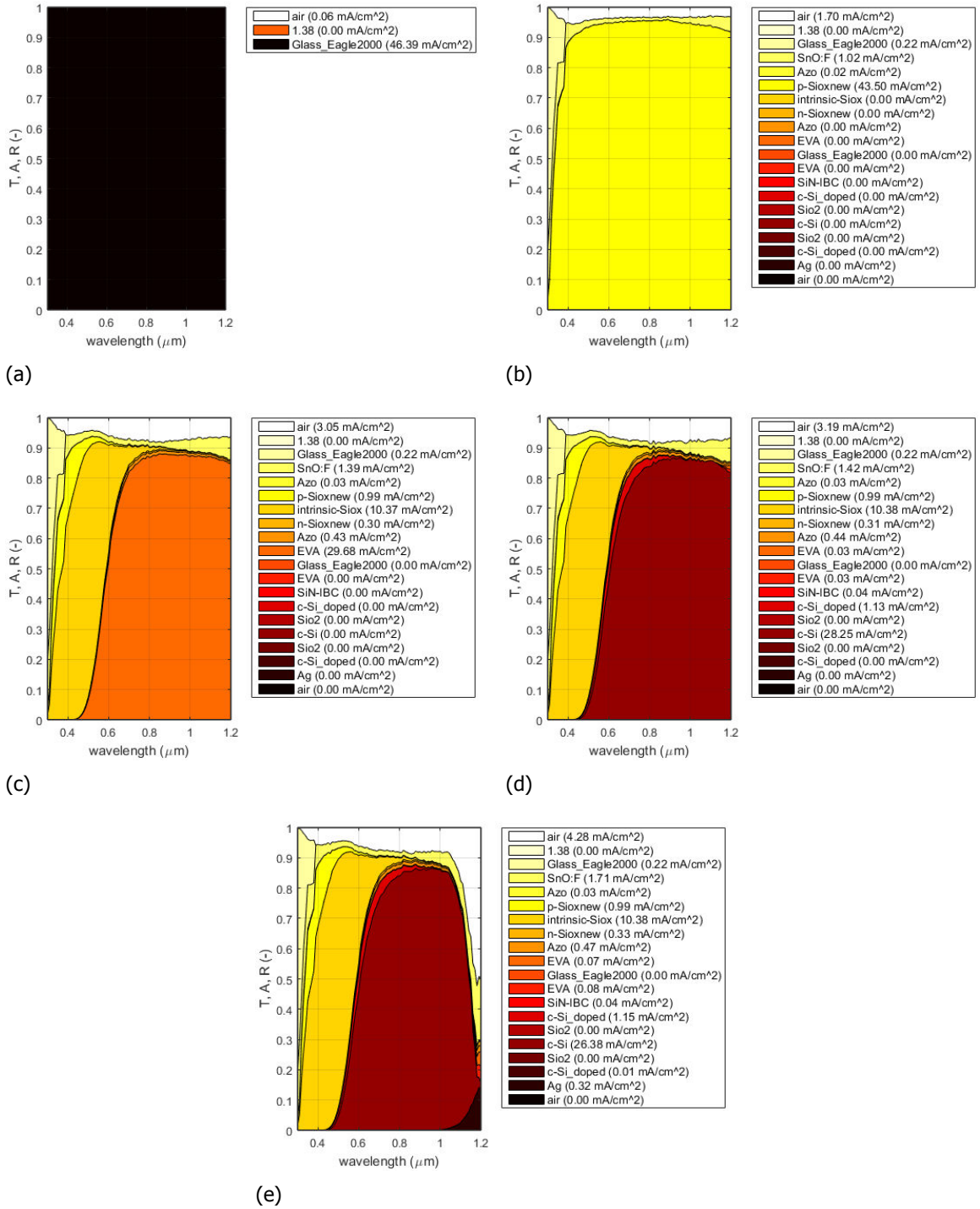

Figure B.14: GenPro4 results for Infinite Thick a) Top Glass b) Thin Film Cell c) First EVA layer d) Crystalline Silicon cell e) Metal Back Contact after reduction of reflection loss. These are for poly-Si based four terminal cell.

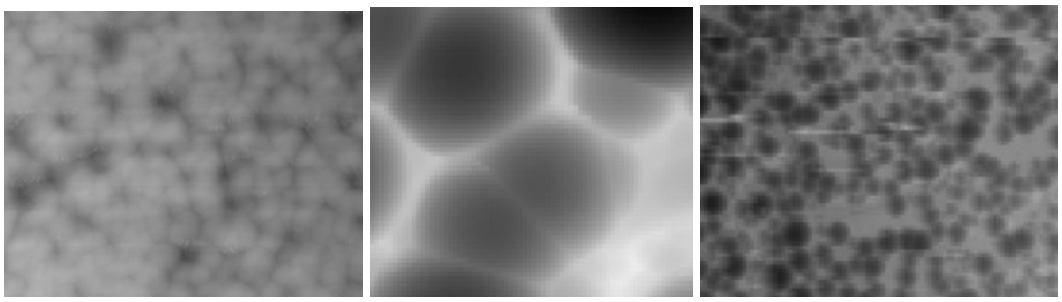

(a) (b) (c)

Figure B.15: The AFM images of the three textures used for simulations.

(a)	(b)	(c)
Selected area: 512 × 512 at (0, 0) px 20.04 × 20.04 at (0.00, 0.00) µm Mask in use: No	Selected area: 256 × 141 at (0, 0) px 20.08 × 11.06 at (0.00, 0.00) µm Mask in use: No	Selected area: 256 × 256 at (0, 0) px 100.4 × 100.4 at (0.0, 0.0) µm Mask in use: No
Minimum: 2.40580 µm Maximum: 4.79790 µm Average value: 3.51399 µm Median: 3.49420 µm Ra (Sa): 352.417 nm Rms (Sq): 430.056 nm Rms (grain-wise): 430.056 nm Skew: 0.1991 Kurtosis: -0.5371 Surface area: 449.766 µm^2 Projected area: 401.567 µm^2 Variation: 181.942 µm^2 Entropy: -13.264 Entropy deficit: 0.023434 Inclination θ: 4.29 deg Inclination φ: 61.85 deg	Minimum: 3.10340 µm Maximum: 4.86790 µm Average value: 4.08211 µm Median: 4.10690 µm Ra (Sa): 269.319 nm Rms (Sq): 326.454 nm Rms (grain-wise): 326.454 nm Skew: -0.3989 Kurtosis: -0.3649 Surface area: 262.979 µm^2 Projected area: 222.044 µm^2 Variation: 124.956 µm^2 Entropy: -13.562 Entropy deficit: 0.046416 Inclination θ: 2.40 deg Inclination φ: 122.56 deg	Minimum: 1.98520 µm Maximum: 6.55340 µm Average value: 4.05750 µm Median: 4.04270 µm Ra (Sa): 608.657 nm Rms (Sq): 737.002 nm Rms (grain-wise): 737.002 nm Skew: 0.06332 Kurtosis: -0.5884 Surface area: 11.5586 10^-9 m^2 Projected area: 10.0786 10^-9 m^2 Variation: 5.25517 10^-9 m^2 Entropy: -12.717 Entropy deficit: 0.015756 Inclination θ: 1.15 deg Inclination φ: 105.56 deg

Figure B.16: The parameters of the three textures. These were obtained from Gwyddion software.